

Orientation, rotation and solvation of ions in helium nanodroplets.

Thèse N° 9671

Présentée le 16 août 2019

à la Faculté des sciences de base

Laboratoire de nanodynamique moléculaire

Programme doctoral en chimie et génie chimique

pour l'obtention du grade de Docteur ès Sciences

par

Verónica OLIVER ÁLVAREZ DE LARA

Acceptée sur proposition du jury

Prof. V. Hatzimanikatis, président du jury

Dr. M. Drabbels, directeur de thèse

Prof. W. Kong, rapporteuse

Prof. A. Slenczka, rapporteur

Prof. T. Rizzo, rapporteur

2019

“Pretty spectra come from easy science.”

A. Clark, 2018.

A mi familia.

ABSTRACT

Helium nanodroplets are liquid, finite size, nanoscale helium clusters that have been employed since the 1990s as a matrix for high-resolution spectroscopy of molecules. Spectroscopic studies of ionic species inside helium droplets were not however realised until 2010, even though the potential information about their structure is of special interest since they are fundamental reaction intermediates in biochemistry. Additionally, the interaction of these species with the helium environment can be determined from these experiments, which is interesting from a fundamental point of view.

To determine structural information and study product selectivity, we proposed using high electric fields to orient the molecular ions in helium nanodroplets. Pendular state spectroscopy of neutral polar molecules in helium nanodroplets in the presence of electric fields has previously given satisfactory results to achieve molecular orientation, allowing one to distinguish biomolecular isomers. Our first experiments validated the technique for neutral aniline since the polarisation difference ratios, which express the degree of orientation, obtained from the NH_2 -stretch transitions were well-reproduced by calculations. On the other hand, the measured degree of orientation of cationic aniline is noticeably smaller than calculations show. Even so, the variation of the degree of orientation with electric field lets us conclude that orientation of the ions in helium droplets was observed. The results of several experiments performed to investigate the possible effects influencing the apparent orientation of the cations did not lead to any straightforward explanation. Our study therefore shows that orientation of molecular ions indeed seems possible and leads the way to possible future experiments.

To examine the formation of ionic-alkali solvation complexes in helium droplets upon photoionisation of the alkali, sodium, and understand the helium-dopant interaction we have performed ion spectroscopy. We found that several scenarios are possible after ionisation including dissociation, solvation and complete solvent evaporation depending on the ionisation process, droplet size and number of water ligands considered. Direct ionisation of sodium leads to solvation in the droplet, collision with the water molecules and formation of the ionic complexes if the

droplet size is sufficiently large. For these conditions, rovibrational spectroscopy of $\text{Na}(\text{OH}_2)^+$ was performed to obtain the A rotational constant in helium droplets and thus determine if the dopant-helium interaction affects the moment of inertia. From the results, we could confirm the latter but could not deduce the extent to which this was the case. This study shows how the spectral information of the solvated ions is useful to understand complexation dynamics in helium droplets and acquire further understanding about the dopant-helium interaction.

Keywords:

helium droplets, superfluid, cluster, ion, spectroscopy, pendular states, Stark effect, sodium, aniline, solvated complex.

RÉSUMÉ

Les nanogouttelettes d'hélium sont des clusters d'hélium liquide de taille finie et nanométrique utilisées depuis les années 90 comme matrice pour la spectroscopie à haute résolution de molécules. Les premières études spectroscopiques d'espèces ioniques à l'intérieur de gouttelettes d'hélium n'ont toutefois été réalisées qu'en 2010 malgré l'intérêt particulier qu'elles constituent en tant qu'intermédiaires fondamentaux de réaction en biochimie. De plus, l'interaction de ces espèces avec l'hélium environnant peut être déterminée à partir de ces expériences, ce qui est intéressant d'un point de vue fondamental.

Pour déterminer les informations structurales et étudier la sélectivité de réaction, nous avons proposé d'utiliser des champs électriques forts pour orienter les ions moléculaires dans les nanogouttelettes d'hélium. La spectroscopie des l'états pendulaires de molécules polaires neutres dans des nanogouttelettes d'hélium en présence de champs électriques a donné des résultats satisfaisants pour atteindre l'orientation moléculaire, permettant ainsi de distinguer les isomères biomoléculaires. Nos premières expériences ont validé la technique pour l'aniline neutre, car les rapports de différence de polarisation, exprimant le degré d'orientation, obtenus à partir des transitions d'élongations de NH_2 ont été bien reproduits par des calculs. Par contre, le degré d'orientation mesuré pour l'aniline cationique est nettement inférieur à celui indiqué par les calculs. Même dans ce cas, la variation du degré d'orientation avec le champ électrique nous permet de conclure que l'orientation des ions dans les gouttelettes d'hélium a été observée. Les résultats de plusieurs expériences réalisées pour étudier les effets possibles sur l'orientation apparente des cations n'ont pas conduit à une explication simple. Notre étude montre donc que l'orientation des ions moléculaires semble bien possible et ouvre la voie à de futures expériences.

Pour examiner la formation de complexes de solvation ioniques-alcalins dans des gouttelettes d'hélium lors de la photoionisation de l'alcalin, le sodium, et comprendre l'interaction hélium-dopant, nous avons effectué une étude par spectroscopie d'ions. Nous avons constaté que plusieurs scénarios sont possibles après l'ionisation, notamment la dissociation, la solvation et l'évaporation complète du solvant, en fonction du processus d'ionisation, de la taille des

gouttelettes et du nombre de ligands aqueux considérés. L'ionisation directe du sodium entraîne la solvatation de la gouttelette, suivie par des collisions avec les molécules d'eau et la formation de complexes ioniques si la taille de la gouttelette est suffisamment grande. Dans ces conditions, une expérience de spectroscopie rovibrationnelle de $\text{Na (OH}_2\text{)}^+$ a été réalisée pour obtenir la constante de rotation A dans les gouttelettes d'hélium et déterminer ainsi si l'interaction dopant-hélium affecte le moment d'inertie. À partir des résultats, nous avons pu confirmer que ce dernier est modifié, mais nous n'avons pas pu déduire une valeur quantitative de l'intensité de l'interaction dopant-hélium. Cette étude montre l'utilité des informations spectrales des ions solvatés pour comprendre la dynamique de complexation dans les gouttelettes d'hélium et approfondir les connaissances sur l'interaction dopant-hélium.

Mots clés:

gouttelettes d'hélium, superfluide, cluster, ion, spectroscopie, états pendulaires, effet Stark, sodium, aniline, complexe solvaté.

RESUMEN

Las nanogotas de helio son grupos de helio líquido de tamaño finito nanométrico que se han empleado desde la década de los noventa como una matriz para la espectroscopia de alta resolución de moléculas. Sin embargo, los primeros estudios espectroscópicos de especies iónicas dentro de gotas de helio no fueron realizados hasta 2010, a pesar de su especial interés como intermedios de reacciones fundamentales en bioquímica. Adicionalmente, estos experimentos permiten estudiar la interacción de estas especies con los átomos de helio de las nanogotas, lo cual es interesante desde un punto de vista fundamental.

Para determinar información estructural y, en última instancia, estudiar la selectividad de reacción, propusimos orientar iones moleculares en las nanogotas de helio utilizando campos eléctricos elevados. La espectroscopia de estados pendulares de moléculas polares neutras en nanogotas de helio ha dado previamente resultados satisfactorios, logrando orientar las moléculas y permitiendo así distinguir isómeros biomoleculares. En nuestros primeros experimentos se obtuvo el grado de orientación para la anilina neutra a partir de las transiciones de tensión de NH_2 . Estos resultados, de acuerdo con los calculados, validaron la técnica para orientar la molécula neutra. Por otro lado, el grado de orientación medido para la anilina catiónica es notablemente más pequeño de lo que muestran los cálculos. Aun así, la variación del grado de orientación con el campo eléctrico nos permite confirmar la orientación de los iones en las gotas de helio. Los resultados de varios experimentos realizados para investigar los posibles efectos que influyen en la orientación aparente de los cationes no llevaron a ninguna explicación directa. Sin embargo, nuestro estudio sugiere que la orientación de los iones moleculares es posible y abre el camino hacia experimentos futuros.

Para examinar la formación de complejos de solvatación iónicos-alcalinos en gotas de helio tras la fotoionización del alcalino, (en este caso, sodio), y comprender la interacción helio-dopante, hemos realizado espectroscopia de iones. Encontramos que son posibles varios escenarios después de la ionización, incluida la disociación, la solvatación y la evaporación completa del disolvente, y que estos dependen del proceso de ionización, el tamaño de las gotas y el número de ligandos de agua considerados. La ionización directa del sodio conduce a la solvatación en la gota,

colisionando con las moléculas de agua presentes y dando lugar a la formación de complejos iónicos si el tamaño de la gota es suficientemente grande. Bajo estas condiciones, se realizó espectroscopia roto-vibracional de $\text{Na}(\text{OH}_2)^+$ para obtener la constante de rotación A en las gotas de helio y así determinar si la interacción dopante-helio afecta al momento de inercia de la molécula. A partir de los resultados, pudimos confirmar esto último, pero no pudimos cuantificar el grado de interacción. Este estudio muestra cómo la información espectral de los iones solvatados es útil para comprender la dinámica de las reacciones de complejación en las nanogotas de helio y obtener una mayor comprensión sobre la interacción dopante-helio.

Palabras clave:

gotas de helio, superfluido, agregado, ion, espectroscopia, estados pendulares, efecto Stark, sodio, anilina, complejo solvatado.

CONTENTS

Abstract.....	I
Résumé	III
Resumen	V
1 Introduction.....	1
1.1 Helium.....	1
1.1.1 Different directions in quantum fluid clusters research.....	2
1.1.2 Molecular rotation in helium nanodroplets.....	3
1.1.3 Spectroscopy of ions in helium nanodroplets.....	7
1.2 Motivation	8
1.3 Outline.....	9
2 Experimental setup.....	11
2.1 Overview.....	11
2.2 Lasers	15
2.3 Methods.....	16
2.3.1 Excitation spectra.....	16
2.3.2 Ion-velocity map imaging.....	16
2.3.3 Time-of-flight mass spectra.....	17
3 Setup optimisation.....	19
3.1 Motivation	19
3.2 Reflectron time-of-flight spectrometer	19
3.2.1 Concepts.....	19
3.2.2 Design.....	22
3.2.3 Simulated ion trajectories and mass resolution.....	24
3.2.4 Experimental details.....	27

3.3	High-Voltage switch	29
3.4	Summary	30
4	Pendular state spectroscopy of molecular ions	31
4.1	Introduction	31
4.2	Concepts and methods.....	34
4.2.1	Coordinate system and orientation determination	34
4.2.2	Calculations of molecular orientation.....	36
4.2.3	Aniline.....	39
4.3	Experimental approach.....	43
4.3.1	Layout.....	43
4.3.2	Methods	44
4.4	Results	46
4.4.1	Neutral aniline.....	46
4.4.2	Cationic aniline	51
4.5	Summary	69
5	Ion spectroscopy of sodium ion water complexes	73
5.1	Introduction	73
5.2	Experimental approach.....	75
5.3	Support information and concepts.....	75
5.3.1	Pick-up probability and evaporative cooling loss	75
5.3.2	Sodium dimer and solvation complexes	79
5.4	Results	82
5.4.1	One laser experiments	82
5.4.2	Rovibrational spectroscopy of $\text{Na}(\text{OH}_2)^+$	93
5.5	Summary	105
6	Summary	109
7	References.....	113
	List of abbreviations.....	121

List of figures.....123

List of tables.....131

Acknowledgements..... A

Curriculum Vitae..... E

1 INTRODUCTION

Ionic species are fundamental intermediates in biochemical processes and acquiring knowledge and understanding of their structure and dynamics is therefore of special interest. Helium nanodroplets have proven to be an appropriate matrix to study them, providing high-resolution spectra^[1]. In this superfluid medium, molecular spectra show essentially the same structure as if they were free rotors^[1]. The molecular freedom to rotate in helium has been extensively studied and the role of the molecule-helium interaction disentangled^[2]. Ultimately, having control over this rotational motion in the medium could allow examining steric effects. The aim of the work enclosed in this thesis is to extend the methods to orient molecules in helium droplets to molecular ions by performing pendular state spectroscopy. Additionally, the effect of solvation on the ionic complex's initial rotation is studied as well as the formation and desolvation conditions.

1.1 HELIUM

Helium and its unique properties have been studied for over a century^[3]. It becomes liquid when cooled to very low temperature and is the only substance that remains liquid at normal pressure (it only solidifies above 25 bar^[4]) at absolute zero. Helium-4, the most abundant isotope, has a phase transition at the so-called 'lambda point' at 2.17 K, below which it behaves as a low density superfluid medium (He II state). Doping of nanosized superfluid helium droplets with atoms or molecules can be used as a probe to explore some of the physical properties of this quantum liquid such as quantised vorticity, almost zero viscosity or high heat conductivity^[5]. The weak interaction between helium atoms and dopants also makes it interesting to

be used as an inert cryogenic environment. Helium nanodroplets (HNDs, He_N), liquid finite size nanoscale helium clusters, have been employed since the 1990s^[6] as an alternative to the bulk superfluid since single embedding is achieved in a simple manner. Formed after a supersonic expansion of precooled helium, the clusters are directly doped by inelastic collisions of the beam with foreign species in the gas phase. The atoms/molecules are bound to the droplets via van der Waals forces and its position in the droplet depends on the required energy to arrive to the solvated state. For the dopant to localise inside the droplet some energy is required to create a cavity to accommodate the impurity and for this to happen the helium-helium interaction must be weaker than that between the dopant and helium. Calculating the dopant-helium solvation parameter considering the pair interaction potential allows predicting the equilibrium position^[7]. The dopants solvate if the parameter is greater than a critical value. Alkali and alkali earth atoms, used in this thesis, are predicted and known to be ‘inert’; i.e. they typically do not solvate but are located in a dimple at the droplet surface. The distinctive cluster temperature of 0.37 K is maintained after doping by evaporative cooling of helium to compensate for the pick-up energy, thereby also cooling down the impurity^[8-9]. Since radiation of energy below 20 eV does not interact with the helium^[10], light in the range of IR and visible-UV can be used to interrogate the cooled dopants without affecting it.

1.1.1 Different directions in quantum fluid clusters research

With the basis of this field established, several groups now use HNDs to examine physical and chemical phenomena. Different research directions investigate topics from the most intrinsic properties of helium such as quantised vorticity^[11-12] or ionisation of pure helium^[13] to intracluster reactions for which understanding of the solvation/desolvation mechanism^[14-17] of dopants is of interest. High-resolution spectroscopy of dopants is performed in helium droplets; spectra are barely shifted compared to that of gas phase and show rotational structure^[1]. Solute-solvent interaction and complex formation have also been studied^[18], though the lack of viscosity of helium leads to only weak interactions. This makes it an ideal isolation matrix in which reactions at cryogenic temperatures are examined. The molecule-helium interaction being weak, and in some cases smaller than the intermolecular interaction, favours condensation of species and reaggregation after dissociation. The resulting unstable molecules^[19], clusters^[20-21], and molecular radicals^[22]; which do not exist in gas phase due to rapid rearrangement into more stable structures,

are present in HNDs since the released energy by the process is quickly dissipated by the helium environment. Some studies then focus on probing these unique systems and their formation. In the area of formation of structures, some groups proved helium to be an appropriate medium in which to grow nanoparticles and nanowires^[23-24]. Successful removal of these clusters from the droplet^[25] opens the possibility of using this method for nanotechnology applications. Other experiments use helium to examine the formation of interstellar material by condensation in the low temperature matrix^[26]. Since the first doping experiments, a vast amount of studies has been performed looking at chemical dynamics and mechanisms of reactions and processes following excitation or ionisation, in some cases using ultrafast lasers. Either by ionisation of doped droplets^[14] or by pick-up of ionic species^[27] experiments have been performed on ionic systems. Using different methods several groups^[28-29] have achieved controlled orientation of the embedded molecules.

It is evident that spectroscopy in helium droplets is a well-developed field nowadays and cannot be fully covered in this introduction. To acquire a more profound overview, the reader is referred to the several reviews there are about specific areas^[22, 30-36], theoretical aspects^[37-39], and more general concepts^[5, 40]. Relevant for this thesis, in the subsections hereafter I will elaborate on the rotation of embedded molecules in HNDs and the studies of ionic dopants in helium.

1.1.2 Molecular rotation in helium nanodroplets

In the first spectroscopic experiments, the cluster temperature was determined and superfluidity could be confirmed^[8, 41-43]. The infrared (IR) spectra of a vibrational transition of sulphur hexafluoride was rotationally resolved and indicated almost full rotational freedom of the molecule in the helium matrix. A very enlightening experiment was performed by Grebenev et al. in 1998^[1], in which spectra of an OCS molecule in helium-3 were recorded as helium-4 atoms were sequentially added. After 60 units, the atoms would surround the molecule and rotational resolution appeared, indicating superfluid behaviour (Figure 1-1^[1]).

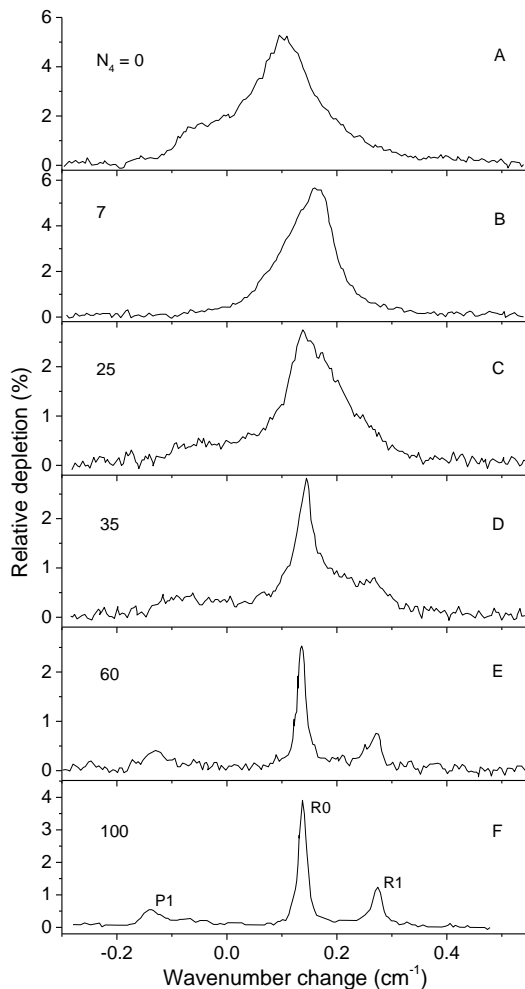


Figure 1-1. Spectra of OCS in ^3He as the average number of added ^4He atoms (N_4) is increased. The spectrum in ^3He (A) shows a broad band that results into sharp rotational features for $N \geq 60$ (E and F). ν_θ is at 2061.71 cm^{-1} . Taken from [1].

Though the molecular spectra exhibit fine structure similar to that of free rotors, the moments of inertia for solvated molecules change pointing to some coupling of helium with dopants. Two distinct behaviours are observed. For heavy molecules, with rotational constants below 0.5 cm^{-1} [44], the moments of inertia are increased in helium and the rotational constants are generally decreased by a factor of three compared to gas phase. In the case of light molecules, which are fast rotors with rotational constants much larger than 1 cm^{-1} [30, 44], their rotational constants in the lack and presence of helium are almost the same. This seems to indicate that helium affects to a different degree molecular rotation depending on how fast this is. Several models were suggested to explain the larger moments of inertia. In a simplistic way, one could think that some helium atoms surrounding the molecule

follow its motion and contribute to the moment of inertia, like a molecule-helium complex^[8]. This rigid classic approximation is an easy concept to understand coupling but seems inaccurate since the surrounding density is delocalised and dynamical exchange between helium atoms is expected. More realistic models have been developed since. One of the main approaches, the *two fluids* model, suggests a non-superfluid helium fraction and a superfluid helium fraction that coexist in the droplet^[44-45]. The non-superfluid fraction is caused by the interaction with the dopant and is situated in its vicinity contributing to its rotation. The total moment of inertia is then defined as a sum of the free molecule's moment of inertia; that of the non-superfluid helium distributed around the molecule, and the superfluid helium component caused by the molecule's rotation. This last contribution, the hydrodynamic term, considers the perturbation by the molecule to the surrounding superfluid to cause a backflow. This last term is assumed to be small^[1]. The second main approach, the *hydrodynamic* model, is based on this concept and unlike the former model considers the hydrodynamic term to be significant^[30, 46-47]. It assumes helium's density to be only superfluid and its kinetic energy proportional to the squared angular velocity of the molecule. By considering the variation of helium's density around the dopant, this contribution to the moment of inertia becomes important and defines the difference between the free molecule's inertia and the solvated molecule's. This density variation is also taken into account in the *two fluids* model, included in the non-superfluid term. Both approximations consider helium's density anisotropic and assume that some fraction of helium's density in the first solvation layer follows the molecule's rotation adiabatically. The degree of helium's contribution to the moment of inertia explains the solvated rotational constants of heavy and light molecules pointing to different degrees of transfer of the angular momentum of the molecule to the solvent. Nevertheless, both dynamical models are based on solvating helium density profiles calculated around static molecules that are then assumed to be similar when in motion, an assumption that fails when dealing with fast rotors. Direct calculations of the energy levels of the clusters containing the molecule, based on rotationally excited dopants, can complement these models^[2, 48-49]. The results confirm that helium's density is considerably more delocalised when the molecule is in motion. Figure 1-2 (a) ^[44] illustrates it in the case of SF₆. In agreement, a more isotropic density is obtained when considering higher rotational constants of the same molecule, see Figure 1-2 (b) ^[49]. While computationally more expensive and thus limited to small systems of tens of atoms, direct calculations allow understanding of the change in the

rotational constants from the free molecule to the quantum solvated molecule. Comparison to experiments in which the number of helium atoms has been fixed up to tens^[50-53] has enabled concluding that the first solvation shell is not completely coupled to the dopant's rotation and that it is indeed a partial adiabatic following in which helium's density is anisotropic. The values of rotational constants first decrease as the number of helium atoms increases and then undershoot to converge at a different number depending on the molecule. As the droplet size increases, the contribution of the helium-helium interaction becomes more important competing with the molecule-helium interaction. This indicates that direct calculations of the molecule attached to one helium atom in the absence and inclusion of rotation can estimate the molecule-helium interaction but cannot describe to what extent the molecule's angular momentum will affect helium's density of a large droplet. The moment of inertia upon solvation is determined by the anisotropy of the molecule-helium interaction potential, rather than the molecular weight.

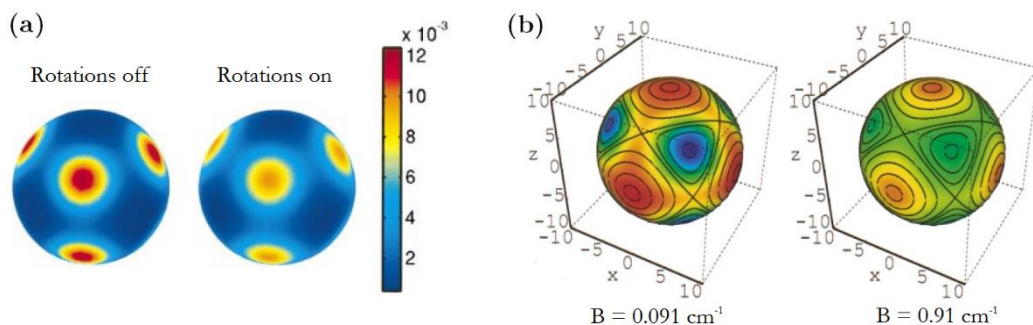


Figure 1-2. Ground state wave function obtained from Monte Carlo calculations (a) of helium for a nonrotating (left) and rotating (right) SF_6 molecule projected in the molecular frame at 4.25 Å from the molecule; (b) of $^4\text{He}_8\text{SF}_6$ projected at 8 a.u. radius when the gas phase rotational constant (B) (left) and a ten times larger B value (right) are used. In (b), the colour scale uses blue to represent high values and red for low ones. A more isotropic density is obtained for rotating SF_6 . Higher rotational constants result in an even more isotropic density. Reprinted from (a) ^[44], (b) ^[49].

Rotation of molecular ions in HNDs

The contribution of helium to the moment of inertia becomes more important when the dopant is ionic due to stronger coupling. For ionic aniline, a heavy rotor, the rotational constants in HNDs have been found to decrease by a factor of nine compared to gas phase^[14]. It seems reasonable to think of a greater degree of dopant-helium interaction caused by the ionic charge. Consequently, it would be interesting to find out whether this ion-helium interaction can already modify the moments of

inertia of what are normally considered light rotors. Unfortunately, no information could be extracted from experiments on HCl^+ and ionic acetylene performed in this group to this purpose^[54]. To our knowledge, experiments of this sort have not been explored otherwise and the outcome remains unanswered.

1.1.3 Spectroscopy of ions in helium nanodroplets

Spectroscopic investigations of ions in HNDs were reported for the first time in 2010 by this group^[14]. To create ion-containing droplets two different approaches can be taken: (i) ionisation of neutral doped droplets^[14] or, (ii) direct doping with ions^[27].

After dopants are subjected to ionisation, some are directly ejected while some remain in the droplets. Exciting the ions remaining in the droplets, either vibrationally or electronically, causes their desolvation^[14]. By choosing appropriate pump-probe delays and gating the ion detector, the bare ions generated by the photoionisation can be excluded to provide background-free signal of photoexcited, mass-selected ions. This method has proven applicable for ions generated by both non-resonant and resonant-enhanced ionisation^[14, 16]. Although the method is limited to molecules that can be doped, those which are either in gas phase or can be evaporated, it has proven to be effective for performing spectroscopy of ions.

Electrospray ionisation has been put forth to produce and dope helium droplets with mass-to-charge selected ions^[27]. After selecting the ions produced by standard electrospray with a quadrupole filter, they are sent into an ion trap cell. The droplets, generated with a pulsed source, collide with the ions exceeding the trapping potential energy and leaving the cell to arrive to the detector. Coupling with a laser system allows spectroscopy of the doped ions. This method enables investigation of large biomolecules, for which thermal evaporation is not possible without causing decomposition/fragmentation.

With these two methods, isolated ions at low temperatures have been spectroscopically studied after vibrational^[14, 16, 55] and electronic^[15, 56-57] excitation. The helium medium induces shifts of 1-2 cm^{-1} and up to tens of cm^{-1} in the bands position after vibrational and electronic excitation of ions respectively, similar to the typical displacements found for neutrals in HNDs, and clear structure confirming helium as an ideal matrix to study ions. Some of the studies focused on unravelling the desolvation mechanism following ionisation and excitation of the species^[14-16]. Other studies focused on structural characterisation^[55, 58], since

assigning molecular ions structures might be key to understand biochemical processes.

Experiments on ions have pointed out lower ionisation energies in HNDs than in the gas phase^[59]. This shift is caused by solvation effects; the surrounding medium is slightly polarised by the ionic dopant.

Desolvation mechanism of ions from HNDs

Photoexcitation of the ions leads to their desolvation from the droplet. This process is a combination of helium evaporation and ion ejection. After excitation, a number of helium atoms proportional to the energy deposited into the droplets by the relaxation of the excited molecule is evaporated. But bare ions have been observed for sufficiently large droplets sizes for which a thermal process of this sort could not lead to complete droplet disintegration. As an example, bare ionic aniline has been observed after photoexcitation of doped helium droplets of ~ 3000 atoms when the vibrational energy is calculated to lead to evaporation of 700 helium atoms^[14]. This evidences that direct ejection of the ions is governed by a non-thermal mechanism, a process that does not occur for neutral molecules and for which understanding is still lacking. The efficiency of ion ejection decreases with droplet size, pure ejection is favoured for smaller droplets ($N \leq 3000$) whereas complete desolvation in large droplets is mainly a result of a two-photon process via smaller ion-He_N clusters formation.

1.2 MOTIVATION

The moments of inertia of molecular ions were expected to increase upon solvation in HNDs to a larger degree than for neutrals due to stronger coupling with helium and this has been confirmed experimentally for a heavy molecule^[14]. Studies on light ionic molecules have not given any clear conclusions about whether this coupling is strong enough to change the moments of inertia more significantly than in the case of neutrals^[54]. Part of this thesis focuses on the rotation of an ionic complex formed after ionisation of a surface located atom colliding with a light solvated molecule. Sodium is known to solvate upon ionisation^[60-61]. In this case, the rotation of a complex formed among water (embedded) and ionic sodium as it solvates upon ionisation is examined. The formation and desolvation of ionic sodium water complexes upon sodium ionisation for different droplet sizes and number of water ligands are also investigated.

Several methods have already been developed to control molecular rotation achieving a determined orientation in HNDs^[29, 62]. With them, molecular structures could be determined and the effect of molecular orientation in chemical reactivity could be examined and steered. Pendular state spectroscopy of neutral polar molecules in helium droplets in the presence of electric fields has given satisfactory results confirming the abilities of the method being capable of distinguishing biomolecular isomers^[63]. Here, the goal is to extend the method to achieve orientation of molecular ions. The presence of HNDs allows the ions to remain in the field for long enough to perform spectroscopic studies with a probe pulse before being repelled by the electrostatic interaction as it would happen in gas phase. For this purpose, ionic aniline is used as a proof-of-principle. The dependence of the degree of orientation on several factors is examined and the results supported by simple calculations.

The goal of this thesis is then to extend the understanding about ionic species in HNDs and develop techniques that can facilitate control over them to acquire further knowledge about the species themselves. The methods and experimental setup employed to perform these experiments are detailed in the next chapter.

1.3 OUTLINE

The thesis is structured in the following manner. In Chapter 2, the main features of the experimental setup comprising the helium droplet beam machine and lasers, and the different employed techniques are described. In Chapter 3, the reflectron detection stage is explained in further detail. The experimental modifications to make it operational are accompanied with updated simulations and some experimental working values as reference for future experiments. Chapter 4 examines molecular ion orientation, where pendular state spectroscopy on ionic aniline is performed and the influence of several experimental conditions considered. The results are compared with neutral aniline. Values from calculations help discussion of the achieved degrees of orientation. Chapter 5 describes research on ionic sodium solvation complexes inside helium droplets. Spectra around the ionisation energy of sodium are recorded to examine solvation of ionic sodium followed by solvation by different size water clusters. The rotational dynamics of the monosolvated ionic complex in helium droplets are determined by rovibrational spectroscopy. A summary of the main results of this work along with future experiments suggestions are in Chapter 6.

2 EXPERIMENTAL SETUP

2.1 OVERVIEW

The scheme of the helium droplet beam machine and the main components of the experimental setup used in the experiments is shown on Figure 2-1. With it, photoionisation phenomena were observed in and on helium nanodroplets and pump-probe experiments were performed in this research work. The technical details and detailed description of the setup can be found elsewhere^[64]. Since construction, some modifications were carried out^[54, 60, 65]. Updated information about the latest modification, i.e. the addition of a second detection stage^[65], is reported in chapter 3. Below, an overview of the main setup characteristics is given.

Pure helium gas (purity 6.0) at a pressure of 30 bars is cooled to 11-22 K and expanded through a nozzle of 5 μm into vacuum. Under these conditions, helium nanodroplets of 1000-20000 atoms are formed depending on the temperature at the nozzle (detailed below). The beam then passes a 0.3 mm-diameter skimmer before entering the doping chamber. In this region, a leak valve and a high-temperature oven are situated so the droplets can be either doped by high or low vapour pressure substances. The pressure of the species is adjusted so each droplet picks up the correct amount of atoms/molecules (pick-up probability is explained in section 5.3.1). The doped droplet beam reaches the detection chamber after passing through a differential pumping stage, which is used in double pick-up experiments and to attain ultra-high vacuum and thus reduce the effusive beam in the detection region. The composition of the beam is monitored by means of a quadrupole mass

spectrometer (QMS; QMG422, Balzers), which is located at the end of the detection chamber.

The species in or on the droplets are irradiated at the intersection between a perpendicular incoming beam laser and the molecular beam at the centre of one of the two detection stages in the detection chamber. First in the direction of the molecular beam there is the velocity map imaging (VMI) stage after which the reflectron stage is placed. Voltages at the interaction regions accelerate and send the charged particles to the detectors. The detection set of the VMI stage includes a micro-channel plate (MCP) and a phosphor screen (PS). At the reflectron stage a microsphere plate (MSP) and a micro-channel plate together with a phosphor screen are placed at the top and coaxial to the flight tube ion entrance for different operational modes. With those, position and arrival time at the detector are resolved. Charge-coupled device (CCD) cameras (A202K, Basler AG and piA1000-48gm, Basler AG respectively) placed at the back of the PSs record single-shot images that can be integrated for longer times for improved statistics. The electrical signal on the phosphor screens is sent to an oscilloscope (WaveSurfer 104MXs-B, Teledyne LeCroy) or a multiple event time digitizer (P7886, FAST ComTec GmbH). If the front MCP plate is gated by switching the applied voltages (HTS 31-GSM and HTS301-03, Behlke), mass-selected information can be obtained.

General descriptions of the different employed techniques are found below. Specific conditions for every experiment are given in the results chapters (4.3 and 5.2).

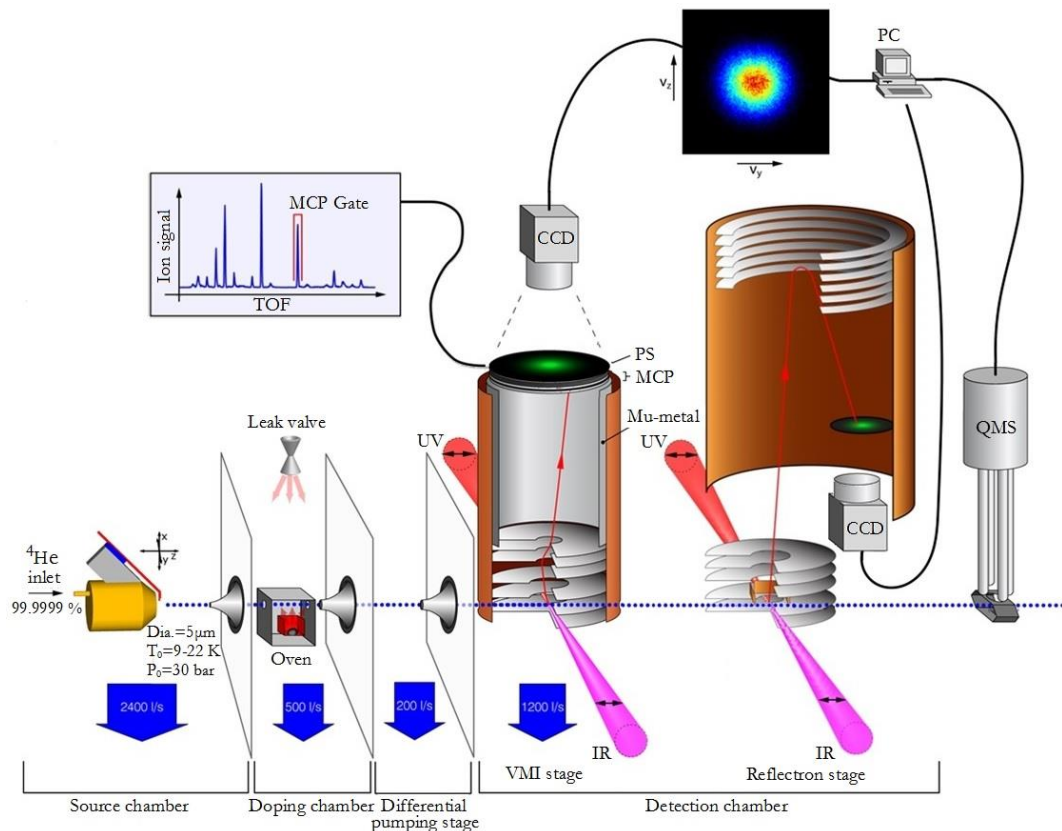


Figure 2-1. Illustration of the main components of the experimental setup. The blue dots show the trajectory of the helium droplet beam. The red lines show the ion trajectories in the time-of-flight mass spectrometers.

Cluster source

The helium-4 molecular beam is obtained from a supersonic jet expansion of precooled pure helium gas (purity 6.0) through a nozzle of $5\text{ }\mu\text{m}$ into vacuum. To cool the helium gas, between 5 K and 25 K , a closed-cycle refrigerator system consisting of a cold head (RDK-205D, Sumitomo Heavy Industries) and a compressor unit (CKW-21A, Sumitomo Heavy Industries) is used, providing continuous cooling. The gas cools on its way to the nozzle in two steps, as it makes thermal contact with the two cold head stages. To measure and stabilise the temperature, two silicon diodes (DT-70-CU-13, Lake Shore Cryotronics) and a temperature controller (Model 336, Lake Shore Cryotronics) are used. The droplets can be produced by subcritical, critical and supercritical expansion of the gas^[66]. Under the source conditions used here (30 bar , $13\text{--}19\text{ K}$, $5\text{ }\mu\text{m}$ nozzle diameter), helium droplets are formed by condensation in a subcritical regime expansion^[66].

Droplet size distribution

Different size droplets are formed depending on the stagnation temperature; the lower the temperature is, the bigger they are. But the droplet size in the cluster beam is not fixed. The number of helium atoms per droplet N follows a log-normal distribution $f(N)$, which is expressed as^[67-68]:

$$f(N) = \frac{1}{N\delta\sqrt{2\pi}} e^{-\frac{(\ln N - \mu)^2}{2\delta^2}} \quad (2.1)$$

where δ and μ are the standard deviation and mean of the natural logarithm size distribution which can be transformed into the mean droplet size $\langle N \rangle$ and its standard deviation S calculated:

$$\langle N \rangle = e^{\mu + \frac{\delta^2}{2}} ; \quad S = \langle N \rangle \sqrt{e^{\delta^2} - 1} \quad (2.2)$$

The mean droplet sizes for different nozzle temperatures previously estimated^[64] are in Table 2-1 knowing that the radius r [Å] is related to the number of helium atoms N by^[69]:

$$r = r_0 \sqrt[3]{N} \quad (2.3)$$

and taking $r_0 = 2.22$ Å as the unit radius of ^4He .

Table 2-1. Mean number of helium atoms per droplet ($\langle N \rangle$) and droplet radius ($\langle r \rangle$, [Å]) at different nozzle temperatures (T , [K]).

T (K)	$\langle N \rangle$	$\langle r \rangle$ (Å)
22	1100	23
21	1370	25
20	1710	27
19	2150	29
18	2750	31
17	3540	34
16	4620	37
15	6080	41
14	8080	44
13	10860	49
12	14710	54
11	20060	60

2.2 LASERS

Several laser systems have been used to perform the experiments described in this thesis. Dye lasers pumped by the second or third harmonic of pulsed Nd:YAG lasers (1064 nm fundamental) have been used for resonance-enhanced multiphoton ionisation (REMPI) in the UV. In this case, two different pairs have been used: 1) a PrecisionScan SL (Sirah Laser-und Plasmatechnik GmbH) pumped by a Quanta-ray Pro 250 (Spectra-Physics Lasers) and 2) a NarrowScan (Radiant dyes Lasers) pumped by a Quanta-Ray GCR-170 (Spectra-Physics Lasers). The repetition rates were 20 Hz and the pulse length 7-9 ns. The outputs were doubled using KDP or BBO crystals depending on the frequency. An output of several mJ per pulse was typically obtained. A half-wave plate enables rotation of the initial horizontal polarisation (parallel to the droplet beam axis). The Nd:YAG lasers were also used standalone to perform non-resonant ionisation with the fourth harmonic at 266 nm. Fused silica lenses with focal lengths of 400 and 500 mm were used to focus the beams. For the IR, an Optical Parametric Oscillator (OPO) and Optical Parametric Amplifier (OPA) from LaserVision pumped by the fundamental of a GCR-270-20 (Spectra-Physics Lasers) Nd:YAG laser at 10 Hz were used. A home-made frequency stabilization unit^[54] ensures single-shot precision over time. The frequency is read out with a WS5 High Finesse wavemeter of 0.1 cm⁻¹ accuracy and

recorded after being stabilised in a feedback loop. A tunable output between 712-880 nm and 1.35 -5 μm can be produced. The output in the mid-IR region ($< 5 \mu\text{m}$, idler) has horizontal polarisation that can be rotated with a half-wave plate. The power is frequency dependent; an output up to 8 mJ per pulse was typically obtained in the experiments. A nitrogen purging system was included in the beam path to minimise IR absorption by water vapour. A barium fluoride (BaF_2) lens with a focal length of 400 mm was used to focus the IR beam.

2.3 METHODS

2.3.1 Excitation spectra

The excitation spectra reported in this thesis have been recorded using various detection schemes. In all cases the spectra are recorded by monitoring the number of ions arriving at the detector per laser shot as a function of the excitation frequency. These spectra can be recorded mass-specifically since the arrival time is specific for every mass, being proportional to the square root of the mass-to-charge ratio. By gating the detector on a specific time interval (defined by arrival time and duration), mass specific spectra can be recorded. At the same time, the gating minimises any background signal. By gating the detector it also becomes possible to discriminate between ions generated by the pump and probe lasers. However, for some experiments the time delay between the pump and probe lasers is so small that signals cannot be gated separately. For such cases, background subtraction is performed by using different laser repetition rates. The selection of a spatial region of interest (ROI) on the detector allows for a further reduction of any residual background signal.

2.3.2 Ion-velocity map imaging

Ion speed distributions or kinetic energies can be obtained by velocity map imaging (VMI). Ions generated at different source positions within the laser and molecular beam intersection impinge on the detector at the same spot for a specific repeller to extractor voltage ratio (1:0.707 give the optimum resolution) if they have the same velocity (and charge and mass). This separates the species by velocity creating a 2D projection (map) of the 3D velocity distribution. After inverse Abel transform^[70], the 3D distribution of recorded integrated ion images is reconstructed^[71]. Velocity and kinetic energy distributions can be obtained using appropriate calibration factor values.

The kinetic energy T [cm²] is related to the radius R [pixel] by^[64, 72]:

$$T = C \cdot q \cdot V_R \cdot R^2 \quad (2.4)$$

where C [cm⁻¹ · eV⁻¹ · pixel⁻²] is the calibration factor, q [e] is the ion charge and V_R [V] the repeller voltage.

In this thesis, all images were recorded at 2000 V on the repeller plate. A calibration factor equal $1.397 \cdot 10^{-4}$ cm⁻¹ · eV⁻¹ · pixel⁻² [54] was used.

From 3D reconstructions to kinetic energies

After Abel inversion, details about the used procedure are in [64, 71], the 3D distribution is expressed as a velocity distribution in one dimension $P_v(v)$ and an angular distribution in two dimensions $P_\vartheta(v, \vartheta)$ product^[64, 73]. The ‘velocity space’ over all directions gives the speed distribution $P_s(v)$, which is proportional to the squared velocity ($P_s(v) = v^2 \cdot P_v(v)$). The kinetic energy distribution $P_e(T)$ is obtained from the speed distribution ($P_s(v)dv = P_e(T)dT$ from particle conservation).

$$P_e(T) = \frac{1}{mv} P_s(v) = \frac{v}{m} P_v(v) \quad (2.5)$$

Where v and m are the fragment velocity and mass.

From the kinetic energy distribution the average kinetic energy is calculated as:

$$\langle E_{kin} \rangle = \frac{\int T \cdot P_e(T) dT}{\int P_e(T) dT} \quad (2.6)$$

2.3.3 Time-of-flight mass spectra

Time-of-flight (TOF) mass spectra are recorded in the velocity map imaging stage by sending the electrical signal from the phosphor screen (triggered by the laser) to a multiple event time digitizer. A maximum mass resolution of 100 is obtained for 1:0.45 repeller to extractor voltage ratio. In this work the repeller voltage was set to 5 kV to record species of mass up to 1000 amu. Single-shot flight distributions are averaged to improve statistics and corrected for UV intensity.

3 SETUP OPTIMISATION

3.1 MOTIVATION

As part of this work several modifications were necessary to make the reflectron time-of-flight (TOF) stage of the setup operational. The mass spectrometer was designed and built by a former student of the group but never tested^[65]. Additional parts necessary for experiments were installed and SIMION[®] simulations on which the original design was based were refined. The apparatus was designed to achieve higher mass resolution than the linear TOF installed in the first stage of the detection chamber as well as adding new experimental possibilities. One of them was to include an interaction region capable of handling static and pulsed electric fields in the range of $60 \text{ kV} \cdot \text{cm}^{-1}$ to perform pendular state spectroscopy. Further details about this method are described in chapter 4. Addition of a high-voltage (HV) switch allows selecting the arrival time and duration of the pulsed field.

In this chapter the principles of the spectrometer and its design are described, and the outcome of simulated ion trajectories detailed. The experimental steps and modifications and a set of working voltage values are reported. Lastly, some specifications about the high-voltage switch are given.

3.2 REFLECTRON TIME-OF-FLIGHT SPECTROMETER

3.2.1 Concepts

The time-of-flight of ions accelerated by an electric field can be related to the mass-to-charge ratio (m/z) of the species by the following expression^[74]:

$$t = d \sqrt{\frac{m}{2Uq}} \quad (3.1)$$

where d [m] is the total flight path distance, q [C] is the elementary charge, m [kg] is the mass of the ion, t [s] is the flight time and U [V] the applied voltage.

The mass resolution (R) of a TOF mass spectrometer is defined as^[74]:

$$R = \frac{1}{2} \frac{t}{\Delta t} \quad (3.2)$$

where t is the minimum total flight time it takes to the ion to arrive to the detector and Δt is the time distribution of all possible trajectories.

When using a laser pulse to generate the ions, several factors can broaden their flight times leading to limited mass resolution. The formation time of the ions within the pulse length leads to pure temporal spread (Figure 3-1 left a). Additionally, the ions are produced at slightly different positions in the laser focus size (Figure 3-1 left b) and thus arrive at the detector at different times determined by their different potential energies. In a simple linear TOF instrument this energy spread can be alleviated by placing the detector in the field-free region where ions are intrinsically focused. The ions that are created further away from the detector experience higher potential energies and thus they overtake the slower ones at some specific point in space called the (first-order) space focus (x_{sf}), see Figure 3-1 right. For a dual-stage (three electrodes) ion source^[75] the position of the space focus can be shifted, allowing further (second-order) correction and minimising the time distribution. With these corrections, there still exists a broadening factor due to the pure kinetic effect. To correct for it, an energy compensating means is needed.

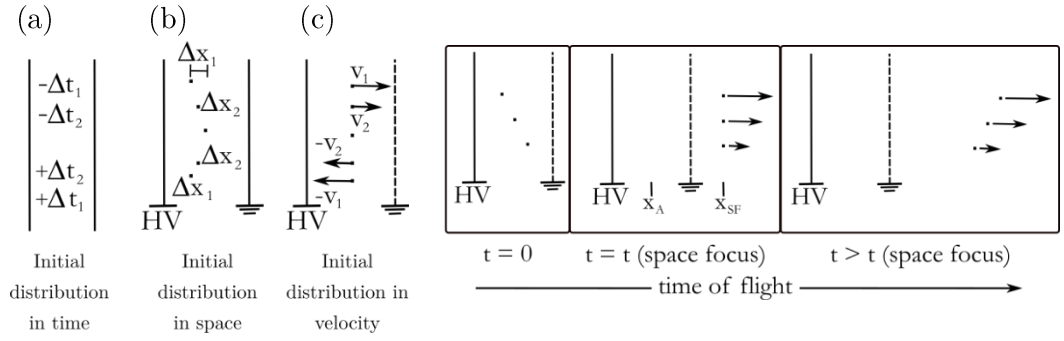


Figure 3-1. Left: Initial distribution of the ions produced by the laser in a field (HV) and in terms of temporal (t), spatial (x) and velocity (v) distributions factors contributing to an initial distribution. Right: Illustration explaining (first order) space focus. At time zero the ions are spread and start moving by the field. The distance from these positions to the ground electrode is x_A . At some point, called the space focus x_{SF} , the faster ions overtake the slower ones ($x_{SF} = 2x_A$). The simultaneity is lost after the space focus. Taken from [74].

Such a means is provided by a reflectron TOF mass spectrometer^[76]. A reflectron usually comprises a pulsed ion source, a field-free region, an ion mirror and an ion detector (Figure 3-2). Ions are formed in the ion source obtaining kinetic energy and then enter the ion mirror, which is a series of evenly spaced electrodes onto which a potential is applied. Then, they travel up the potential hill to the point that matches the energy obtained from the source. Once stopped, the ions return back down thanks to the electric field applied to the ion mirror that reverses the direction. The detector is positioned on the entrance side of the ion mirror to capture the ion arrival after being reflected.

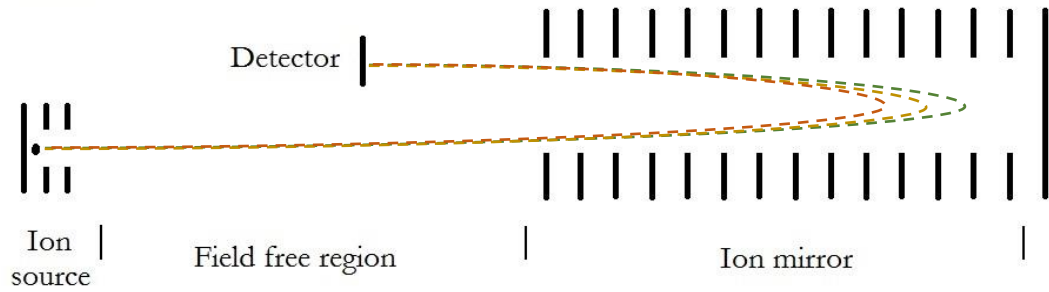


Figure 3-2. Schematic representation of the reflectron time-of-flight apparatus showing its different components. Ions with different kinetic energies would follow different trajectories (dashed lines) in the ion mirror; for greater kinetic energies they arrive faster to the ion mirror but penetrate deeper (in green) into the field traveling a longer flight path and resulting in similar total flight times.

This layout diminishes the spread of flight time of the ions with same mass-to-charge ratio but different kinetic energies and also enables distinguishing between ions of similar mass-to-charge ratio. Ions with greater kinetic energy arrive at the ion mirror first but penetrate deeper into the field, i.e. travelling a longer flight path, than ions with less kinetic energy and thus both arrive at the detector at nearly the same time (Figure 3-2). The increased length of the flight path results into longer flight times leading to a larger temporal separation between ions of similar but different m/z . As a result, the width of the flight time is only determined by the pure temporal ion formation spread.

3.2.2 Design

A side view of the reflectron TOF mass spectrometer is shown on Figure 3-3. A microsphere plate detector at the end of the ion mirror enables using it as a linear TOF spectrometer; the ion trajectory for this operational mode is shown in red. The blue dashed line shows the typical trajectory in the reflectron mode used in the experiments. The detector consisting of a micro-channel plate with phosphor screen is positioned coaxial to the entrance side. To record images of the ions, a CCD camera is mounted to the back of the MCP detector. The ion mirror consists of fourteen equally spaced electrode plates interconnected by resistors. The first one is grounded and voltages are applied to the 5th and the 14th electrodes creating the field that reverses the direction of the ions.

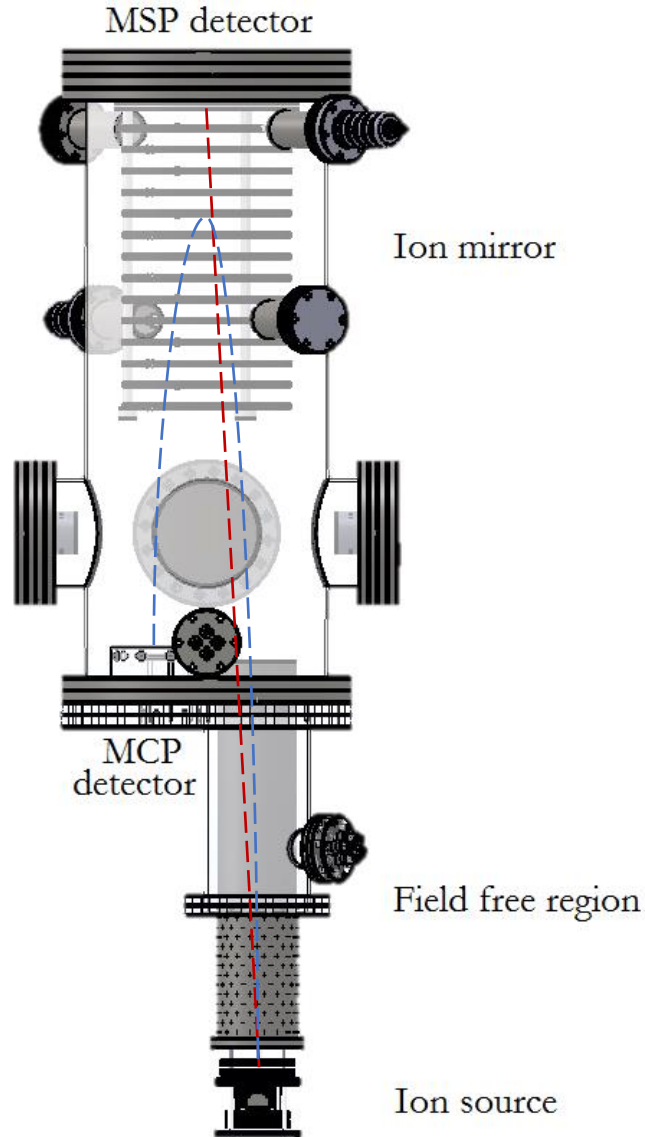


Figure 3-3. SOLIDWORKS side view of the built reflectron time-of-flight mass spectrometer viewed from the helium nozzle to the quadrupole mass spectrometer of the machine. The design allows linear and reflectron TOF configurations. The ion trajectories for each are shown in red and blue dashed lines respectively.

Figure 3-4 shows the ion source in detail. It is set up so the laser beams intersect the helium beam at the centre between the repeller and extractor electrodes. At this position, an electric field created by these electrodes accelerates the ions. Then, four deflector electrodes and an Einzel lens consisting of three electrodes are used to guide and resize the ions before entering the field-free region.

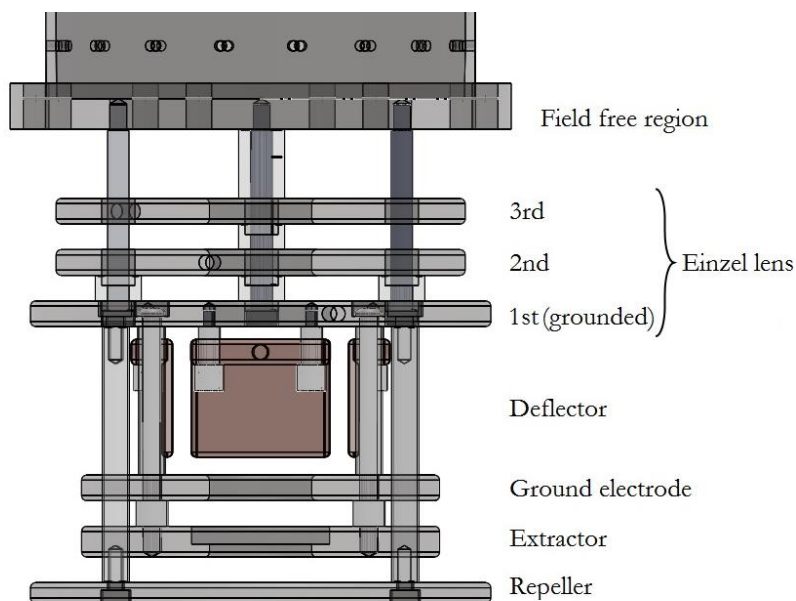


Figure 3-4. SOLIDWORKS side view of the ion source.

Further details including connections, feedthroughs, dimensions and components' materials are described in reference^[65].

3.2.3 Simulated ion trajectories and mass resolution

After initial test of the reflectron TOF spectrometer it was noted that the initial design of the apparatus was based on simulations that did not consider a field-free time-of-flight tube and the presence of the nickel mesh placed on the extractor electrode was neglected. As a result, the spectrometer did not function as expected, i.e. the estimated mass resolution and working voltages were incorrect. Simulations using the SIMION[®] software package (version 8.1.2.28) were performed to calculate the actual achievable values. The dimensions were imported into the software from the 3D CAD-model used to construct the setup. A LUA code was written to find optimum voltages that would lead to best mass resolution and performance (most ions splatting on the detector). The starting positions of the ions are defined by the intersection between the laser and the molecular beam. An approximate laser radius of 0.25 mm and a molecular beam diameter of 2 mm are used to define a cylindrical distribution of the set number of particles.

Table 3-1. Input parameters used to simulate the ion trajectories in SIMION®. The y, z, x axes are defined in the direction of the laser beam, the molecular beam, and perpendicular to them respectively.

Particle group starting conditions		
Volume distribution: radius, length (mm)	0.25, 2	
Starting position: x, y, z centre (mm)	120.165, 173.54, 36	
Initial speed (mm/μs)	0.45	
	Dual-stage	Single-stage
Number of particles	1000	100
Mass (uma)	200	93
Charge (e)	1	1

For a dual-stage operational mode, the voltage of the repeller is fixed to 5 kV to find the optimum extractor voltage. 1000 singly-charged particles of 200 uma with an initial velocity in the direction of the molecular beam are used as input to carry out the simulations. All parameters are listed in Table 3-1. With this input, a maximum mass resolution of 1002 is found at the detector. The corresponding voltages are reported in Table 3-2. Figure 3-5 shows the trajectories the ions follow at these values. This mass resolution is significantly lower than typical reflectrons, up to 30000 ^[77-79], due to the mistakes in the original design.

Table 3-2. Optimum calculated voltages for dual-stage ion source operation of the designed reflectron time-of-flight spectrometer for a 5 kV repeller voltage.

Ion source	Deflector	Einzel lens	Ion mirror
	Front: 0		
Ground: 0	Back: 30	1 st : grounded (0)	1 st grounded (0)
Extractor: 4300	Right: 1340	2 nd : 1500	5 th 2500
Repeller: 5000	Left: grounded (0)	3 rd : grounded (0)	14 th 6500

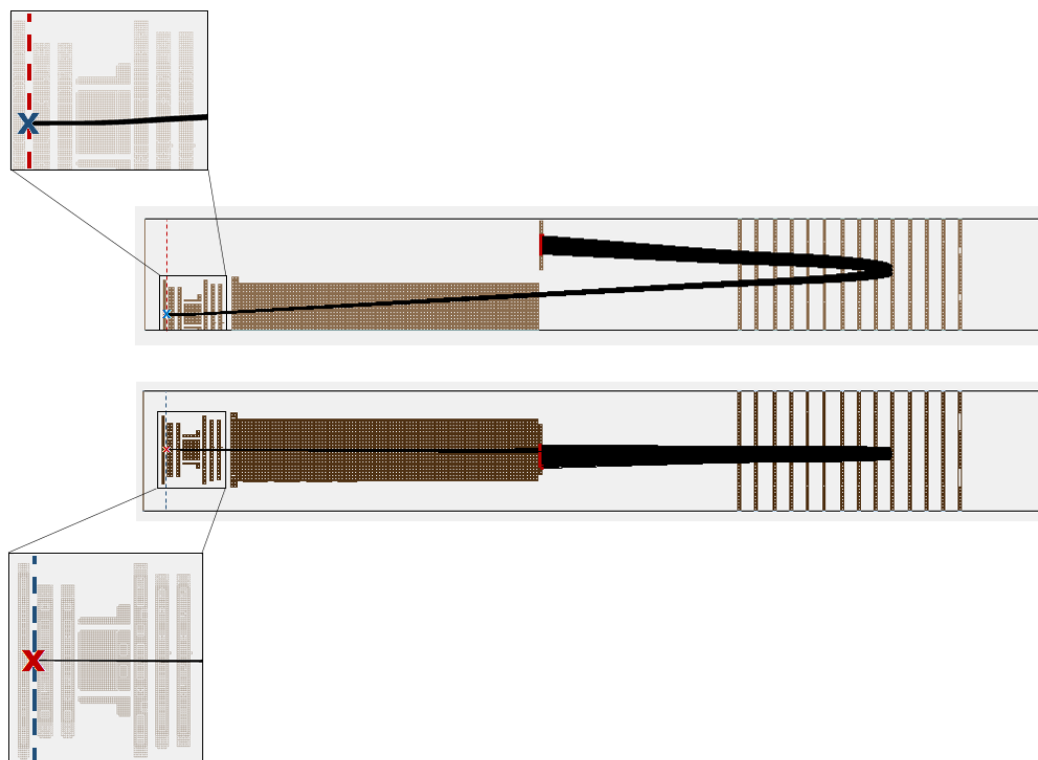


Figure 3-5. Simulated trajectories of ions of 200 uma at $60 \text{ kV} \cdot \text{cm}^{-1}$ in the reflectron TOF with an initial velocity in the molecular beam direction in a dual-stage type ion source. The blue and red dashed lines represent the molecular beam and laser beam respectively. Top: viewed from the molecular beam to the quadrupole mass spectrometer of the machine. Bottom: viewed in the direction of the laser, perpendicular to the molecular beam.

For pendular state spectroscopy, a single-stage ion source is considered. In a dual-stage ion source the field between the first two plates is smaller than in between the second two. To be able to apply electric fields up to $60 \text{ kV} \cdot \text{cm}^{-1}$ in the first-stage, the required voltages would be prohibitively large. The simulation is performed by fixing the repeller and extractor at 30 kV and 0 kV respectively. Since the first experiments in the setup will be on aniline, singly-charged particles of 93 uma with an initial velocity in the direction of the molecular beam are input. All parameters are in Table 3-1. The maximum mass resolution at the detector is 267. The output voltages are in Table 3-3. Figure 3-6 shows the ion trajectories under these conditions.

Table 3-3. Optimum calculated voltages (for a $60 \text{ kV} \cdot \text{cm}^{-1}$ electric field) to perform pendular state spectroscopy using the designed reflectron time-of-flight spectrometer.

Ion source	Deflector	Einzel lens	Ion mirror
	Front: 0		
Ground: 0	Back: 200	1 st : grounded (0)	1 st grounded (0)
Extractor: 0	Right: 4300	2 nd : 1000	5 th 10000
Repeller: 30000	Left: grounded (0)	3 rd : grounded (0)	14 th 25000

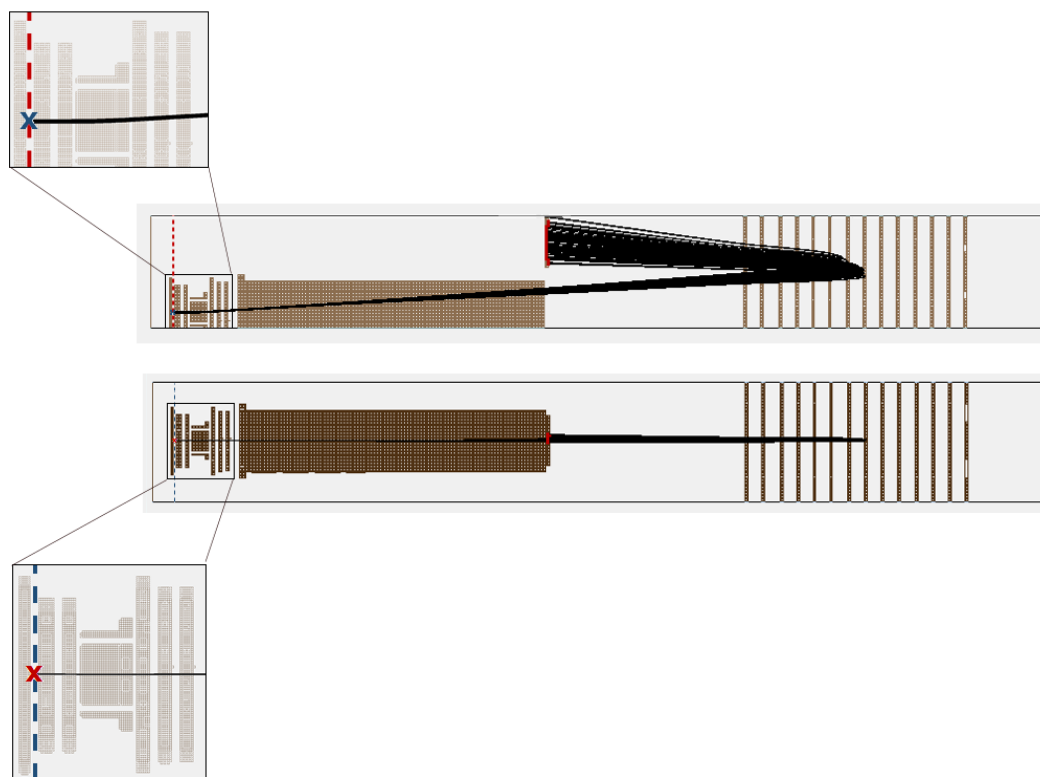


Figure 3-6. Simulated trajectories of aniline ions at $60 \text{ kV} \cdot \text{cm}^{-1}$ in the reflectron TOF with an initial velocity in the molecular beam direction in a single-stage type ion source. The blue and red dashed lines represent the molecular beam and laser beam respectively. Top: viewed from the molecular beam to the quadrupole mass spectrometer of the machine. Bottom: viewed in the direction of the laser, perpendicular to the molecular beam.

3.2.4 Experimental details

To make the stage operational, the following was accomplished:

Proper wiring of the plates in the ion mirror was ensured after including a missing resistor to ground the first electrode. A metallic isolation box and hose

were installed along with new insulated wires from the feedthrough to the MCP to avoid the ion trajectories to be deviated by the applied voltages on the detector. High-voltage feedthrough protections have been designed and included. Grounding of the stage was ensured, which is essential when working with electric fields of this magnitude.

Two sets of window mounts were installed to send the laser beams into the ion source. Light baffles were included to prevent electrical discharge caused by the laser beam hitting the repeller and extractor electrodes. The mounts include a differentially pumped sealing system to ensure ultra-high vacuum is achieved in the detection chamber.

A detection camera was installed coaxial to the entrance side of the ion mirror at the back of the MCP and phosphor screen, see Figure 3-3. The designed mount allows ambient light shielding between the detector and the camera.

After the required upgrade and voltage conditioning, the simulated voltages above were taken as a reference to find the best experimental signal. Table 3-4 comprises the optimum voltages found for the highest applied electric field used in the experiments (pendular state spectroscopy of aniline in chapter 4). The values are in reasonable agreement with the calculated ones reported in Table 3-3. A mass resolution of 210 was found.

Table 3-4. Optimum experimental voltages (for a $60 \text{ kV} \cdot \text{cm}^{-1}$ electric field) to perform pendular state spectroscopy using the designed reflectron time-of-flight spectrometer.

Ion source	Deflector	Einzel lens	Ion mirror
	Front: 835		
Ground: 0	Back: 1065	1 st : grounded (0)	1 st grounded (0)
Extractor: 0	Right: 4260	2 nd : 2000	5 th 9170
Repeller: 30000	Left: grounded (0)	3 rd : grounded (0)	14 th 22600

3.3 HIGH-VOLTAGE SWITCH

To enable applying a pulsed orienting electric field, a high-voltage switch was installed. A custom-made device using the push-pull transistor switch HTS301-03 from BEHLKE[®] was designed and built by the institute's electronic workshop. Connecting it to a delay generator (TTL signal) allows pulse length and arrival time control. Easily exchanged components allow two operational modes (Figure 3-7^[80]). In the first configuration 'positive-positive' the polarity stays the same; a positive voltage is applied and then switched to a greater value. Example: a voltage of 1 kV is applied and then switched at a selected time to 30 kV during the pulse duration. For the second configuration 'negative-positive' (also employed for zero to positive) the voltage polarity is inversed throughout operation. Example: a negative voltage of 1 kV is applied and then switched to positive 30 kV. The green line on Figure 3-8 shows the square wave high-voltage output. The rise time of the generated pulse is on the order of 100 ns.

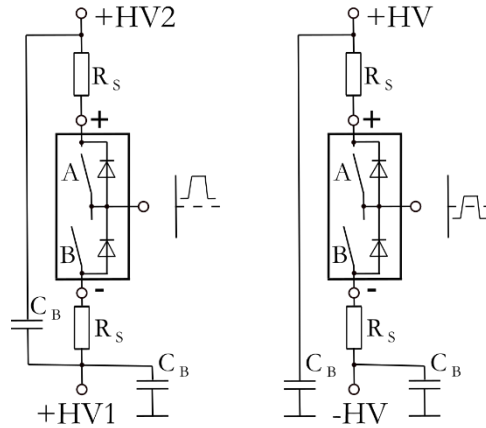


Figure 3-7. Circuits of the two operational modes of the HV-switch. Left: scheme employed for switching between positive voltages. Right: Employed for negative-positive fields. R_s : series resistors, C_B : capacitor, A: switching off-state path, B: switching on-state path. Taken from BEHLKE^[80].

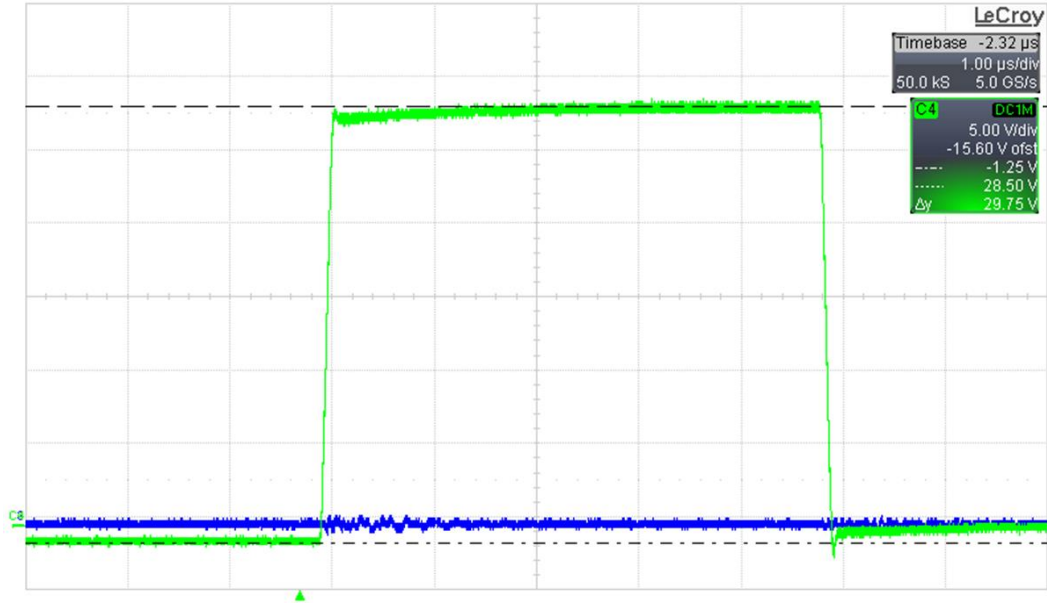


Figure 3-8. Measured voltage output (in green) on an oscilloscope from an initial voltage of zero switched to 30 kV generated by the installed HV-switch. A 1000:1 probe is employed to measure it. Each horizontal division corresponds to 1 μ s and every vertical to 1 kV. The rise time is on the order of 100 ns and the pulse length is 5 μ s.

3.4 SUMMARY

In this chapter updated information about the reflectron TOF mass spectrometer in the setup is presented. Simulations considering the installed mesh on the extractor and a field-free region allowed estimation of the limitations and specifications of the built apparatus. Voltage values for single- and dual-stage type ion sources are found and taken as a reference together with the updated mass resolutions. Proper wiring of the ion mirror and electric isolation of the MCP detector allowed the ions to arrive at the detector at voltages fairly close to the simulated values. After installation of the missing components, conditioning and characterisation, the setup was used to perform pendular state spectroscopy experiments, the results of which are covered in chapter 4. In addition, specifications about the installed high-voltage switch together with the measured wave output are included.

4 PENDULAR STATE SPECTROSCOPY OF MOLECULAR IONS

4.1 INTRODUCTION

The purpose of the research reported in this chapter is to orient molecular ions in helium droplets using an electric field. To aid understanding, orientation of neutral molecules is also examined.

To start with, we would like to recall the difference between alignment and orientation. Whereas alignment (\leftrightarrow) does not discriminate head to tail (the molecules can be parallel or antiparallel to the reference), orientation (\rightarrow) restricts the directionality completely. The orientation of molecules prior to reaction is key in product selectivity, and therefore the ability to control it allows understanding and manipulation of stereochemical reactivity. Since the 1960s several methods have been developed and are employed nowadays to orient molecules.

The first steric experiment studied the reaction of rubidium with methyl iodide^[81] in Bernstein's group. This method employs a hexapole focusing field, sometimes a guiding field and an orienting field to control the orientation of polar molecules^[82]. The molecules in a molecular beam are sent through a hexapole which is used to [rotational] state-select and focus those states exhibiting a positive Stark effect. The rest of the molecules are dispersed or not influenced. The selected molecules are then transferred to the collision/detection region by the guiding field, which retains their polarisation, and finally oriented in the laboratory frame by a weak (10s of $\text{V} \cdot \text{cm}^{-1}$) homogeneous electric field^[81, 83]. This technique is mostly limited

to linear and symmetric top molecules with permanent dipole moments since hexapoles cannot select single quantum states of asymmetric top molecules at achievable electric fields.

Since it was suggested by Zare^[84], optical fields have been used to generate aligned molecules. Back then, photoexcited molecules whose transition dipoles were parallel to the electric field of a resonant linearly polarised laser were aligned. Restricted to alignment, this method also requires system-specific photon energies and prior knowledge of the transition dipole moment's direction. But non-resonant laser alignment is also possible. The interaction between an intense optical field and the induced dipole moment results in alignment of any anisotropically polarisable molecule^[85]. Moreover, the laser field technique can increase the control of molecules to their 3D alignment using elliptically polarised light, which can be adapted to the molecule's polarisation, to fix all three axes^[29]. Generally, the use of continuous wave and pulsed lasers, or the pulse duration of the latter, differentiates adiabatic and non-adiabatic alignment. Adiabatic alignment is produced while the laser field is on if the field duration is longer than the molecules' rotational period^[85]. Pulse durations down to nanoseconds can be used in this approach. When the pulse is shorter, rotational wave packets can be formed. In this non-adiabatic regime, the molecules are aligned in field-free conditions right after the laser pulse or at revival times of the wave packets^[86-87].

The method we will use to perform our experiments was first named 'brute force' orientation^[88]. It requires that the interaction of an electric field with the dipole moment of the molecule exceeds the average rotational energy of the molecule. In the 1970s, the required magnitude of the applied field (1000s of $\text{kV} \cdot \text{cm}^{-1}$) was considered experimentally impossible even for systems with large dipole moments^[88]. However, gas-phase molecules can be rotationally cooled by supersonic expansions to several kelvin ($<10 \text{ K}$)^[89]. At this temperature, only the lowest rotational levels are populated allowing orientation of any polar molecule with moderate fields (10s of $\text{kV} \cdot \text{cm}^{-1}$) since the 1990s^[90-91]. As the electric field strength increases, the motion of the molecule goes from a rigid rotor to that of a pendulum: the permanent dipole moment is restricted to librate within a small angle about the applied field. The interaction (Stark effect) makes the rotational states mix and hybridise into so-called 'pendular' states^[92]. For these reasons this technique is also referred as Stark or pendular state spectroscopy.

Pioneered by Miller^[62, 93], the orientation of neutral polar molecules in helium droplets in the presence of electric fields was utilised by several groups^[63, 94-101]. The temperature of the dopants in the droplets reaches 0.37 K after evaporative cooling^[8-9], decreasing the rotational energy and allowing orientation to be observed at weak fields. Moreover, the rotational constants of heavy molecules^[30] and ions^[14] are substantially reduced in helium droplets indicating slower rotation and enhancing orientation. Looking at the direction of the vibrational transition moments with respect to the permanent dipole, different tautomers of several nucleic acid bases were distinguished^[63, 94-98]. Electronic spectroscopy of molecules embedded in helium droplets has also enabled identification of conformers and determination of their transition dipole moment directions^[99-101].

We aim to apply this technique to molecular ions in order to assign the excited spectra to their corresponding conformers. To do so, the molecules need to remain in the excitation region upon ionisation for long enough to permit excitation. Orientation of molecular ions in the gas phase is generally unfeasible due to the electrostatic interaction between the ionic charge and the field that would rapidly eject them from the excitation region before excitation. The helium medium increases the time the ions stay in the excitation region up to hundreds of nanoseconds. The ion remains in the helium droplet in a metastable state that cannot be held forever and out of which it can escape by a small increase of energy, like the one produced by the excitation pulse (probe pulse photon energy). The possibility of using high electric fields to orient ions embedded in helium droplets is explored with aniline.

In this chapter, the results of the experiments performed with this purpose are reported. First, some concepts and methods useful to understand and discuss the results are discussed. Then the results are examined. The first part of the results comprises electronic and vibrational polarisation spectroscopy of neutral aniline in helium droplets comparing both the experimental and calculated results. The second part reports our findings for aniline cations in which the effect of several experimental conditions was examined, together with the calculated results.

4.2 CONCEPTS AND METHODS

4.2.1 Coordinate system and orientation determination

To describe the orientation of molecules one has to use the appropriate coordinate systems. The z-axis of the laboratory frame is defined by the direction of the applied electric field. When a polar molecule is placed in the field, the molecule tends to rotate to align its permanent dipole moment in the direction of the field (see Figure 4-1 ^[102]).

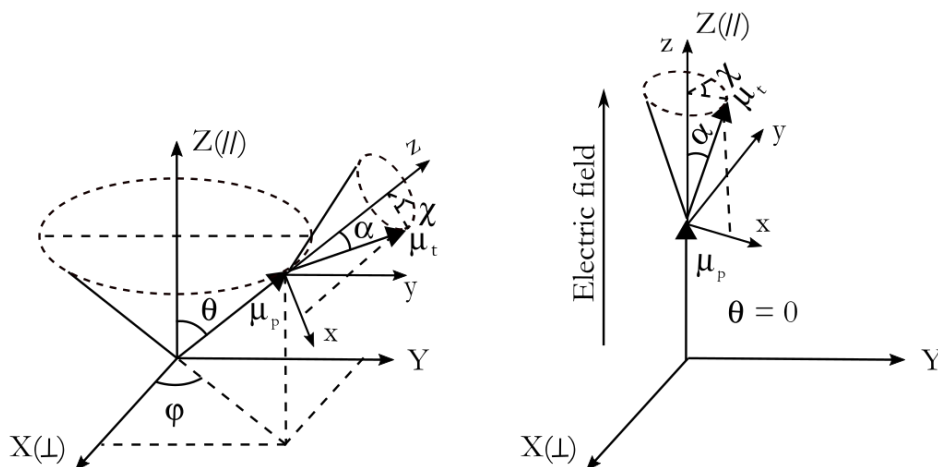


Figure 4-1. Left: Coordinate system illustrating the laboratory frame (X, Y, Z) and the molecular frame (x, y, z). In the molecular frame, the permanent dipole, μ_p , is chosen to be the z axis and the transition dipole, μ_t , is set to be within the x-z plane. θ is the angle between the laboratory frame and the molecular frame, ϕ is the projection of this angle on the X-Y plane and, α is the angle between the permanent dipole moment and the transition dipole moment. Right: when the electric field is applied the permanent dipole moment orients in its direction ($\theta = 0$). Reprinted and adapted with permission from ^[102].

This orientation of the dipole moment can be probed by selected vibrational and/or electronic transitions, since the absorption probability of a transition depends on the relative orientation of the transition dipole moment with the polarisation vector of the light^[103]. The probability is greatest when the dipole moment of the transition is aligned with the laser polarisation vector^[104]. Since the transition dipole moment makes a fixed angle with the permanent dipole moment, which lines up in the electric field, the intensity of the transition depends on the angle between the electric field and the laser polarisation. For a transition dipole moment parallel to the permanent dipole moment, the intensity of the band is enhanced when the laser field is aligned parallel to the applied electric field since the transition dipole moment is in the direction of the light. On the other hand, if the alignment of the

laser field is perpendicular to the static field, the absorption probability of the transition decreases and the band intensity is diminished, see Figure 4-2 (a)^[63]. In contrast, Figure 4-2 (b) shows the case where the behaviour is reversed. The angle is close to 90° and consequently the enhancement occurs when the laser field is perpendicular to the static field and vice versa. In this method there is also a ‘blind’ angle. When the transition dipole moment is at the so-called magic angle, 54.7° , with respect to the permanent dipole moment, the absorption probability shows no polarisation dependence^[105].

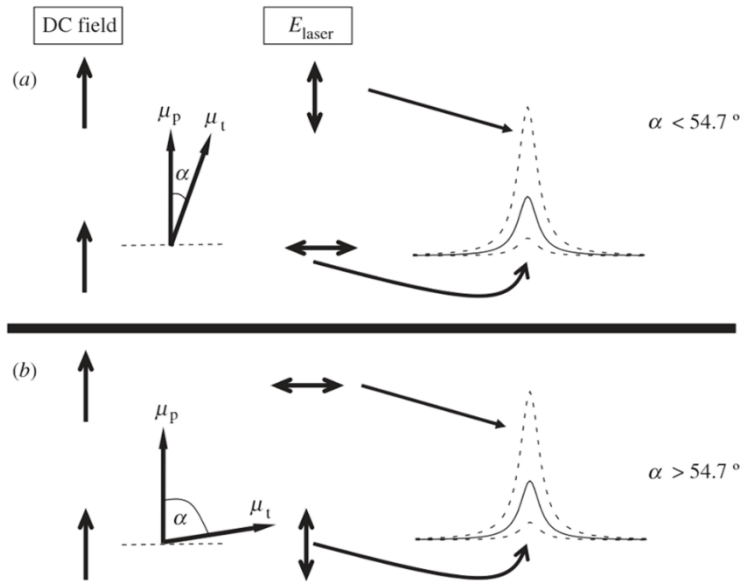


Figure 4-2. Effect of an electric field on the transition intensity as a function of the laser polarisation direction. The solid line represents the spectra at zero field. μ_p is the permanent dipole moment, μ_t is the transition dipole moment and α the angle between them. Reprinted with permission from ^[63].

Throughout this chapter, the laser polarisation is defined with respect to the laboratory frame axis, i.e. the electric field direction, independent of the transition dipole moment direction.

In order to express the orientation, the polarisation difference ratio will be employed:

$$P = \frac{A_{\perp} - A_{\parallel}}{A_{\perp} + A_{\parallel}} \quad (4.1)$$

where A_{\perp} (A_{\parallel}) is the integrated area of the transition with laser polarisation perpendicular (parallel) to the electric field. With this definition the degree of orientation can take values from +1 when $A_{\perp} \gg A_{\parallel}$ to -1 when $A_{\parallel} \gg A_{\perp}$, while it equals zero for an isotropic distribution, in the absence of an orientation effect.

Knowing the directions of the transition dipole moments with respect to the permanent dipole moment of the molecule allows foreseeing under which laser polarisation the band intensity will increase.

4.2.2 Calculations of molecular orientation

The interaction of the permanent dipole moment of a molecule with an electric field changes the molecule's motion from a rigid rotor to that of a pendulum, i.e. the permanent dipole moment is restricted to librate within a small angle about the applied field, see Figure 4-3^[106]. This causes splitting of the degenerate rotational levels into lower and higher energy levels, called pendular states.

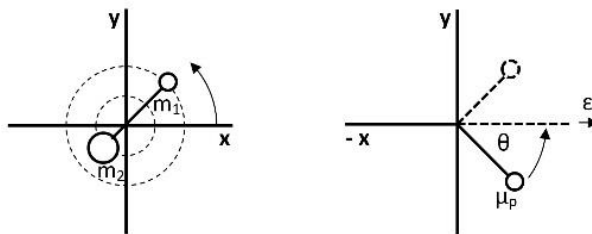


Figure 4-3. Left: Motion of a two-particle rigid rotor. Right: Stark pendulum, the dipole moment of the molecule (μ_p) is trapped by the applied electric field (ϵ) in a libration motion. Adapted from reference ^[106].

To estimate the molecular orientation in the electric field one has to find the energies of these pendular states. Kong et al.^[107] explain in detail the methodology for calculating the orientation of asymmetric top molecules in a uniform electric field where the permanent dipole moment (μ_p) is not parallel to any principal axis. The entire mathematical treatment is beyond the scope of this thesis. Instead, I will only indicate the basis of their approach that we use for our calculations.

Briefly, the rotational Hamiltonian is modified to consider the asymmetry of the molecule and the Stark effect that is present when an electric field (ϵ) is applied:

$$H = H^{asym} + H^{Stark} = A\hat{J}_z^2 + B\hat{J}_x^2 + C\hat{J}_y^2 - \mu_p\epsilon \quad (4.2)$$

where A, B, C are the rotational constants and \hat{J}_i ($i = x, y, z$) the x, y, z components of the angular momentum operator in the molecular frame.

In order to solve the Schrödinger equation, the linear variational method^[108] is used. Using the calculated energies of the molecule and taking into account the selection rules for the correspondent transitions, the spectral transitions are predicted. The orientation is then calculated from the intensities of the bands using (4.1).

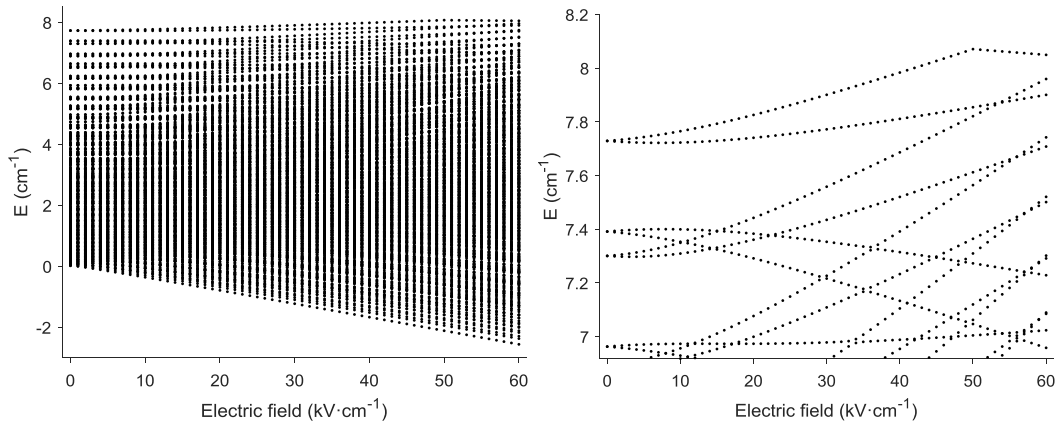


Figure 4-4. Calculated splitting and shifting of the energy levels when the dipole of aniline cation interacts with an electric field ($J = 20, m = 1$). The rotational constants are divided by nine. Right: Enlarged y axis to observe the splitting in detail.

Figure 4-4 highlights how the rotational levels split and hybridise as the electric field increases into pendular states. The final population of the molecular states depends on whether the transfer from field free to high field is adiabatic or non-adiabatic. The adiabatic case assumes the population and order of the energy levels to remain the same. The non-adiabatic treatment transfers the population to the most similar final state corresponding to minimum changes. In both cases some metastable levels will be populated. If the species in these levels remain in the electric field for long enough, relaxation to lower levels is possible yielding a thermal distribution. For the calculations in this thesis, thermal population is assumed since best agreement with experiments was previously observed^[109-110].

The shape of the band can also give information about the orientation of the molecule in the field. As the increasing Stark effect mixes the rotational levels, the band shape is distorted. This effect has been previously observed for the H-F stretch of acetylene-HF^[110]. Figure 4-5 shows the calculated spectra obtained using the method developed by Kong et al. as a function of electric field. When the molecules become oriented in the field, the band intensity increases when the laser field is parallel to the transition dipole. As the field increases, the structure collapses into a pendular feature near the vibrational band origin. When the laser polarisation is perpendicular to the transition dipole, the region corresponding to the pendular features appears empty. The structure splits to the sides with increasing electric field, and the intensity increases notably less than in the parallel case^[63, 110].

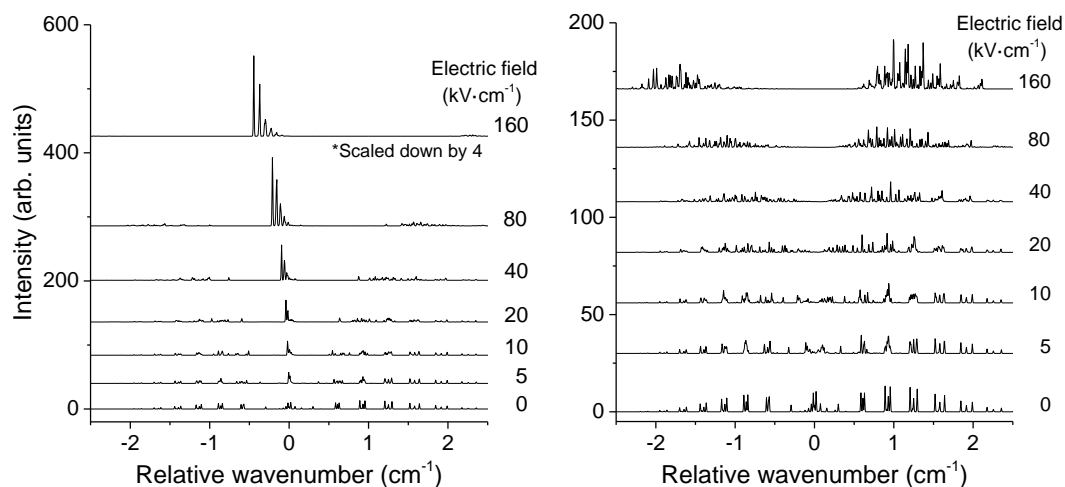


Figure 4-5. Calculated spectra of the H-F stretch in acetylene-HF (parallel to the permanent dipole moment) from 0 to 160 $\text{kV} \cdot \text{cm}^{-1}$ resulting for (left) parallel (right) perpendicular laser polarisation.

Practical information

The ab initio input rotational constants and permanent dipole moments of aniline and ionic aniline are gathered in Table 4-1 and Table 4-3. The rotational constants are divided by a factor of three and nine for the neutral molecule and the molecular ion respectively unless otherwise specified, to take into account the dopant-helium interaction^[14, 30]. The orientation of the transition dipole moment with respect to the permanent dipole is also obtained from the computed geometry, and is input to perform the calculations.

4.2.3 Aniline

The simple structure of aniline and aniline cation makes them ideal to examine orientation once the directions of the transition dipole moments with respect to the permanent dipole moment are known. Whereas the spectroscopy of the aniline molecule has been extensively studied, much less is known about the spectroscopy of ionic aniline. To treat both systems on an equal basis we have calculated using the Gaussian 09^[111] programme suite: the geometry, rotational constants, permanent dipole moments, vibrations and excited states by Density Functional Theory (DFT) and Time-Dependent (TD) DFT using the B3lyp functional and a 6-311++G(df,pd) basis set. Calculations using the same methodology have revealed good agreement with experimentally available spectroscopic data^[112], thereby justifying this approach.

4.2.3.1 Neutral aniline

Ab initio calculations reveal that the structure of aniline in its ground state is non-planar (C_s), with a 40 degrees angle between the amino group and the ring plane, in agreement with experimental results^[112]. The permanent dipole moment is found to be 1.607 D and its direction in the molecular frame is shown in Figure 4-7 (a). The A, B, C axes of inertia correspond to X, Y, Z of the molecular frame. The corresponding rotational constants are gathered in Table 4-1.

Table 4-1. Calculated values of rotational constants [cm^{-1}] and permanent dipole moments [D] of aniline by DFT and TD-DFT using B3lyp functional and a 6-311++G(df,pd) basis set in Gaussian.

	A (cm^{-1})	B (cm^{-1})	C (cm^{-1})	μ_p (D)
Ground state, S_0	0.1885	0.0868	0.0595	1.607
Excited state, S_1	0.1787	0.0883	0.0591	1.80

The IR spectrum of aniline is characterised by two strong absorptions at 3422 cm^{-1} and 3509 cm^{-1} corresponding to the symmetric and antisymmetric NH_2 -stretch vibrations respectively^[113]. The intensities are calculated to be very similar for both transitions^[112], see Table 4-2, in agreement with experiment. The directions of the transition dipole moments are however different; whereas the direction of the symmetric stretch vibration is parallel to the permanent dipole moment, the antisymmetric is perpendicular (see Figure 4-7 (b) and (d)).

Table 4-2. Vibrational wavenumbers ($\tilde{\nu}$ [cm^{-1}]) and molecular absorption coefficients (a [$\text{km} \cdot \text{mol}^{-1}$]) for both the symmetric and antisymmetric stretch of aniline.

	$\nu_{\text{sym}}\text{NH}_2$	$\nu_{\text{asym}}\text{NH}_2$
$\tilde{\nu}$ (cm^{-1})	3422	3509
a ($\text{km} \cdot \text{mol}^{-1}$)	20	17

The $S_1 \leftarrow S_0$ electronic transition in aniline not only has been studied in the gas phase, but also in helium droplets. Figure 4-6 compares the spectrum recorded in the gas phase versus that in helium droplets^[59]. Due to the interaction with the helium, the individual vibronic transitions are substantially broadened and blue shifted with respect to the gas phase^[114]. Whereas in the gas phase the band origin is located at 34030 cm^{-1} , in helium droplets it has its maximum at 34100 cm^{-1} . The calculations reveal the quasi-planar structure of aniline in the S_1 state and indicate that the transition dipole moment is perpendicular to the permanent dipole moment, represented by the blue arrow on Figure 4-7 (c).

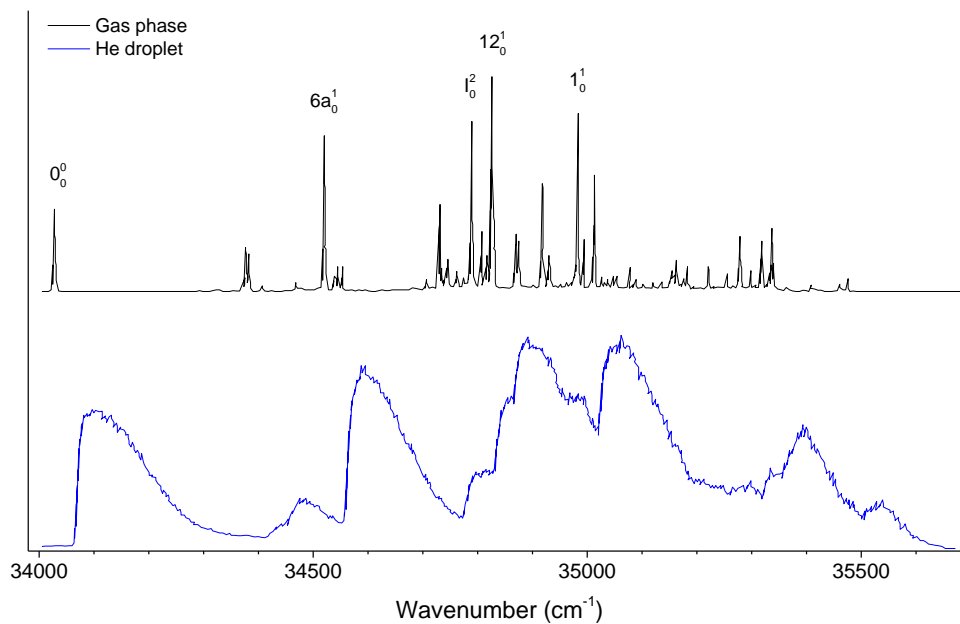


Figure 4-6. Excitation spectra ($S_1 \leftarrow S_0$ (1+1)-REMPI) of aniline in the gas phase (top) and in helium droplets (bottom) for a droplet size of 41 \AA . Taken from ^[59].

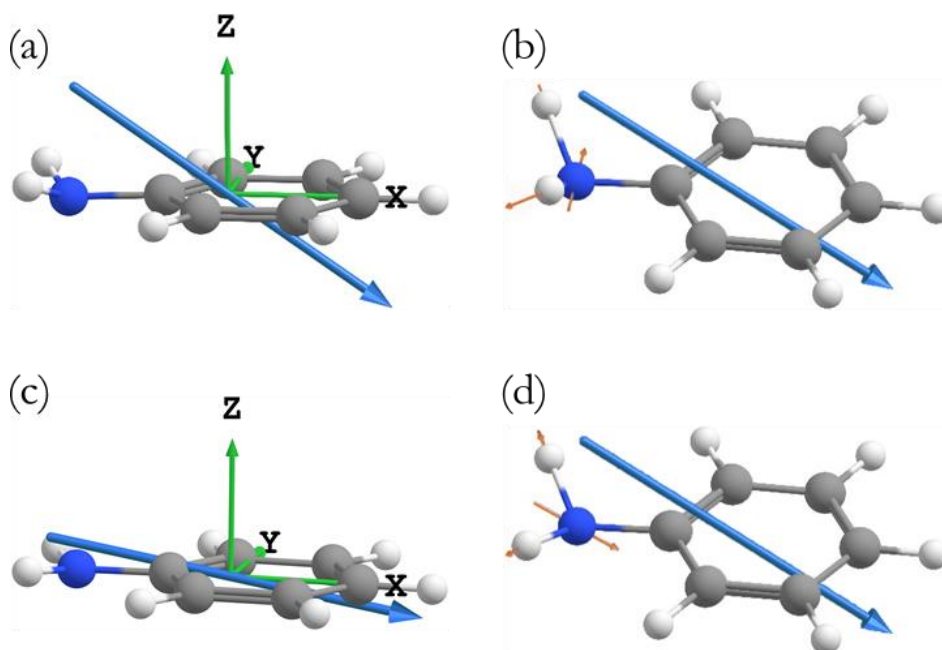


Figure 4-7. (a) Structure of aniline in the ground state showing the molecular frame axes (in green) and the permanent dipole moment direction (in blue). (c) Structure of aniline in the S_1 state showing the molecular frame axes (in green) and the permanent dipole moment direction (in blue). Right: direction of the displacement vectors (in orange) contributing to the antisymmetric (b) and symmetric (d) transition dipole moments.

4.2.3.2 Ionic aniline

The characteristic non-planarity of amino groups is not present for the aniline radical cation in its ground state, whose symmetry group is C_{2v} (planar) (Figure 4-8). This geometrical structure is reproduced by the calculations, which yield a permanent dipole moment of 2.77 D pointing along the C_2 axis, i.e. the X axis in the molecular frame. The corresponding rotational constants are reported in Table 4-3.

Table 4-3. Calculated values of rotational constants [cm^{-1}] and permanent dipole moment [D] of ionic aniline by DFT using B3lyp functional and a 6-311++G(df,pd) basis set in Gaussian.

	A (cm^{-1})	B (cm^{-1})	C (cm^{-1})	μ_p (D)
Aniline cation	0.1803	0.0898	0.0599	2.77

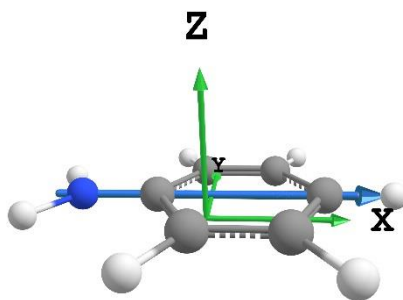


Figure 4-8. Structure of aniline cation showing the molecular frame axes (in green) and permanent dipole moment direction (in blue).

The IR spectrum of the aniline cation in helium droplets has been studied in the past by the group^[54]. The spectrum in the near infrared shows three transitions, see Figure 4-9. The two strong transitions at 3395.1 cm^{-1} and 3488.8 cm^{-1} correspond to the symmetric and antisymmetric NH_2 -stretch vibrations respectively, while the weak band at 3270.6 cm^{-1} corresponds to a scissoring overtone. The shift of the transition frequencies between the gas phase^[115] and in helium droplets^[54] is only of 2 cm^{-1} for the symmetric and of 3 cm^{-1} for the antisymmetric stretch vibrations. The scissoring overtone was assigned based on the fundamental scissoring vibrational of aniline- Ar^+ at 1635 cm^{-1} ^[116]. In helium droplets, a value of 1648.3 cm^{-1} was found^[54]. The effect of the laser intensity on the width pointed out a minimum width of 1.6 cm^{-1} for the NH_2 -stretch and 0.4 cm^{-1} for the NH_2 -scissoring indicating intrinsic broadening of these lines related to the ion-helium coupling. The line intensities of the two stretch vibrations are well reproduced by the calculations which yield molecular absorption coefficients of 258 and $95\text{ km} \cdot \text{mol}^{-1}$ for the symmetric and antisymmetric NH_2 -stretch vibrations, respectively. The corresponding transition dipole moments are calculated to be parallel and perpendicular (along the Y axis in the molecular frame) to the permanent dipole moment.

Table 4-4. Vibrational wavenumbers ($\tilde{\nu}$ [cm^{-1}]) and molecular absorption coefficients (a [$\text{km} \cdot \text{mol}^{-1}$]) for both the symmetric and antisymmetric stretch of aniline cation.

	$\nu_{\text{sym}}\text{NH}_2$	$\nu_{\text{asym}}\text{NH}_2$
$\tilde{\nu}$ (cm^{-1})	3395.1	3488.8
a ($\text{km} \cdot \text{mol}^{-1}$)	258	95

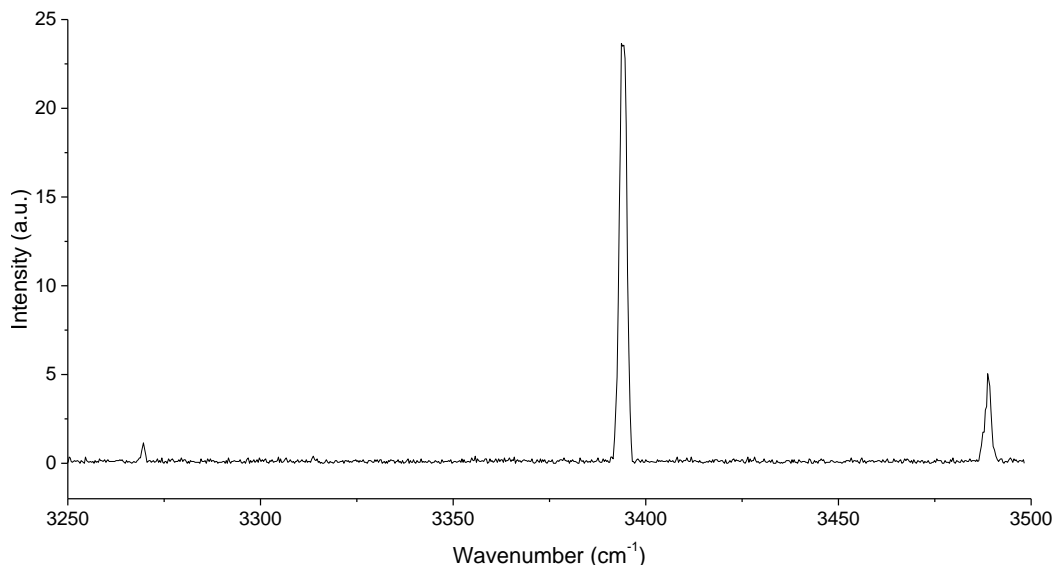


Figure 4-9. IR spectrum of aniline cation in helium droplets showing the scissoring overtone ($2\delta_{\text{scis}}\text{NH}_2$) at 3270.6 cm^{-1} , the symmetric NH_2 -stretch vibration ($\nu_{\text{sym}}\text{NH}_2$) at 3395.1 cm^{-1} and the antisymmetric NH_2 -stretch vibration ($\nu_{\text{asym}}\text{NH}_2$) at 3488.8 cm^{-1} . Data taken from [54].

4.3 EXPERIMENTAL APPROACH

4.3.1 Layout

The experiments are performed using the setup described in Chapter 2 using the reflectron TOF spectrometer. A beam of doped helium droplets is formed by introducing aniline into the doping chamber via a leak valve with a pressure on the order of 10^{-5} mbar. The temperature of the nozzle is set to ensure pick-up of one molecule per helium droplet.

The UV light for electronic excitation and ionisation is generated by frequency doubling the output of a dye laser pumped by the second harmonic of a Nd:YAG laser operating at a repetition rate of 20 Hz. The laser is focused on the droplet beam with a lens placed in the optical path 400 mm before the interaction region. Two focusing lenses of different focal length are employed depending on the experiment. A lens of 400 mm is used to perform the experiments of neutrals to tightly focus the beam. A 500 mm focusing lens is used to efficiently excite the ions. The droplets containing ions are repelled by the electrostatic interaction with the applied electric field. Therefore, increasing the beam size ensures excitation within the pump-probe delays. The initial horizontal polarisation is rotated using a half-wave plate when needed.

The IR is generated by an OPO/OPA laser pumped by a Nd-YAG operating at 10 Hz and focused by a BaF₂ focusing lens of 400 mm focal length. The estimated diameter ($1/e$) at the interaction region is 1.06 mm using the knife-edge method^[54, 117]. A half-wave plate is used to rotate its linear polarisation when needed.

All orientation experiments are performed in the reflectron stage of the machine. A static electric field is applied for most experiments. To explore the orientation of molecular ions after field-free ionisation, the electric field is applied after ionisation, just before the IR pulse. Further details about temporal delays and applied voltage values are given in section 4.4.2.3.

To minimise contributions of ions to the recorded signal other than aniline, the MCP detector is gated at the arrival time of the aniline ions. The use of different repetition rates of the lasers allows for background subtraction of signal induced by the UV light on a shot-by-shot basis.

4.3.2 Methods

To probe the orientation of neutral and ionic aniline by pendular state spectroscopy, different excitation and probe schemes are used. A brief description of the different cases is given below.

4.3.2.1 Neutral aniline

The orientation of neutral molecules is probed in two ways: by electronic and by IR vibrational spectroscopy. The $S_1 \leftarrow S_0$ electronic transition of aniline is measured by a single-colour experiment (Figure 4-10 left). UV light at 34100 cm⁻¹ generates ions by (1+1)-resonant-enhanced multiphoton ionisation (REMPI) via the band origin. The presence of a static electric field in the excitation region orients the permanent dipole moment of the neutrals before ionisation. The ionisation efficiency is proportional to the absorption cross-section of the $S_1 \leftarrow S_0$ electronic transition, which is greater when the laser polarisation is parallel to its dipole moment. The relative ion yield between laser polarisations can therefore be used to determine the molecular orientation.

The use of vibrational transitions to probe the orientation of neutral aniline involves pulsing linearly polarised IR light 20 ns before the molecules are ionised by the UV pulse (Figure 4-10 right). In this case, the IR is scanned in the energy range of the symmetric and antisymmetric NH₂-stretches (3422 cm⁻¹ and 3509 cm⁻¹ respectively^[14, 113]). Following excitation of the molecules, these relax to the ground

state on a sub-nanosecond timescale^[59, 118]. The energy deposited into the droplets by the relaxation of the excited molecule leads to the evaporation of approximately 700 helium atoms from the droplet^[14]. The formation of aniline ions upon UV ionisation is more likely for smaller droplets, and thus the ion yield will increase when the IR radiation is in resonance with a vibrational transition in the molecule. The intensity of the observed vibrational band is dependent on the IR polarisation direction with respect to the transition dipole moment and thus allows characterising the degree of orientation of the neutral aniline.

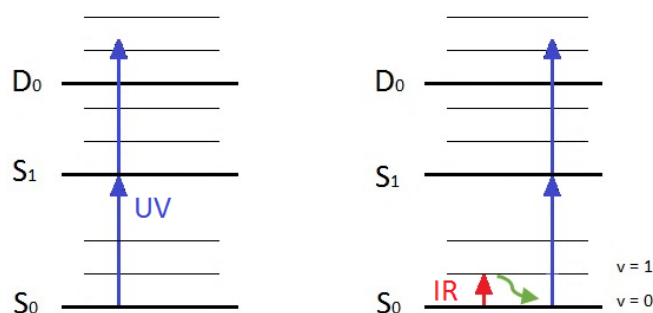


Figure 4-10. Conceptual scheme of the levels of the states populated: electronic (left) and vibrational (right) transitions of neutral molecules.

4.3.2.2 Ionic aniline

To determine the degree of orientation of aniline cations in helium droplets these have to be produced in situ. For this purpose, several ionisation schemes have been used, see Figure 4-11. In the first scheme, aniline is ionised non-resonantly via two photons by the fourth harmonic of a Nd:YAG laser at 37594 cm^{-1} . The other schemes employ a (1+1)-REMPI ionisation scheme, using either the band origin 0_0^0 at 34100 cm^{-1} or the 12_0^1 vibronic band at 34900 cm^{-1} as resonant state achieved by the frequency-doubled output of a dye laser pumped by the second harmonic of a Nd:YAG. The difference between these methods is twofold. First, the degree of orientation of the ions upon formation is expected to be different. Second, the initially populated vibrational states will be different. However, in all cases full relaxation and reorientation of the ions is expected on a sub-nanosecond timescale. The orientation of the ions is subsequently probed by IR spectroscopy. The IR light arrives tens of nanoseconds after ionisation, 20 ns for the resonant cases and 70 ns for the non-resonant case. These delays are long enough to ensure full relaxation of the ions but short enough ensuring that the ions are still present in the excitation region. The IR radiation excites either the symmetric NH_2 -stretch vibration at 3395

cm^{-1} or the antisymmetric stretch at 3488 cm^{-1} [14, 113]. Upon excitation the ions desolvate from the droplets by a non-thermal mechanism^[14], a detailed understanding of which is still lacking. By recording spectra using different IR polarisations, the orientation can be deduced provided that the desolvation mechanism is independent of the orientation of the excited ions.

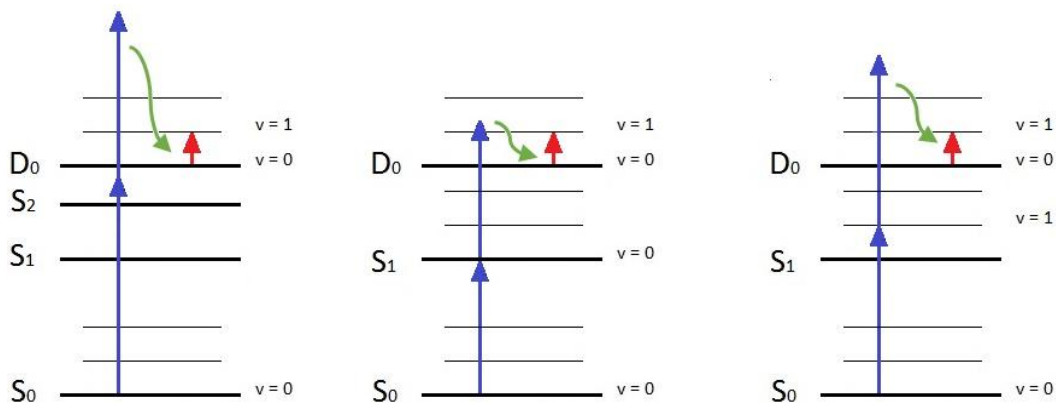


Figure 4-11. Scheme of ionisation methods and excitation: two-photon non-resonant ionisation (left), (1 + 1)-resonance-enhanced multiphoton ionisation via the band origin 0_0^0 (middle) and the 12_0^1 vibronic band (right) of the $S_1 \leftarrow S_0$ transition.

4.4 RESULTS

4.4.1 Neutral aniline

4.4.1.1 Electronic transitions

To validate the technique in our setup we start with the simplest system, i.e. the electronic excitation, and ionisation, of neutral aniline. The experimental method is detailed in 4.3.2.1. The molecular ion yield is recorded for ionisation of aniline via the band origin of the $S_1 \leftarrow S_0$ transition for parallel and perpendicular laser polarisations. The REMPI ionisation yield depends on the excitation efficiency of the intermediate electronic excited state. The signal levels therefore depend on the degree of orientation of the neutral molecules and the polarisation direction of the UV light. For small electric fields the neutral molecules are only weakly oriented and the resulting distribution will be nearly isotropic. As a result, the ion yield for the two different UV polarisations is nearly identical as it can be seen in Figure 4-12, which shows both signal levels recorded in a $5\text{ kV} \cdot \text{cm}^{-1}$ electric field using a laser fluence of $350\text{ mJ} \cdot \text{cm}^{-2}$. At high electric fields the ion yields indicate orientation of the molecules. In this case an increase (decrease) of the signal levels

is observed when the laser polarisation is perpendicular (parallel) to the electric field, because the electronic transition dipole moment is nearly perpendicular to the permanent dipole moment. This difference in ion yield for the two different laser polarisations is clearly noticeable in Figure 4-12 for the data recorded in an electric field of $60 \text{ kV} \cdot \text{cm}^{-1}$. Figure 4-13 shows the polarisation difference ratio determined by averaging over 3000 laser shots the ionic signal for various electric fields strengths in the range from 5 to $60 \text{ kV} \cdot \text{cm}^{-1}$. The data clearly reveal an almost linearly increasing polarisation difference factor with electric field and a low value even at the highest field applied, $60 \text{ kV} \cdot \text{cm}^{-1}$, suggesting that the molecules are not yet fully oriented with respect to the field.

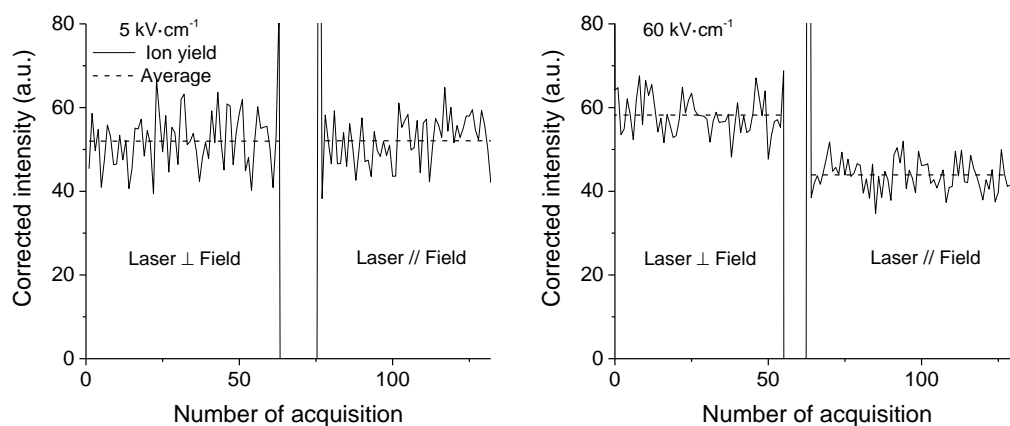


Figure 4-12. Dependence of the ion yield of aniline on the UV laser polarisation at different field strengths.

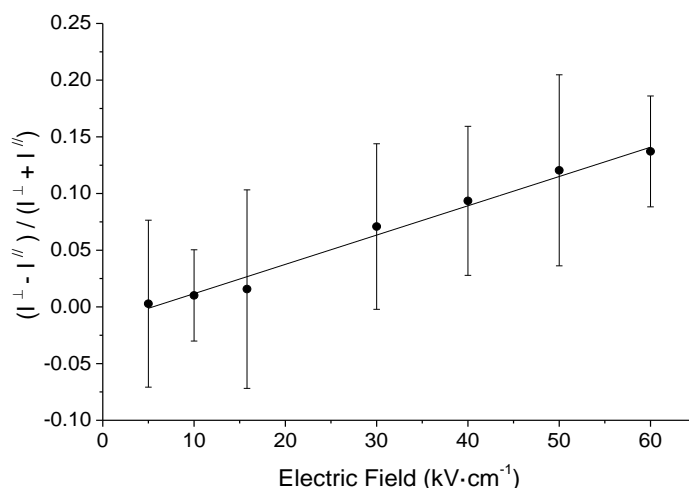


Figure 4-13. Effect of the applied electric field on the ion yield generated after electronic excitation of aniline (expressed as the difference ratios of the averaged intensity from each laser polarisation).

To obtain better insight into the degree of orientation that can be achieved, we have simulated the polarisation difference ratio as a function of the electric fields employing the method described in section 4.2.2 and using the constants for neutral aniline reported in Table 4-1 divided by a factor of three to consider the helium environment. A comparison between the experimental and calculated data, see Figure 4-14, indicates that the measured degree of polarisation is smaller suggesting that the technique fails to achieve the expected degree of orientation.

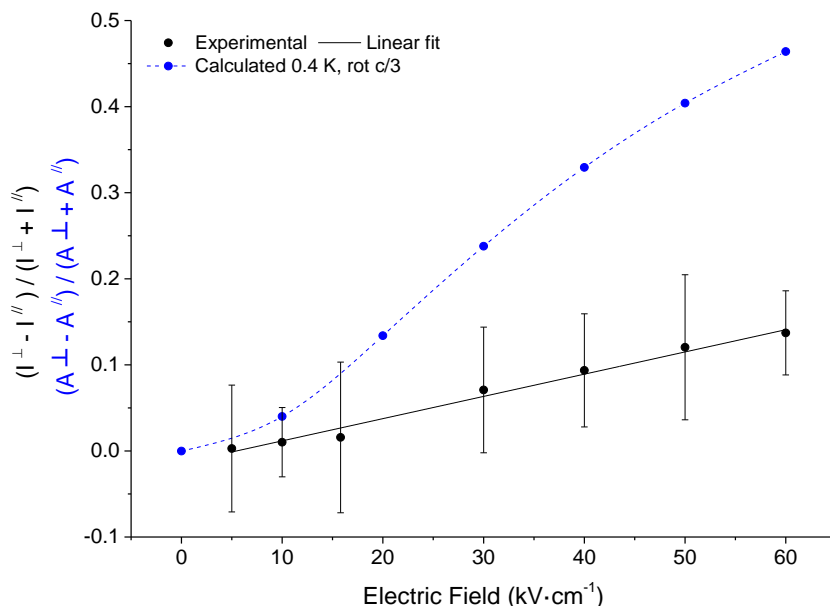


Figure 4-14. Effect of the applied electric field on the ion yield generated after electronic excitation of aniline (expressed as the ratio of the averaged intensity from each laser polarisation) and comparison with simulated values at standard helium nanodroplet conditions (expressed as the ratio of the transition peak areas from each laser polarisation).

4.4.1.2 Vibrational transitions

In view of the disagreement between the experimental and computed values of the polarisation difference ratio for the electronic transition, it was decided to measure the IR excitation of the NH_2 symmetric and antisymmetric stretching vibrations of neutral aniline to repeat the orientation measurement of neutral aniline. Pendular state IR spectra of neutral molecules have been found to be well-reproduced by model calculations analogous to those used here^[96, 110]. The IR measurements, obtained as described in 4.3.2.1, will therefore test the validity of our approach and setup.

Figure 4-15 left shows the spectrum of the antisymmetric NH_2 -stretch vibrational band recorded in an electric field of $15 \text{ kV} \cdot \text{cm}^{-1}$ under parallel and perpendicular laser polarisation as an example. The areas of the transitions have been obtained from a Gaussian function fitted to the data points. Although the signal is very weak and noisy, the polarisation difference ratio can be determined with sufficient accuracy by averaging over four sets of spectra to determine a clear trend with electric field. Only at $60 \text{ kV} \cdot \text{cm}^{-1}$, the signal levels of the antisymmetric stretch are not sufficient to determine the polarisation difference ratio.

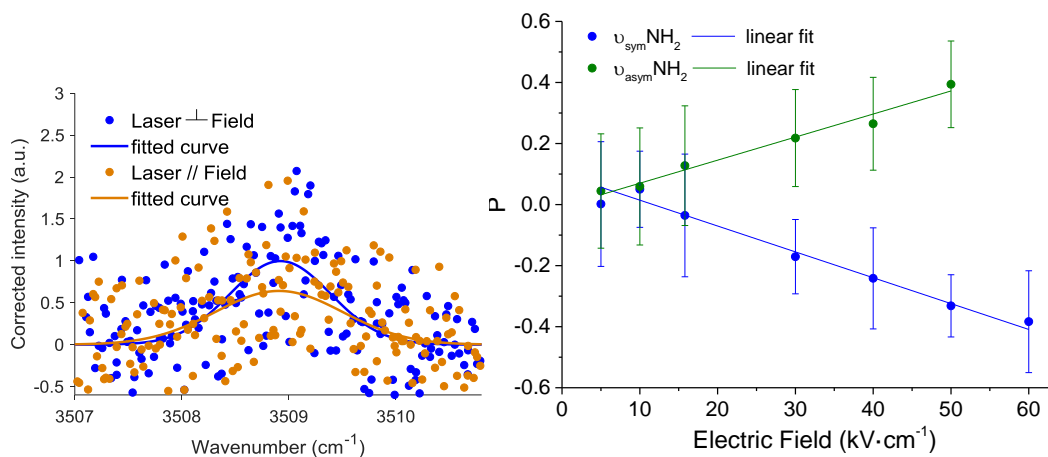


Figure 4-15. Left: Antisymmetric NH_2 -stretch vibrational band of aniline in helium nanodroplets when the laser polarisation direction is parallel and perpendicular in a $15 \text{ kV} \cdot \text{cm}^{-1}$ static electric field. Right: Effect of the applied electric field on the symmetric (in blue, $\nu_{\text{sym}}\text{NH}_2$ at 3422 cm^{-1}) and antisymmetric (in green, $\nu_{\text{asym}}\text{NH}_2$ at 3509 cm^{-1}) stretch transition intensity for neutral aniline (expressed as the difference ratios of the peak areas from each laser polarisation).

One can already obtain some important insight from the data alone. To start with, the slopes for the two vibrations are very similar but opposite. This is expected as the IR transition dipole moments are calculated to be perpendicular and parallel to the permanent dipole moment. Apart from that, the magnitudes of the polarisation difference ratios for the IR transitions are significantly larger than found for the electronic transition. Because the degree of orientation is the same in both experiments there has to be another reason for the observed difference in the polarisation difference ratios. We therefore have calculated the polarisation difference ratios in the same fashion as for the electronic transition but taking the properties of the two vibrational states. A comparison between the experimental and calculated values shows an almost perfect agreement, see Figure 4-16. This

allows us to have confidence in the methodology used and the degree of orientation obtained in the setup.

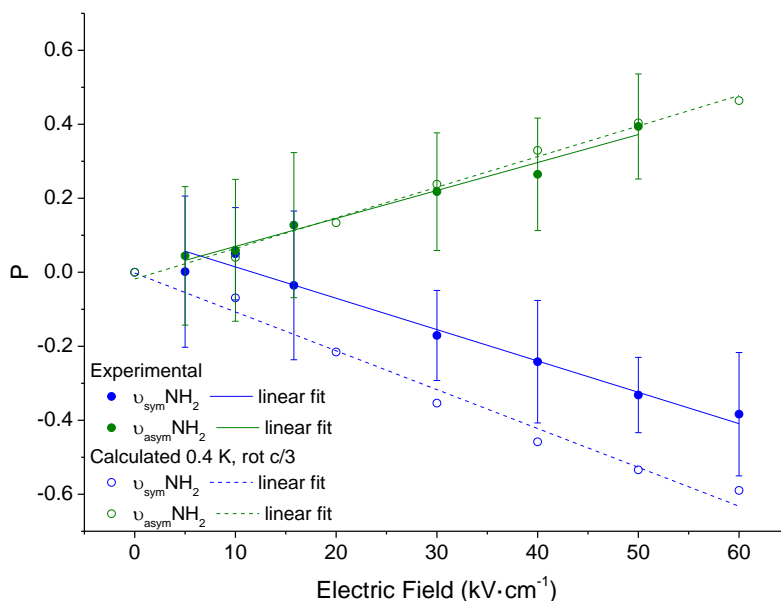


Figure 4-16. Effect of the applied electric field on the symmetric (solid line in blue, $\nu_{\text{sym}}\text{NH}_2$ at 3422 cm^{-1}) and antisymmetric (solid line in green, $\nu_{\text{asym}}\text{NH}_2$ at 3509 cm^{-1}) stretch transition intensity for neutral aniline and comparison with simulated values (dashed lines) at standard helium nanodroplet conditions both expressed as the difference ratios of the peak areas from each laser polarisation.

4.4.1.3 Summary

The degree of orientation achieved for neutral aniline in the setup validates the chosen technique. The magnitudes of the experimental polarisation difference ratios for the IR transitions are well-reproduced by calculations. However, one would think otherwise looking at the electronic polarisation results. The polarisation difference ratios suggest some degree of orientation but to a rather small extent, in disagreement with the calculations. Given that orientation of the neutral aniline in the field is actually achieved, several factors could lead to false values. As mentioned, the ion yield is proportional to the absorption cross-section of the electronic transition. Therefore, the saturation of this transition could explain the reduced polarisation difference ratios found. Another factor could be the way to probe orientation, the ion desolvation. In the IR experiment, the transition is excited prior to the ionisation process, which only is responsible of desolvation of the ion. In the electronic case, the laser acts both to probe the transition and

desolvate the dopant. This difference could affect somehow the degree of orientation.

4.4.2 Cationic aniline

Once the orientation of neutral aniline molecules embedded in helium droplets in an electric field is confirmed, we attempt to extend the technique to molecular ions. Based on the calculated properties of the aniline cation (in section 4.2.3.2) one can intuitively foresee the effect of the applied electric field on the IR spectra corresponding to the symmetric and antisymmetric NH_2 -stretch vibrations. To increase our understanding of the pendular state spectroscopy on ions in helium droplets the contribution of several experimental parameters: ionising laser energy, exciting laser power, lasers polarisations, helium droplets size, application of the orienting field before and after ionisation; is examined. Information is extracted from the bands shapes, bandwidths, polarisation difference ratios and by comparison to calculations.

The NH_2 -stretch vibrational bands are recorded at several static field strengths to confirm orientation of the molecular ions. Three different ionisation energies and schemes (see 4.3.2.2 for details) are examined. At first, IR spectra are investigated of aniline cations formed by non-resonant two-photon ionisation by 266 nm UV light with a fluence of $40 \text{ mJ} \cdot \text{cm}^{-2}$. Figure 4-17 left shows the spectrum of the NH_2 symmetric stretch vibration at 3395 cm^{-1} recorded in an applied electric field of $60 \text{ kV} \cdot \text{cm}^{-1}$ with parallel and perpendicular polarised IR light using a fluence of $75 \text{ mJ} \cdot \text{cm}^{-2}$. Even though the signal-to-noise ratio is poor, it nonetheless allows for the determination of the polarisation difference ratio. The peak areas are determined from a Gaussian function fitted to the data points. The polarisation difference ratios and their corresponding uncertainties shown in Figure 4-17 right have been obtained from typically seven spectral sets at a given electric field. The polarisation difference ratios decrease monotonously with increasing value of the static field, in agreement with the fact that the calculated IR transition dipole moment is perpendicular to the permanent dipole moment. This might indicate that after the time delay of 70 ns between the ionising UV laser and the IR probe laser the ions are still oriented. It is remarkable the extrapolation of the polarisation difference ratio to zero electric field, which does not yield the expected value of zero but rather -0.023 ± 0.007 .

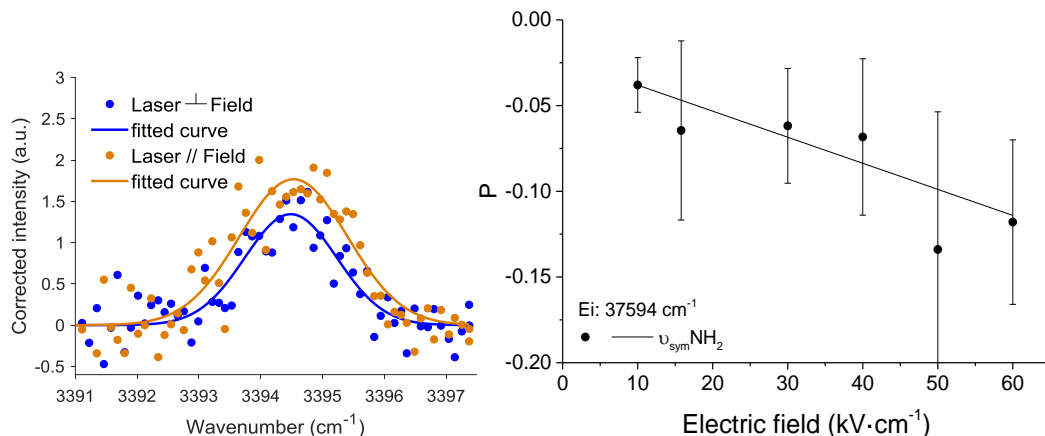


Figure 4-17. Left: Symmetric NH_2 -stretch vibrational band of non-resonantly generated aniline cations in helium nanodroplets when the laser polarisation direction is parallel and perpendicular in a $60 \text{ kV} \cdot \text{cm}^{-1}$ static electric field. Right: Effect of the IR polarisation on the symmetric stretch transition intensity for non-resonantly ionised aniline for different field strengths (expressed as the difference ratio of the peak areas from each laser polarisation).

Unfortunately, information about the antisymmetric stretch vibration could not be obtained for these experimental conditions. The molar absorption coefficient is about 2.7 times smaller than that of the symmetric stretch^[112], which makes the intensity of the transition to fall within the noise level.

In order to make a comparison between the two vibrational bands possible, aniline ions are produced using efficient (1+1)-REMPI schemes via the band origin and the 12_0^1 vibronic band of the $S_1 \leftarrow S_0$ transition. Using these ionisation schemes both the symmetric and antisymmetric stretch vibrational bands could be observed in fields up to $60 \text{ kV} \cdot \text{cm}^{-1}$. The NH_2 -scissoring overtone transition ($2\delta_{\text{scis}}\text{NH}_2$ at 3270.6 cm^{-1} ^[54], see Figure 4-9) could not be detected with sufficient signal to noise to extract any meaningful polarisation difference ratios.

Figure 4-18 shows IR spectra corresponding to excitation of the antisymmetric (left panel) and symmetric (right panel) stretch vibrations, recorded in an electric field of $60 \text{ kV} \cdot \text{cm}^{-1}$ 20 ns after ionisation of aniline in helium droplets via the band origin of the $S_1 \leftarrow S_0$ transition. To record these spectra, a UV fluence of $15 \text{ mJ} \cdot \text{cm}^{-2}$ is used whereas the IR fluence is similar to that used in the experiments using non-resonant ionisation, i.e. $75 \text{ mJ} \cdot \text{cm}^{-2}$. The figure shows that the signal yield of the antisymmetric stretch is larger when the IR polarisation is perpendicular, corresponding to a polarisation difference ratio of 0.14 ± 0.02 . In contrast, the

signal yield for the symmetric stretch is almost independent of the IR polarisation, corresponding to a value of 0.021 ± 0.011 for the polarisation difference ratio. This result is unexpected considering the calculated IR transition moments, which are perpendicular and parallel to the permanent dipole moment of the ion for the symmetric and antisymmetric stretch respectively. The polarisation difference ratios have been determined from five sets of spectra each and are shown in Figure 4-19. The polarisation difference ratios exhibit the expected dependence with electric field, i.e. (decreasing) increasing with electric field for the (anti)symmetric stretch. As anticipated, the slopes for both vibrations have opposite sign, $(-0.3 \pm 0.3) \cdot 10^3$ vs. $(1.5 \pm 0.2) \cdot 10^3$. Analogous to the results on non-resonant ionisation, extrapolation of the polarisation difference ratios to zero electric field yield very similar value different from zero. Whereas non-resonant ionisation yielded a value smaller than zero, resonant ionisation yields values larger than zero.

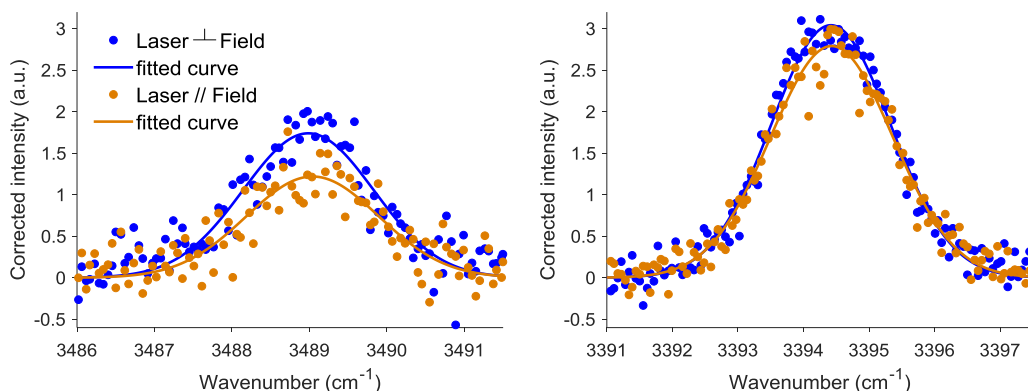


Figure 4-18. Antisymmetric (left) and symmetric (right) NH_2 -stretch vibrational bands of aniline cations generated by resonant ionisation via the $S_1 \leftarrow S_0$ band origin at 34100 cm^{-1} in helium nanodroplets when the laser polarisation direction is parallel and perpendicular in a $60 \text{ kV} \cdot \text{cm}^{-1}$ static electric field.

As might be expected, the results obtained for ions created by resonant ionisation via the 12_0^1 vibronic band of the $S_1 \leftarrow S_0$ transition are quite similar to those obtained for ionisation via the band origin. Nevertheless, there are some differences even though the spectra have been recorded under otherwise identical conditions. The slopes for both vibrations have similar magnitude in this case. The slope of the polarisation difference ratio with electric field for the symmetric stretch differs, $(-0.3 \pm 0.3) \cdot 10^3$ vs. $(-1.2 \pm 0.4) \cdot 10^3$, as well as its value at zero field, $(4.9 \pm 1.3) \cdot 10^2$ vs. $(5.5 \pm 1.3) \cdot 10^2$, for ionisation via the band origin 0_0^0 or the 12_0^1 vibronic band of the $S_1 \leftarrow S_0$ transition respectively. Within the stated uncertainty

of two standard deviations for the values, these differences appear significant. However, as one can see from the graphs in Figure 4-19, the uncertainties in the individual values of the polarisation difference ratios are relatively large for ionisation via the 12_0^1 band. Likewise, the values for ionisation via the band origin show a large spread around a straight line. It might therefore well be that the differences are not significant.

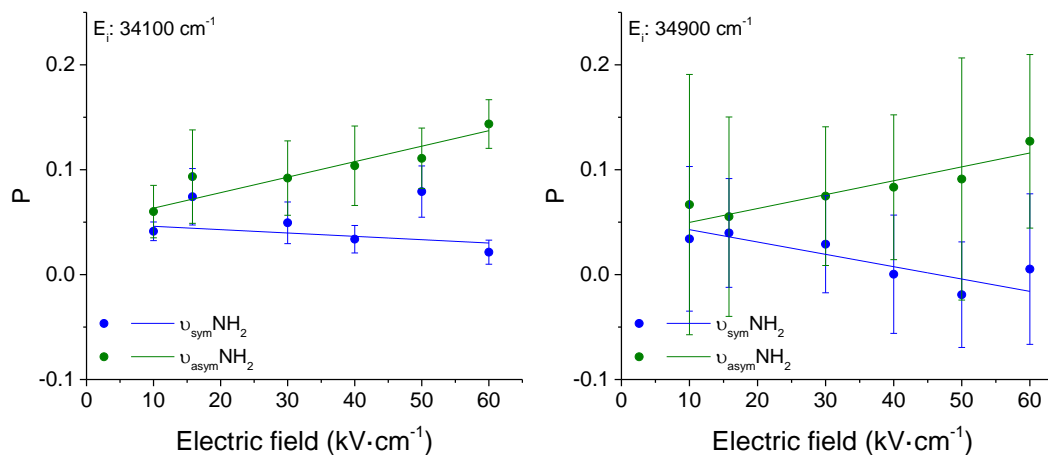


Figure 4-19. Effect of the IR polarisation on the symmetric ($\nu_{\text{sym}}\text{NH}_2$ at 3395 cm^{-1}) and antisymmetric ($\nu_{\text{asym}}\text{NH}_2$ at 3488 cm^{-1}) stretch transition intensity for cationic aniline (expressed as the difference ratios of the peak areas from each laser polarisation) as a function of the applied electric field. Left: resonant ionisation via the band origin 0_0^0 of the $S_1 \leftarrow S_0$ transition origin at 34100 cm^{-1} . Right: resonant ionisation via the 12_0^1 vibronic band at 34900 cm^{-1} of the $S_1 \leftarrow S_0$ transition.

To conclude this section, the results obtained under the different ionisation conditions are compared. The polarisation difference ratios are plotted in Figure 4-20. The fitted values are reported in Table 4-5 enabling a quantitative comparison of the polarisation difference ratios in terms of their variation with electric field and their values at zero field. Based on the variation of the polarisation difference ratios with electric field in opposite direction for the two NH_2 -stretch vibrations, it is safe to conclude that we observe orientation of ions in helium droplets. However, it is not obvious whether the reported values truly reflect the degree of orientation, like for IR spectroscopy on neutral aniline (4.4.1.2), or whether the values are somehow reduced, like in the case of electronic spectroscopy on neutral aniline (4.4.1.1). The variation of the electric field dependence of the polarisation difference ratio with ionisation method seems to indicate that the values do not reflect the true degree of orientation. Furthermore, the fact that the polarisation difference

ratio in the absence of a field deviates from zero, either positively or negatively depending on the ionisation method, might be an indication of a preferred orientation of the ions under free-field conditions. We will address these issues again after having presented other observations.

Table 4-5. Values and standard errors of slopes and intercepts and Pearson correlation coefficients obtained of the linear fits of the polarisation difference ratios obtained for different vibrational transitions of molecules ionised in the three different ways.

	E_i (cm ⁻¹)	Slope · 10 ³	Intercept · 10 ²	Pearson's r
$\nu_{\text{sym}}\text{NH}_2$	34100	-0.3 ± 0.3	4.9 ± 1.3	-0.43
	34900	-1.2 ± 0.4	5.5 ± 1.3	-0.85
	37594	-1.5 ± 0.3	-2.3 ± 0.7	-0.94
$\nu_{\text{asym}}\text{NH}_2$	34100	1.5 ± 0.2	4.9 ± 0.9	0.96
	34900	1.3 ± 0.3	3.7 ± 1.0	0.93
	37594	-	-	-

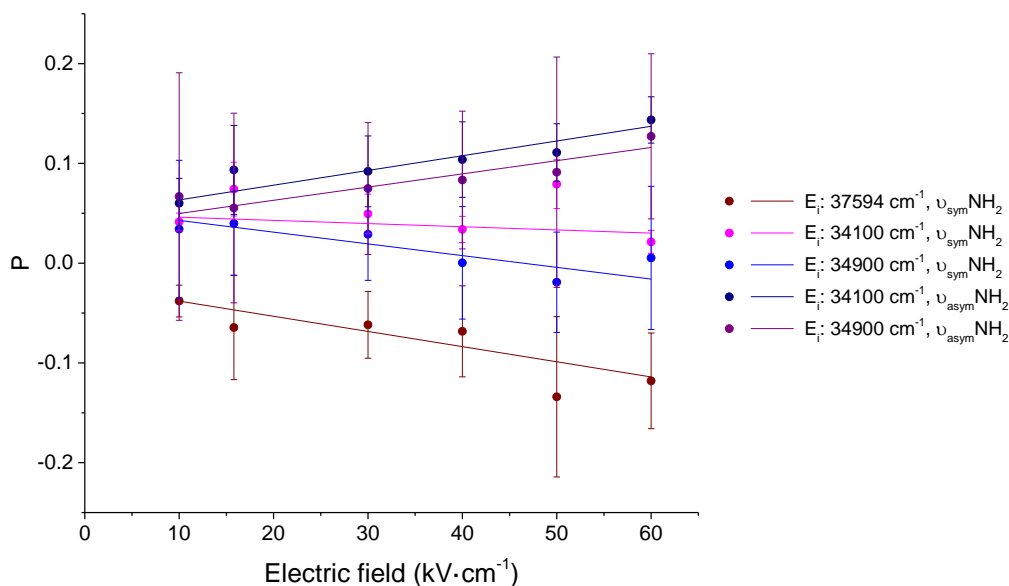


Figure 4-20. Effect of the IR polarisation on the symmetric ($\nu_{\text{sym}}\text{NH}_2$ at 3395 cm⁻¹) and antisymmetric ($\nu_{\text{asym}}\text{NH}_2$ at 3488 cm⁻¹) stretch transition intensity for cationic aniline ionised in three different ways (expressed as the difference ratios of the peak areas from each laser polarisation) as a function of the applied electric field. $E_i = 37594$ cm⁻¹ non-resonant ionisation, $E_i = 34100$ cm⁻¹ resonant ionisation via the $S_1 \leftarrow S_0$ band origin, $E_i = 34900$ cm⁻¹ resonant ionisation via the 12_0^1 vibronic band of the $S_1 \leftarrow S_0$ transition.

4.4.2.1 Calculations

The calculated polarisation difference ratios of neutral aniline and those determined experimentally from the IR spectra agree confirming the validity of the experimental approach used in this study. As discussed above, the experimental data for ionic aniline are not conclusive and thus, comparison with calculations would be helpful. The polarisation difference ratios for the symmetric and antisymmetric stretch vibrations have been calculated using the molecular constants reported in Table 4-3. For these calculations the calculated gas phase rotational constants have been reduced by a factor of nine to take into account the helium environment^[14]. A comparison of the experimental with the calculated polarisation difference ratios shows a large discrepancy, the calculated values are significantly larger (Figure 4-21 left). To determine whether this difference is related to the effective rotational constants, the calculations have been repeated using different reduction factors for the gas phase constants. The calculated polarisation difference ratios are of course different for all reduction factors used, but in all cases still significantly larger than found experimentally. It should be noted that the calculated values are also larger than for neutral aniline. This is not surprising given the magnitude of the permanent dipole moment, 2.77 D, compared to that of neutral aniline, 1.607 D.

It is assumed in the calculations that the rotational degrees of freedom of the aniline cation have equilibrated to the droplet temperature of 0.37 K. In the ionisation process, however, a significant fraction of the ions is formed in vibrationally excited states. Relaxation of these ions deposit a significant amount of energy into the droplets. The heated droplets will cool down to sub-kelvin temperatures on a sub-nanosecond timescale. Since the degree of orientation that can be achieved depends strongly on the rotational temperature of the molecules, the polarisation difference ratios have been calculated for a range of temperatures. Notwithstanding the temperature dependence of the polarisation difference ratio, see Figure 4-21 right, the calculations do not reproduce the experimental data using temperatures close to the droplet equilibrium temperature. Only when assuming a temperature around 4 K a reasonable agreement is observed. However, such a high temperature is unrealistic for a helium droplet 20 ns after ionisation. If the system probed were not an ion containing helium droplet, but rather an ion partially solvated by helium atoms, a rotational temperature of a few kelvin could be feasible in view of the estimated helium binding energy of 5 cm⁻¹ ^[69].

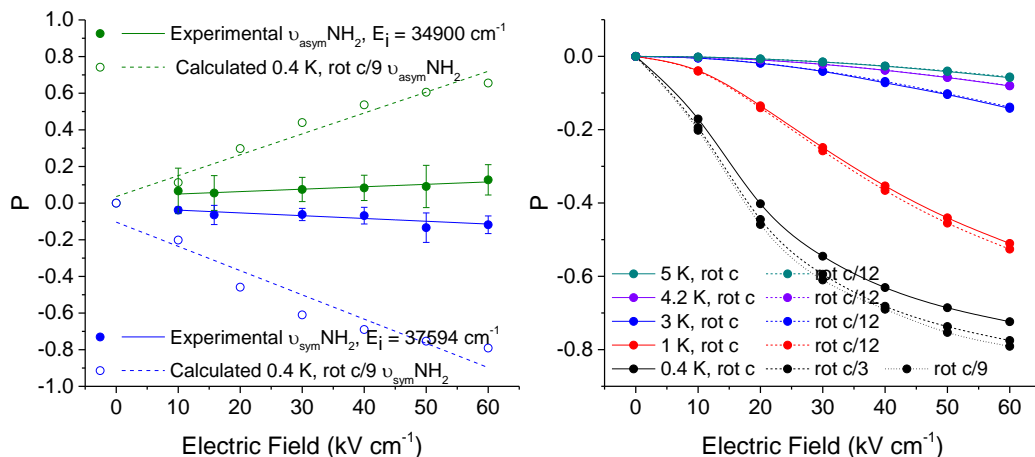


Figure 4-21. Left: Effect of the applied electric field on the symmetric (in blue) and antisymmetric (in green) stretch vibrational transition intensity (expressed as the difference ratios of the peak areas from each laser polarisation) and comparison with simulated values at standard helium nanodroplet conditions for ions (dashed lines). Right: Simulated effect of the electric field on the symmetric stretch transition area of aniline ions resulting for different temperatures and rotational constants.

4.4.2.2 Effect of UV polarisation

The disagreement between theory and experiment discussed above warrants a more detailed investigation of possible effects influencing the apparent orientation of the cations. As shown in 4.4.1.1, the ion yield following (1+1)-REMPI is affected by the polarisation of the UV light. Furthermore, it was found that the polarisation difference ratio deviates from zero in the absence of an electric field. To determine whether the ionisation process possibly leaves ions in a preferred orientation, the IR spectra of the symmetric and asymmetric NH₂ stretching vibrations are recorded using different polarisations of the UV light. The polarisations defined relative to the applied field are: perpendicular, parallel, at 54.7° angle (the magic angle), and perpendicular to the magic angle. The embedded aniline molecules are ionised via the band origin of the S₁ ← S₀ transition at 34100 cm⁻¹ using a fluence comparable to that used to record the IR spectra reported in section 4.2.2, i.e. 15 mJ · cm⁻². For each UV polarisation, the polarisation difference ratio is determined from four sets of IR measurements. The resulting values are plotted in Figure 4-22. The similarity of the data for the different UV polarisations is evident allowing to rule out any remaining orientation of the ions due to the ionisation process.

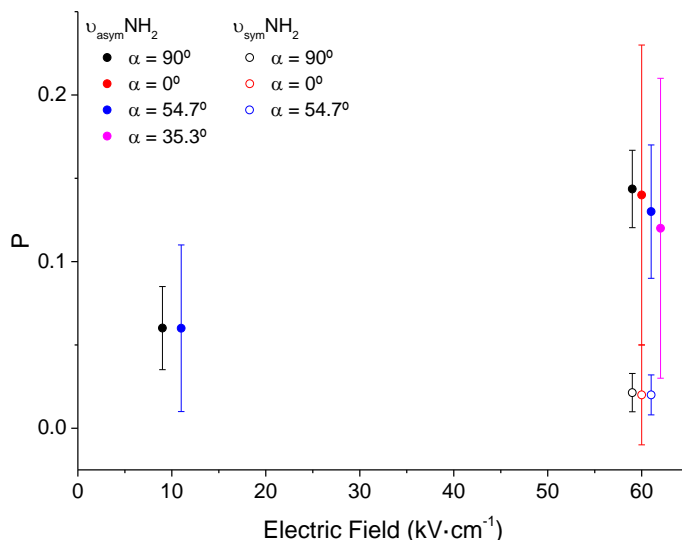


Figure 4-22. Effect of the IR polarisation on the symmetric (open circle, $\nu_{\text{sym}}\text{-NH}_2$ at 3395 cm^{-1}) and antisymmetric (solid circle, $\nu_{\text{asym}}\text{-NH}_2$ at 3488 cm^{-1}) stretch transition intensity for cationic aniline for several UV polarisations (expressed as the difference ratios of the peak areas from each laser polarisation). α is the angle between the UV laser polarisation direction and the field direction. The values are taken in a $10\text{ kV} \cdot \text{cm}^{-1}$ and $60\text{ kV} \cdot \text{cm}^{-1}$ electric field. Data points at the same field strength are horizontally displaced from each other for clarity.

4.4.2.3 Effect of pulsed electric fields

The experiments described above indicate that the initial orientation of the ions is not relevant for the final degree of orientation as probed by IR spectroscopy. Additional insight into the orientation process might be obtained by switching the electric field. To this end, aniline is ionised under (nearly) field-free conditions after which the orienting field is rapidly switched on using a fast high-voltage switch having a risetime of 100 ns. Figure 4-23 shows the various delays (pump-switch, pump-probe, and switch-probe) and voltage configurations examined.

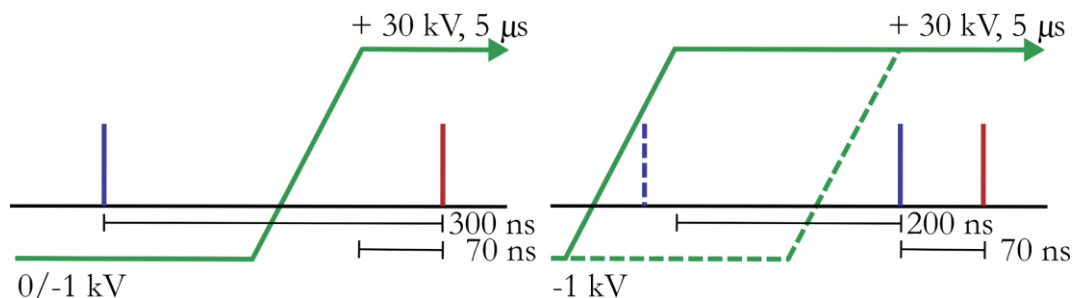


Figure 4-23. Scheme showing the relative delays of pump, probe and high-voltage switch. Left: normal switch working conditions with an initial zero or negative voltage. Right: voltage switches 200 ns before the UV pulse to imitate static field conditions.

The studies using static electric field revealed some differences between different ionisation schemes. Therefore, the effect of pulsed electric fields is investigated both for non-resonant and resonant ionisation of the aniline. Using the non-resonant ionisation scheme, the two voltage configurations indicated in Figure 4-23 left are employed. At a pump-probe delay of 300 ns, the orienting field of $60 \text{ kV} \cdot \text{cm}^{-1}$ is applied 70 ns before the IR pulse by switching the applied voltage from either 0 or -1 kV to +30 kV. The use of a negative initial voltage has the advantage that aniline cations produced by the UV ionisation process are removed prior to the IR pulse, thereby enhancing the sensitivity.

The spectrum on Figure 4-24 left, corresponding to the symmetric stretch band, has been recorded in the absence of an electric field during the ionisation process. The polarisation difference ratio of -0.19 ± 0.02 deduced from these spectra, is similar to that obtained under static field conditions $60 \text{ kV} \cdot \text{cm}^{-1}$ (Figure 4-17 left). It is worth noting that in both cases the orienting field has approximately the same time duration, i.e. 70 ns. This strongly suggests that the orientation of the neutral molecules does not affect the outcome. When using an initial negative voltage, however, one obtains a very different result. In this case, the spectra recorded with different IR polarisations are very similar, see Figure 4-24 right, and a polarisation difference ratio closer to zero, -0.035 ± 0.014 , is obtained. It appears that the relatively weak electric field prevents orientation of the aniline cation on the timescale of 70 ns. This conclusion contradicts the other results. Unfortunately, it was not possible to confirm this conclusion by determining the polarisation difference ratio of the antisymmetric stretch transition. The signal-to-noise ratio was too low to extract a meaningful polarisation difference ratio. In this context it should be mentioned that the presence of a negative voltage during a relatively long time, $\sim 130 \text{ ns}$, not only removes aniline ions resulting from the ionisation, but

also the lightest doped droplets, leaving behind only the heavier, larger droplets. Potentially, the orientation involving heavier droplets is not as efficient.

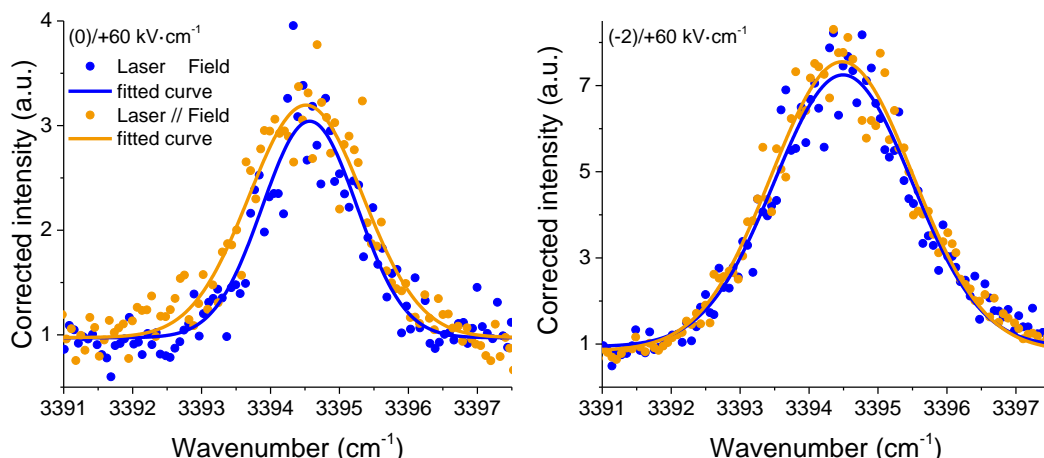


Figure 4-24. Left: Effect of a $60 \text{ kV} \cdot \text{cm}^{-1}$ pulsed electric field on the symmetric stretch vibrational transition of ionic aniline after non-resonant ionisation. Right: Effect of a $60 \text{ kV} \cdot \text{cm}^{-1}$ pulsed electric field with $-2 \text{ kV} \cdot \text{cm}^{-1}$ initial field.

Resonant ionisation yields higher signal levels than in the non-resonant case. As a result, both the symmetric and antisymmetric stretch vibrations could be investigated for the pulsing scheme used for non-resonant ionisation, Figure 4-23 left. As an extra check, the polarisation difference ratio has been determined using both UV polarisations for the symmetric stretch vibration. In addition, the symmetric stretch vibration is examined using yet another configuration, shown in Figure 4-23 right, where the orienting voltage is applied 200 ns before the UV pulse as to simulate the static field conditions. In this case the pump-probe delay is set to 70 ns. The polarisation difference ratios found for these measurements are plotted together with the static field measurements (4.4.2) in Figure 4-25 for comparison. The figure reveals that there are noticeable differences. The polarisation difference ratio is largest for ionisation in the absence of an electric field and smallest when the strong orienting field is present. Having a weak field present during ionisation yields values in between the two extreme cases. These results are found not to depend on the polarisation of the UV light. In addition to that, the polarisation difference ratio found for the configuration that is supposed to mimic the static situation, Figure 4-23 right, is comparable to the static case. What is most striking about these results is that for the symmetric stretch band a positive polarisation difference ratio is found, where one would expect a negative

value since in this case the vibrational transition moment is parallel to the permanent dipole moment.

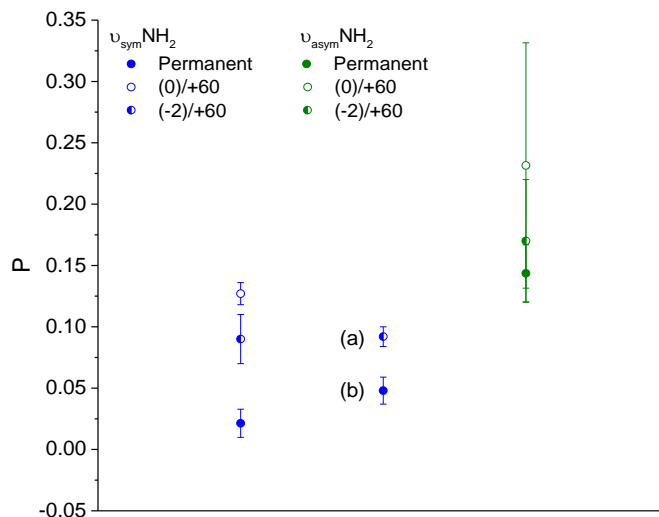


Figure 4-25. Effect of a $60 \text{ kV} \cdot \text{cm}^{-1}$ pulsed electric field on the difference ratios of the peak areas from each IR laser polarisation on the symmetric ($\nu_{\text{sym}} \text{NH}_2$ at 3395 cm^{-1}) and antisymmetric ($\nu_{\text{asym}} \text{NH}_2$ at 3488 cm^{-1}) stretch vibrations of aniline cations generated by resonant ionisation via the $S_1 \leftarrow S_0$ band origin at 34100 cm^{-1} . (a) The positive voltage is applied before the UV pulse, as if no switch. (b) The polarisation of the UV light is vertical (rest done for horizontal). The strength of the field is $60 \text{ kV} \cdot \text{cm}^{-1}$ for all measurements; separated for readability.

A proper analysis of switching electric fields on the observed polarisation difference ratios requires a systematic variation of the electric fields, instead of a measurement at a single voltage setting. Unfortunately, a breakdown of the switching circuitry prevented these measurements to be performed within the time frame of this thesis.

4.4.2.4 Droplet size dependence

All the data reported above have been obtained using a helium nozzle temperature of 17 K , corresponding to undoped droplets containing on average 3540 helium atoms. The cation-helium interaction is short range. Consequently, analysis for droplet sizes ranging from approximately 2000 to 11000 of helium atoms would not be useful to tell if this interaction affects the degree of orientation. However, the desolvation efficiency of excited ions from helium droplets has been found to be droplet size dependent^[54]. To investigate whether the ion desolvation could affect the polarisation difference ratio and thus the apparent orientation, measurements for several droplet sizes are performed. In these experiments the standard

conditions are used, i.e. ionisation via the band origin of the $S_1 \leftarrow S_0$ transition at 34100 cm^{-1} , a pump-probe delay of 20 ns and a static orienting field.

Figure 4-26 shows the polarisation difference ratio for the antisymmetric stretch band at an orienting field strength of $60\text{ kV} \cdot \text{cm}^{-1}$ as a function of the mean droplet size. These factors have been obtained by recording four data sets per point. Even though there is considerable spread in the reported values, no systematic variation with droplet size is observed over the size range studied within the uncertainties. These results indicate that if the desolvation process were to affect the polarisation difference ratio, it does so in the same way for all droplet sizes.

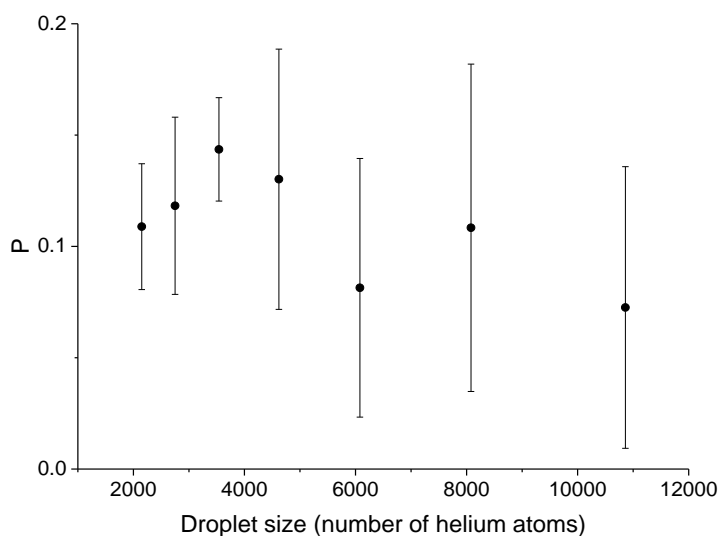


Figure 4-26. Effect of the droplet size on the antisymmetric ($\nu_{\text{asym}}\text{NH}_2$ at 3488 cm^{-1}) stretch transition intensity for ionic aniline (expressed as the difference ratios of the peak areas from perpendicular IR laser polarisations) in a $60\text{ kV} \cdot \text{cm}^{-1}$ field.

4.4.2.5 IR fluence dependence

Pendular state spectroscopy is rather sensitive to saturation effects; high laser fluences tend to reduce the polarisation difference ratios. To determine whether the transitions are saturated by the IR radiation, the polarisation difference ratios of the symmetric vibration have been determined at a static field of $60\text{ kV} \cdot \text{cm}^{-1}$ using pulse energies ranging from 40 to 650 μJ , corresponding to fluence ranging from 5 to 75 $\text{mJ} \cdot \text{cm}^{-2}$. Again, the standard experimental conditions are used, i.e. resonant ionisation via the band origin at 34100 cm^{-1} and pump-probe delay of 20 ns. The results are reported in Figure 4-27 and show no systematic variation with laser fluence.

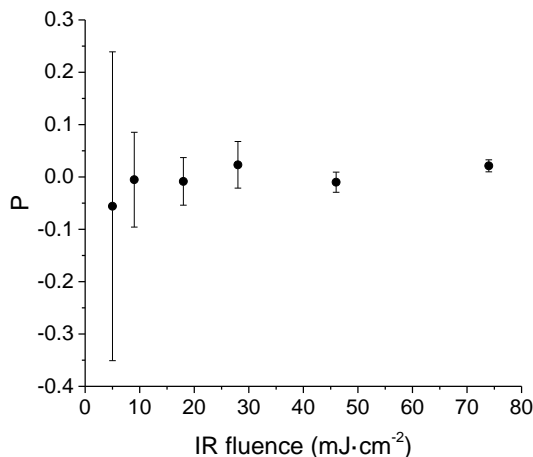


Figure 4-27. Effect of the IR laser fluence on the symmetric stretch ($\nu_{\text{sym}}\text{NH}_2$ at 3395 cm^{-1}) for aniline cation (expressed as the difference ratios of the peak areas from each laser polarisation) in a $60\text{ kV} \cdot \text{cm}^{-1}$ field.

Additionally, measurements of the symmetric stretch are performed for a laser power three times lower, to compensate for the difference in the molar absorption coefficients, for increasing electric fields. The polarisation difference ratios, Figure 4-28 in black, give a slope of $(-1.2 \pm 0.4) \cdot 10^{-3}$ not so far from the obtained for the other ionisation schemes (non-resonant and resonant via the 12_0^1 band) confirming that the differences are not significant.

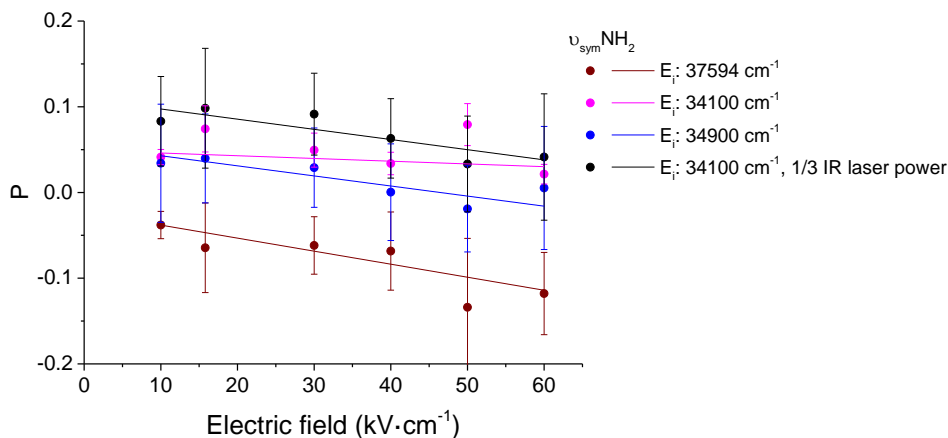


Figure 4-28. Effect of the IR polarisation on the symmetric ($\nu_{\text{sym}}\text{NH}_2$ at 3395 cm^{-1}) stretch transition intensity for cationic aniline as a function of the applied electric field when the IR laser power is decreased by a factor of three after resonant ionisation via the $S_1 \leftarrow S_0$ band origin at 34100 cm^{-1} and comparison with full laser power for all ionisation schemes expressed as polarisation difference ratios.

An estimate of the fluence required to saturate an optical transition can be made based on the calculated absorption intensities. The fluence [$\text{J} \cdot \text{cm}^{-2}$] needed to saturate the transition under pulsed excitation follows the expression^[119]:

$$F \gtrsim \frac{hc}{2\sigma\lambda} \quad (4.3)$$

where h is Planck's constant [$\text{J} \cdot \text{s}$], c is the speed of light [$\text{m} \cdot \text{s}^{-1}$], σ is the cross-section [cm^2], and λ is the wavelength [nm].

The cross-section is particular for every molecule and transition. It is expressed as^[120]:

$$\sigma = \frac{\ln 10 a}{N_a \Delta\nu_{1/2}} \quad (4.4)$$

where a is the integrated molar absorption coefficient [$\text{km} \cdot \text{mol}^{-1}$], N_a is Avogadro's number [mol^{-1}] and $\Delta\nu_{1/2}$ is the full width at half maximum of the transition [cm^{-1}].

The calculated values needed to meet the condition, together with the molar absorption coefficients of these transitions^[112], and calculated absorption cross-sections are gathered in Table 4-6. In order to account for all field strengths, a full width at half maximum of $2.2 \pm 0.2 \text{ cm}^{-1}$ is considered (see 4.4.2.6). The results of the vibrations of neutral aniline are included for comparison.

Table 4-6. Integrated molar absorption coefficients (a) for aniline and its radical cation for both the symmetric and antisymmetric stretch [$\text{km} \cdot \text{mol}^{-1}$]. Calculated values of absorption cross-sections (σ [cm^2]). The error comprises the different values of $\Delta\nu_{1/2}$ (FWHM) at different field strengths ranging from 2.0 to 2.4 cm^{-1} [cm^2]. Energy densities needed to meet the saturation condition [$\text{mJ} \cdot \text{cm}^{-2}$].

	$\nu_{\text{sym}}\text{NH}_2$		$\nu_{\text{asym}}\text{NH}_2$	
	Neutral	Cationic	Neutral	Cationic
a ($\text{km} \cdot \text{mol}^{-1}$)	20	258	17	95
σ (cm^2)	$(3.5 \pm 0.3) \cdot 10^{-18}$	$(4.5 \pm 0.4) \cdot 10^{-17}$	$(3.0 \pm 0.3) \cdot 10^{-18}$	$(1.67 \pm 0.16) \cdot 10^{-17}$
Sat condition				
($\text{mJ} \cdot \text{cm}^{-2}$)	9.8 ± 0.8	0.76 ± 0.06	11.73 ± 1.17	2.10 ± 0.19

To determine if the laser fluence used in the experiments could lead to saturation, one needs to know the focal spot area. To calculate it, the beam diameter is measured with the knife-edge method. A value of $1/e$ equal to (1.06 ± 0.20) mm is measured at the distance where the IR laser intersects the molecular beam. No difference between the two laser polarisations is observed within the reported uncertainty, nor is any displacement of the laser beam observed with changing polarisation. This is of great importance since a slight change in the laser alignment caused by rotation of the half-wave plate could make the results inconsistent. A pulse energy of $650 \mu\text{J}$, yielding a fluence of $(74 \pm 3) \text{ mJ} \cdot \text{cm}^{-2}$, is used under normal experimental conditions. This value exceeds the saturation condition by a factor of ten for neutral aniline and a factor of hundred for its ionic counterpart. Even though the fluence of the IR radiation used for the experiments on neutral aniline exceeds the estimated saturation threshold by an order of magnitude, the polarisation difference ratios determined from the spectra are in agreement with the calculations. This suggests either that saturation does not have an important effect on the derived polarisation difference ratios, or that the saturation fluence has been underestimated. In the case of the aniline cation, the polarisation difference ratios derived from the spectra are found to be independent of laser fluence over a range of one order of magnitude. At the lowest fluence used, the estimated degree of saturation is similar to that for neutral aniline. Based on the fact that under these conditions the correct polarisation difference ratios are obtained for neutral aniline, we conclude that saturation does not affect the polarisation difference ratios for the aniline cation.

4.4.2.6 Lineshape measurements

Even though the polarisation difference ratios are found to vary with electric field indicating orientation of the ions, no obvious change in the width and shape of the vibrational bands is observed with changing electric field, see Figure 4-17 left and Figure 4-18. Even though the bandwidth of the IR probe laser is relatively large, 0.8 cm^{-1} , one would expect to observe some field dependence. To determine whether an electric field dependence exists, the widths of all the transitions recorded have been analysed from Gaussian distributions fitted to the data points. The weighted averaged widths (FWHM) are plotted in Figure 4-29 as a function of electric fields for the different ionisation energies used. No clear systematic electric field dependence of the width can be discerned from these plots. Similar width values when the laser fluence is decreased let us conclude that these results are independent of the IR intensity.

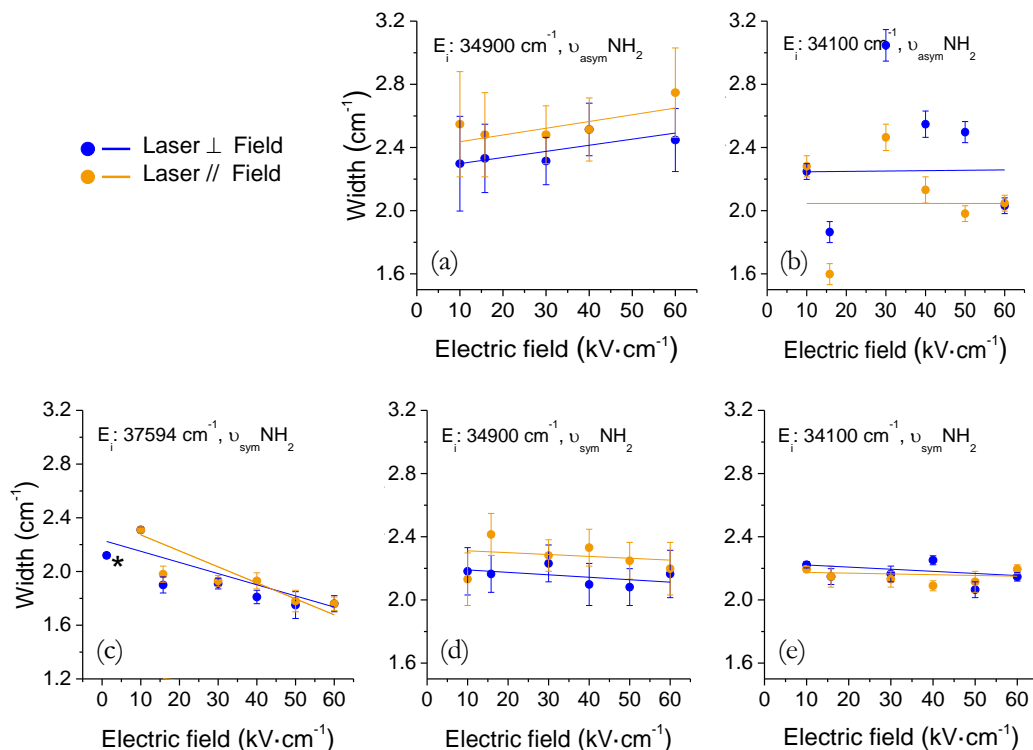


Figure 4-29. Widths of the antisymmetric (a, b) and symmetric (c, d, e) vibrational stretch of the amino group with increasing electric field obtained after non-resonant ($E_i = 37594$ cm⁻¹; c), resonant via the 12_0^1 vibronic band of the $S_1 \leftarrow S_0$ transition ($E_i = 34900$ cm⁻¹; a, d) and resonant via the $S_1 \leftarrow S_0$ band origin ($E_i = 34100$ cm⁻¹; b, e) ionisation of aniline. *) Value obtained previously in the group^[14].

To determine the expected changes in width as function of electric field and laser polarisation, pendular state spectra have been simulated. The transitions are calculated using a factor of nine reduction of the gas-phase rotational constants and a temperature of 0.4 K. The resulting stick spectrum for the aniline cation symmetric stretch vibration can be found in Figure 4-30 (a) for field-free conditions and (b) for an electric field of 60 kV · cm⁻¹. To take into account the laser bandwidth, the transitions are convoluted with a Gaussian distribution having a FWHM of 0.8 cm⁻¹ to yield the spectra reported in Figure 4-30 (c) and (d). The figures show how the typical pendular shape is obscured and could explain the experimental spectra. However, the widths report lower values than the experimental ones. It is worth mentioning that in a previous study^[54] the width of the stretch transitions has been found to be significantly larger than that of the scissoring overtone's transition (Figure 4-9). While the shape of this overtone transition could be reproduced by the rotational band contour, the large widths of

the stretch vibrations could not be explained. It could well be that the large width of these bands is associated with a process that also affects the formation of pendular states.

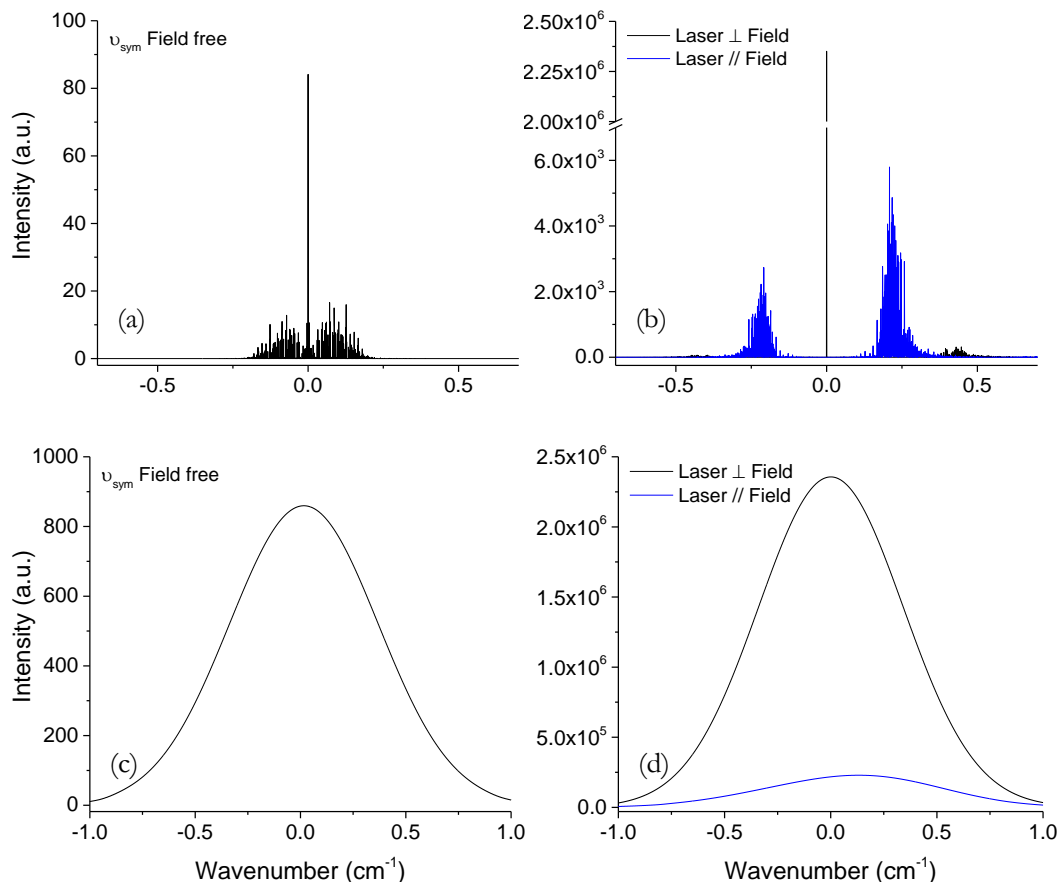


Figure 4-30. Simulated spectra of the symmetric stretch ($\nu_{\text{sym}}\text{NH}_2$ at 3395 cm^{-1}) of cationic aniline under field free (left) and for parallel (blue) and perpendicular (black) laser polarisations to the electric field at $60\text{ kV} \cdot \text{cm}^{-1}$ (right). The bottom figures, (c) and (d), are obtained when the transitions are convoluted with a Gaussian distribution having a FWHM of the laser bandwidth.

4.4.2.7 Summary

Orientation of cationic aniline in helium droplets in the presence of electric fields has been observed. The disagreement between the experimental and calculated data indicates however that the reported values do not present the expected degree of orientation. As in the case of electronic spectroscopy on neutral aniline, it could be that the values do not correspond to the truly achieved degree of orientation or it could mean that there is another process affecting orientation. For that reason, a

more detailed investigation of possible effects influencing the apparent orientation of the cations was performed.

The effect of the UV light polarisation was first examined and enabled us to discard a preferred orientation caused by the ionisation process. Applying a pulsed electric field to ionise aniline under (nearly) field-free conditions has led to inconclusive results. To obtain more information and complete this study, one could examine the evolution of the orientation in the presence of increasing fields which unfortunately could not be performed within the timeframe of this work.

Since the efficiency of the non-thermal desolvation mechanism occurring upon excitation depends on the droplet size, the effect of the droplet size was next considered. Even though the results did not reveal any dependence, we cannot confirm whether or not this mechanism affects the orientation. If it does, it would do so in the same way for all droplet sizes.

Even though the fluence of the IR radiation used in the experiments of neutral aniline exceeds the estimated saturation threshold, the agreement of the experimental and calculated polarisation difference ratios proved it to not affect them. Since the saturation is an order of magnitude greater for ionic aniline, the dependence of the polarisation difference ratios on the IR power has been studied at high fields. The results have shown a lack of dependence even at conditions for which the saturation would be as important as for the neutral. We could then conclude that saturation does not affect the polarisation ratios for the aniline cation.

The width and shape of the vibrational bands have shown no change with electric field and polarisation. Calculations performed taking into account the laser bandwidth point out that the distortion of the shape as the Stark effect mixes the rotational levels is concealed. However, the width of the experimentally observed bands is broader than those calculated and independent of the laser fluence. This could be caused by a process that could also affect the formation of pendular states.

A significant part of this work was to explore the above mentioned effects and dependencies to acquire a more profound understanding of the process and determine whether other experimental conditions would lead to greater polarisation difference ratios in agreement with the calculations. Most effects were ruled out and the reason behind the degree of orientation measured remains unknown. To

complete these studies, the effect of the pulsed electric field strength could be measured in a methodical way. It would also be interesting to look into other systems for which the linewidths are not intrinsically broadened. Apart from that, one could consider performing another experiment to probe the measured orientation. By Coulomb exploding the ion in the cryogenic matrix, one could examine by VMI if the product orientation corresponds to the measured degree of orientation or indicates a higher degree.

4.5 SUMMARY

In this chapter, orientation of molecular ions in helium nanodroplets using an electric field was examined. Pendular state spectroscopy has previously confirmed orientation of neutral polar molecules in helium nanodroplets. Therefore, orientation of a neutral molecule was first examined to validate the technique and aid understanding our results. Aniline and aniline cation were chosen due to their simple structures that make them ideal candidates to be used in a proof-of-principle experiment.

The aniline ion yield found for ionisation via the band origin of the $S_1 \leftarrow S_0$ transition for parallel and perpendicular laser polarisations revealed some degree of orientation. Disagreement between the experimental and computed values suggested that the molecules were not as oriented as would be expected. For this reason, the IR excitation of the NH_2 stretching vibrations was measured to repeat the orientation measurement of neutral aniline. The results in this case were found to be well-reproduced by the calculations indicating that orientation of the neutral aniline was as expected and the previous results did not show the true degree of orientation, see Figure 4-31. This confirmed that orientation of neutral aniline molecules in helium nanodroplets could be achieved.

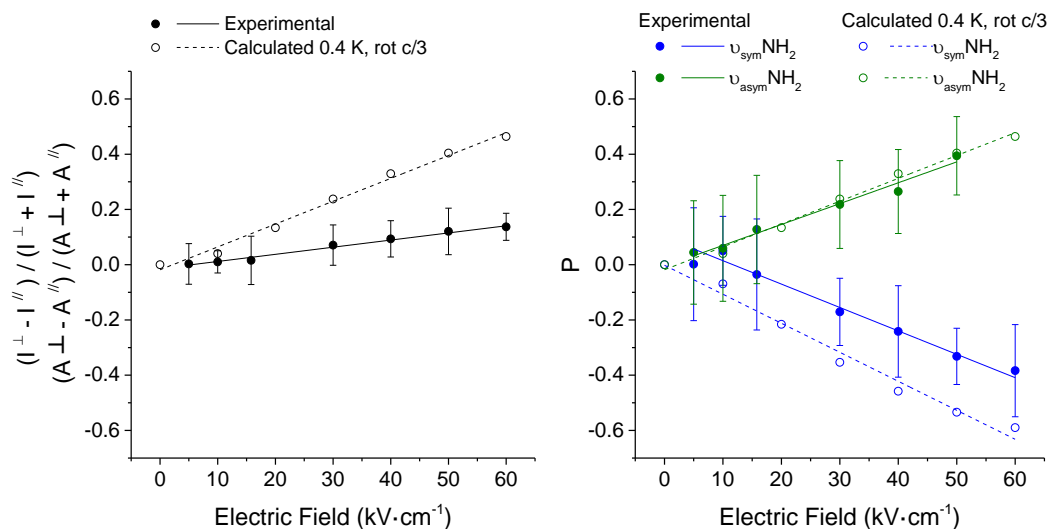


Figure 4-31. Left: Effect of the applied electric field on the ion yield generated after electronic excitation of aniline (expressed as the ratio of the averaged intensity from each laser polarisation) and comparison with simulated values at standard helium nanodroplet conditions (expressed as the ratio of the transition peak areas from each laser polarisation). Right: Effect of the applied electric field on the symmetric (solid line in blue, $\nu_{\text{sym}}\text{NH}_2$ at 3422 cm⁻¹) and antisymmetric (solid line in green, $\nu_{\text{asym}}\text{NH}_2$ at 3509 cm⁻¹) stretch transition intensity for neutral aniline and comparison with simulated values (dashed lines) at standard helium nanodroplet conditions both expressed as the difference ratios of the peak areas from each laser polarisation.

The next step was therefore to try extending the technique to ionic aniline. The IR excitation of the NH₂ stretching vibrations was measured. Three different ionisation energies and schemes were examined, each suggesting some degree of orientation. However, the deduced values under field-free conditions differed for these three methods suggesting a preferred orientation caused by the ionisation process. The achieved degree of orientation was smaller than for the neutral, which already indicated some discrepancy since the permanent dipole moment of the ion is greater than that of the neutral. Accordingly, the experimental data disagreed with the computed values. In order to explain this, several factors were investigated to determine their effect on the apparent orientation of the ions. The effect of the polarisation of the UV light was examined and discarded a preferred orientation of the ions caused by the ionisation process. Applying the orienting electric field after ionisation did not give conclusive results since different schemes led to contradictory results. The results for different droplet sizes agreed, indicating that if the desolvation mechanism of the ion from the droplet leads to modify the orientation it would do so in the same way regardless of the droplet size

dependence. All bands were found to be saturated. Measurements for reduced laser fluences showed similar values. Orientation of the neutral was observed at this reduced level of saturation and thus ruled this out as a reason for the poor degree of orientation. All these parameters considered, there does not seem to be an obvious reason one could control in the experiments that would give polarisation difference ratios closer to the calculated ones. Even though orientation of the ions can be confirmed to some extent, showed by the dependency with changing field, the measured degree of orientation is still questionable, see Figure 4-32.

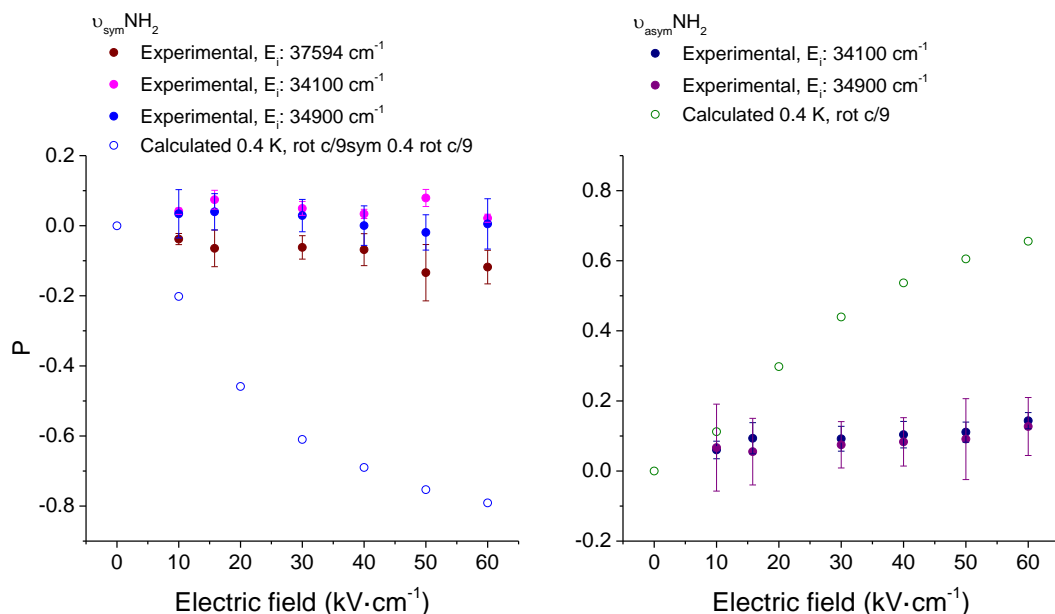


Figure 4-32. Effect of the IR polarisation on the symmetric ($\nu_{\text{sym}}\text{NH}_2$ at 3395 cm^{-1} , left) and antisymmetric ($\nu_{\text{asym}}\text{NH}_2$ at 3488 cm^{-1} , right) stretch transition intensity for cationic aniline ionised in three different ways (expressed as the difference ratios of the peak areas from each laser polarisation) as a function of the applied electric field and comparison with simulated values at standard helium nanodroplet conditions for ions (dashed lines). $E_i = 37594 \text{ cm}^{-1}$ non-resonant ionisation, $E_i = 34100 \text{ cm}^{-1}$ resonant ionisation via the $S_1 \leftarrow S_0$ band origin, $E_i = 34900 \text{ cm}^{-1}$ resonant ionisation via the 12_0^1 vibronic band of the $S_1 \leftarrow S_0$ transition.

The results leave room for further investigation. In all cases, the maximum experimental applied field in our setup, 60 $\text{kV}\cdot\text{cm}^{-1}$, could not achieve complete orientation of the species. Systems with higher permanent dipole moments would be needed to achieve this.

5 ION SPECTROSCOPY OF SODIUM ION WATER COMPLEXES

5.1 INTRODUCTION

The presence of water in many biological processes and water's unique properties resulting from strong hydrogen bonding make it a molecule of special interest that is still studied^[121-123]. Reactions of water with other molecules typically lead to hydrolysis, hydration, or solvation complex formation. Hydration is the addition of a water molecule to a substance. In organic chemistry, hydration of unsaturated compounds is broadly employed to form alcohols, amides, etc. The term 'solvation' is employed in inorganic chemistry when neutral and ionic species are surrounded or complexed by a solvent. The solvent-solute interaction (electrostatic, van der Waals or a hydrogen bond) stabilises the complex. Hydrolysis is the reaction of a compound with water involving ionisation and fragmentation of water. Hydroxides of metals and hydrogen halides are typical reaction products. A well-known example of hydrolysis is the formation of sodium hydroxide by mixing solid sodium and water. Microscopically this product is not present though; the reaction of only one sodium atom with water molecules or clusters leads to solvation clusters $\text{Na}(\text{OH}_2)_n$. At least three sodium atoms are needed to obtain products of hydrolysis^[124-126] other than $\text{Na}_m(\text{OH}_2)_n$ van der Waals complexes. Such reactions between water and alkali metal atoms can also take place within superfluid helium nanodroplets.

The location of dopants in helium nanodroplets depends on the strength of the interaction between the dopant and helium relative to that between helium atoms. As a result of the weak interaction alkali metal atoms are located at the surface of helium droplets^[7, 127], while water molecules reside inside^[122, 128-129] like most polyatomics. Reactions between alkalis and typically solvated dopants are not impeded by this spatial distribution, and the alkali may become solvated^[130] or lead to products near^[131] or outside the droplet's surface. The reaction between sodium and water clusters embedded in helium droplets was studied by Stienkemeier and Koslowski^[132]. Solvation of sodium to form NaOH and Na(OH₂)_n complexes confirmed helium as an appropriate matrix to study reactions at cryogenic temperatures.

The goal of this research is to examine the formation of metal-ion water complexes (Na_m(OH₂)_n⁺) in helium droplets. When the sodium atom is ionised on the surface of a droplet containing water clusters in its interior, several scenarios can be considered: the ion dissociates from the droplet leaving the water intact, or the ion is attracted by the oxygen's electronegativity to form a Na_m(OH₂)_n⁺ product either outside, at the edge, or inside the droplet. Previous results in the group show that the sodium bound to the surface solvates into the droplet after ionisation^[60]. Therefore, formation of Na_m(OH₂)_n⁺ is expected to happen inside the droplets when the ion collides with the water.

Upon formation of Na_m(OH₂)_n⁺ in helium nanodroplets, rovibrational spectroscopy could give information about the dopant-helium interaction. The rotational constants of light neutral molecules in helium are close to gas-phase values due to weak coupling with the matrix^[30]. Experiments with water have shown a 2-3 % difference in the effective rotational constant^[128-129]. It would be interesting to study the rotational dynamics of the complex with a single ligand to see if the moment of inertia is somehow related to that of water and to which degree the helium-cation interaction affects the rotational constants of this light ionic rotor.

In this chapter, the results of several experiments performed to investigate this are discussed. In the first part, UV excitation spectra are acquired for Na(OH₂)_n⁺ with n = [1-7] products in the region around the ionisation energy (IE) of sodium using a variety of doping conditions. The kinetic energy distribution of the desorbed complexes is obtained from velocity map images. The second part looks at the vibrational excitation of the symmetric and asymmetric OH₂-stretches of Na(OH₂)_n⁺

in helium droplets. To understand the succeeding dissociation of the ionic complex from the droplet, time of flight and kinetic energy distributions are recorded before and after excitation.

5.2 EXPERIMENTAL APPROACH

The complexes are formed by a double pick-up process. The helium beam first passes through an oven at [100-120] °C containing sodium before entering the second doping chamber where water can be introduced via a leak valve with a pressure on the order of 10^{-5} mbar. Different nozzle temperatures ranging from 13 to 19 K are used, corresponding to droplet sizes ranging from 2150 to 10860 helium atoms per droplet.

Tunable UV light with a pulse energy of 30 mJ is generated by frequency doubling the output of a dye laser pumped by the third harmonic of a Nd:YAG laser. The light is tightly focused on the droplet beam with a 400 mm focal length lens placed 400 mm before the interaction region in the optical path.

For pump-probe experiments, the IR light (typically $120 \text{ mJ} \cdot \text{cm}^{-2}$) of an OPO/OPA system pumped by a Nd:YAG laser is employed. The IR is focused by a 400 mm BaF₂ lens. To ensure lack of water vapour in the optical path, a nitrogen purging system is installed.

The experiments are performed using the VMI detector. Spectra are taken by monitoring the mass-selected ion signal as a function of the photon energy. To determine the species velocity as they desolvate from the droplets, photoion images are acquired at the arrival time of the ion of interest. The time-of-flight (TOF) distributions are recorded from the electric signal on the phosphor screen, which is sent to a multiple event time digitizer.

5.3 SUPPORT INFORMATION AND CONCEPTS

5.3.1 Pick-up probability and evaporative cooling loss

The number of dopants per droplet and the dissipated energy after pick-up can be estimated using some expressions. Poisson distributions give good probability approximations $P_k(z)$ of k impurities' capture in a helium droplet of a specific size^[60, 64, 122, 133].

The expression:

$$P_k(z) = e^{-z} \frac{z^k}{k!} \quad (5.1)$$

can be used to calculate the pick-up probability of a molecule in the doping chamber, where z is:

$$z = \frac{P_s L \sigma(N) F}{k_B T_s} \quad (5.2)$$

and corresponds to the average number of collisions leading to pick-up of an impurity travelling a distance L [m] (cell length). P_s [bar] is the cell pressure (second doping chamber), k_B [J · K⁻¹] is Boltzmann's constant, T_s [K] is the temperature of the scattering gas (impurity), $\sigma(N)$ [m²] is the cross-section of the droplet and F a correction factor ($F \geq 1$) that considers the increased collision probability of the helium beam passing through a scattering gas in motion. F follows the equation:

$$F = \frac{1}{\sqrt{\pi}} \left(\frac{1}{x} e^{-x^2} + \left(2 + \frac{1}{x^2} \right) \int_0^x e^{-t^2} dt \right) \quad (5.3)$$

where x is:

$$x = \frac{v_D}{\sqrt{\frac{2k_B T_s}{m_s}}} \quad (5.4)$$

and corresponds to the velocity of the droplet beam v_D [m/s] over the scattering gas most probable speed. m_s [kg] is the mass of the scattering gas.

The capture cross-section $\sigma(N)$ [m²] is assumed to equal that of the droplet,

$$\sigma(N) = \pi r^2 \quad (5.5)$$

and its radius r [m] is related to the number of helium atoms N by^[69]:

$$r = r_0 \sqrt[3]{N} \quad (5.6)$$

where r_0 is the radius of one helium atom (2.22 Å for ^4He).

When the molecule collides with the helium droplet, some energy is dissipated leading to shrinking the droplet by evaporative cooling. If the droplets are small this reduction in the cross-section cannot be neglected in the Poisson distribution's calculations.

The collision leads to dissipation of some energy $E_{pick-up}$ [cm^{-1}] from the kinetic energy of the collision E_{kin} , the molecule's internal energy E_{int} , and the binding energy of the impurity to the droplet E_{bind} ^[64, 133]:

$$E_{pick-up} = E_{kin} + E_{int} + E_{bind} \quad (5.7)$$

The kinetic energy is expressed as:

$$E_{kin} = \frac{m_S m_D}{2(m_S + m_D)} (v_S - v_D)^2 \quad (5.8)$$

where m_S and m_D [u] are the masses of the impurity and the droplet respectively and v_S and v_D [$\text{m} \cdot \text{s}^{-1}$] their velocities. This equation can be simplified considering the droplet mass is much larger than the impurity:

$$E_{kin} = \frac{m_S}{2} \langle (v_S - v_D)^2 \rangle \quad (5.9)$$

Applying the law of cosines to the speed vectors:

$$E_{kin} = \frac{m_S}{2} (\langle |v_S|^2 \rangle + \langle |v_D|^2 \rangle - 2\langle |v_S||v_D| \cos \theta \rangle) \quad (5.10)$$

Considering all orientations, the expression can be reduced to:

$$E_{kin} = \frac{m_S}{2} (v_S^2 + v_D^2) \quad (5.11)$$

The velocities of scattering particles have a Maxwell-Boltzmann distribution and can therefore be expressed as:

$$E_{kin} = \frac{3}{2}k_B T_s + \frac{m_s v_D^2}{2} \quad (5.12)$$

The internal energy of the molecule is the sum of the electronic, vibrational E_{vib} , and rotational E_{rot} energy. Considering the electronic energy is negligible:

$$E_{int} = E_{vib} + E_{rot} \quad (5.13)$$

To calculate the thermodynamic energy^[134]:

$$E = \frac{\partial \ln Q}{\partial \frac{1}{k_B T_s}} = k_B T_s^2 \frac{\partial \ln Q}{\partial T_s} \quad (5.14)$$

the rotational and vibrational partition functions Q have to be derived. Knowing that^[135]:

$$Q_{rot \text{ non-linear molecule}} = \sqrt{\frac{\pi}{ABC}} \left(\frac{k_B T}{hc} \right)^3 \quad (5.15)$$

where A, B, C [cm^{-1}] are the rotational constants, h [$\text{J} \cdot \text{s}$] Planck's constant and c [$\text{m} \cdot \text{s}^{-1}$] the speed of light. The rotational energy follows:

$$E_{rot} = k_B T_s^2 \frac{\partial \ln Q_{rot}}{\partial T_s} = \frac{3}{2} k_B T_s \quad (5.16)$$

The vibrational partition function neglecting the anharmonicities (vibration, rotation interaction)^[135]:

$$Q_{vib \text{ harm}} = \left(1 - e^{-\left(\frac{w_1 hc}{k_B T}\right)} \right)^{-d_1} \left(1 - e^{-\left(\frac{w_2 hc}{k_B T}\right)} \right)^{-d_2} \left(1 - e^{-\left(\frac{w_3 hc}{k_B T}\right)} \right)^{-d_3} \dots \quad (5.17)$$

where w_i are the fundamental vibrations, and d_i the degeneracy; and $\frac{w_i hc}{k_B T} = 1.4388 \frac{w_i}{T} [\text{cm}^{-1}]$. If $d_i = 1$,

$$E_{vib} = k_B T_s^2 \frac{\partial \ln Q_{vib}}{\partial T_s} = k_B T_s^2 \sum_i \left(\frac{1.4388 w_i}{T_s^2 (e^{1.4388 w_i / T_s} - 1)} \right) \quad (5.18)$$

With these expressions, the dissipated energy after pick-up can be calculated. Knowing that each evaporated helium atom carries away 5 cm^{-1} [69], the number of evaporated helium atoms is:

$$\Delta N_{He} = \frac{E_{pick-up}}{5} \quad (5.19)$$

The Poisson distribution can be then calculated considering the diminished cross-section due to evaporative cooling after pick-up or neglecting the losses.

5.3.2 Sodium dimer and solvation complexes

5.3.2.1 Sodium dimer

Ionisation of sodium dimer on helium droplets does not appear to have been studied in detail yet. Even though the ionic species has been observed, its ionisation energy is still not known. The energy required to directly ionise sodium dimer in gas phase ($X^2\Sigma_g^+ \leftarrow X^1\Sigma_g^+$) is 39480 cm^{-1} [136-137]. A shift of about 150 cm^{-1} from gas phase to helium conditions is expected, equivalent to that of the monomer [61]. However, one condition has to be kept in mind: the orientation of the valence electron spins. Whereas covalent sodium dimer is formed for a low-spin configuration ($\uparrow\downarrow$ or antiparallel, $X^1\Sigma_g^+$ singlet state) high spin configuration leads to a van der Waals bond ($\uparrow\uparrow$ or parallel, $A^3\Sigma_u^+$ triplet state). The weakly bound triplet dimers are usually difficult to study; the singlet dimers are favoured in gas phase and after molecular beam expansions. However, triplet sodium dimers form in greater abundance compared to singlet dimers on helium droplets. The evaporation of helium atoms caused by the energy liberated after singlet dimer formation may lead to dissociation of the dimer from the droplet or evaporation of small droplets. The weaker bond of triplet dimers allows formation on the droplet's surface since the required binding energy causes moderate droplet shrinkage, see Figure 5-1 [138]. The energy needed to ionise the higher energy triplet-state sodium dimers on helium droplets is therefore expected to be lower than the 39330 cm^{-1} estimated.

Knowing that the energy of the triplet state is 5850 cm^{-1} ^[139-140] higher than the singlet state and assuming that the ionisation energy for the two states is the same, this reports a value of 33480 cm^{-1} .

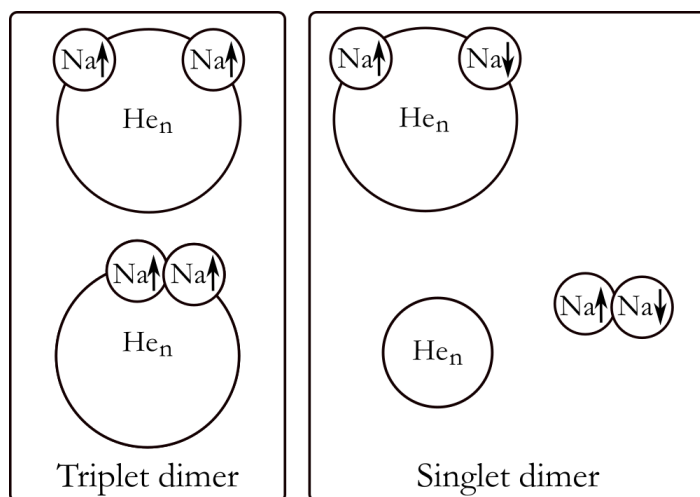


Figure 5-1. Scheme showing the formation of enriched triplet-state dimers on helium droplets compared to singlet. The higher binding energy of the singlet leads to small clusters evaporation or dissociation of the molecule. Reprinted with permission from ^[138]. Copyright (2019) American Chemical Society.

5.3.2.2 Ionic sodium monosolvated complex, $\text{Na}(\text{OH}_2)^+$

5.3.2.2.1 Ionisation energy

Studies have shown that sodium solvates in helium droplets to form predominantly $\text{Na}(\text{OH}_2)_n$ van der Waals complexes since the cluster reactions are less likely in the cryogenic droplet environment^[132]. The energy required to ionise $\text{Na}(\text{OH}_2)$ is calculated using Gaussian 09^[111]. The calculations are performed by DFT using the B3lyp functional and a 6-311++G(df,pd) basis set. After geometry optimisation of the neutral and ionic complexes, the adiabatic ionisation energy is obtained yielding a value of 35280 cm^{-1} . This value is very different to the sodium ionisation energy, which is 41300 cm^{-1} ^[60-61], and thus allows us to examine the formation of solvated ionic complexes upon ionisation of the alkali.

5.3.2.2.2 Geometry, rotational constants and vibrational band frequencies

Assuming the complexes are not directly desorbed after formation, rovibrational spectroscopy of the complex can give information about the rotational dynamics of the ionic species in the helium cluster.

The ionic complex rotational constants and the energies of its OH₂-stretching vibrational modes are calculated using Gaussian 09^[111] after geometry optimisation and are in Table 5-1. The anharmonic calculations are performed by second-order Møller–Plesset perturbation theory (MP2) using the augmented cc-pVTZ basis set.

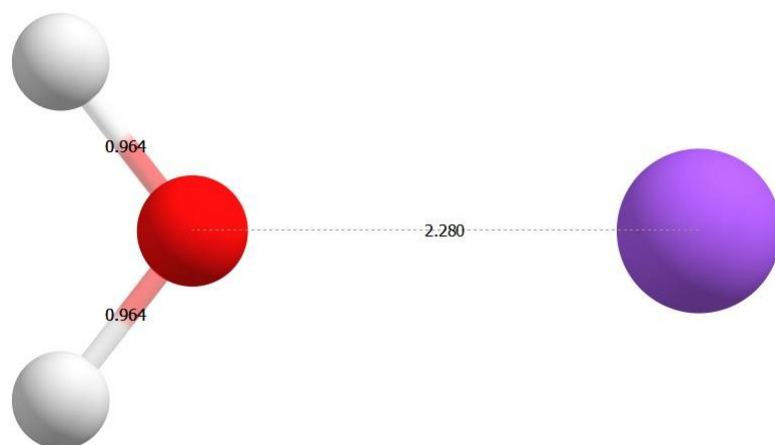


Figure 5-2. Optimised geometry of Na(OH₂)⁺ indicating the bond lengths calculated with Gaussian 09 (MP2-AUG-cc-pVTZ) and plotted with Chemcraft^[141].

The structure (C_{2v} point group) of the asymmetric top obtained after optimisation is shown in Figure 5-2. The axis of least moment of inertia is the symmetry axis; the A rotational constant is 14.45 cm⁻¹. Considered a prolate near-symmetric top, B and C give values of 0.3 cm⁻¹ and 0.294 cm⁻¹ respectively. The calculated energy for the symmetric stretch is 3627 cm⁻¹ and its transition dipole moment is parallel to the top axis resulting the rotational selection rule $\Delta K = 0$. The asymmetric stretch is perpendicular (corresponding to $\Delta K = \pm 1$) and it is calculated at 3706 cm⁻¹. These results match the ones obtained for Na(OH₂)⁺Ar^[142] well, benchmarking our calculations.

Table 5-1. Calculated energies [cm⁻¹] of the symmetric (ν_{sym}) and asymmetric (ν_{asym}) OH₂-stretching modes and rotational constants A , B and C [cm⁻¹] of the Na(OH₂)⁺ using Gaussian (MP2-AUG-cc-pVTZ).

	$\nu_{\text{sym}}\text{OH}_2$ (cm ⁻¹)	$\nu_{\text{asym}}\text{OH}_2$ (cm ⁻¹)	A (cm ⁻¹)	B (cm ⁻¹)	C (cm ⁻¹)
MP2, anharmonic	3627	3706	14.45	0.30	0.294

5.4 RESULTS

5.4.1 One laser experiments

To examine formation of ionic sodium solvation complexes in helium droplets after sodium ionisation and help understand the mechanism, several experiments are performed.

5.4.1.1 Excitation spectra of Na and water doped droplets: Rydberg states region and structure for $\text{Na}(\text{OH}_2)^+$

In a first experiment the excitation spectrum of helium droplets doped with both sodium and water was recorded. The nozzle temperature was 13 K or 18 K and a fixed oven temperature of 100 °C were used. The water doping conditions correspond to five and two molecules of water per droplet on average at 13 K and 18 K respectively. Following resonant-enhanced ionisation via the atom's Rydberg states, the ions are mass-selected and detected.

The excitation spectrum detecting the sodium cation, displayed in Figure 5-3 in black, shows the Rydberg states' structure and matches previous results in the group^[61]. Above the ionisation energy the gas-phase sodium atoms coming out of the oven are directly ionised giving rise to the signal observed at high wavenumbers (41300 to 41700 cm^{-1}). The Rydberg transitions are also observed when detecting $\text{Na}(\text{OH}_2)^+$ ions (Figure 5-3 in blue), although they appear much weaker and on a broad background. These features are better resolved and more intense for larger droplets conditions, as seen by comparing the spectra recorded when the nozzle temperature is 13 K (corresponding to 10860 helium atoms per droplet (N), Figure 5-3 top) and 18 K (N = 2750, Figure 5-3 bottom). The ionisation energy of the complex, calculated in 5.3.2.2, is 35280 cm^{-1} . The appearance of these features above the ionisation energy of the neutral complex suggests then excitation of the metal prior to complex formation. This indicates that the complexation is related to the sodium ionisation process. As this is a resonantly enhanced process, we cannot confirm from these measurements whether the formation of the complex occurs just after sodium ionisation or whether the water is already attracted to the excited sodium.

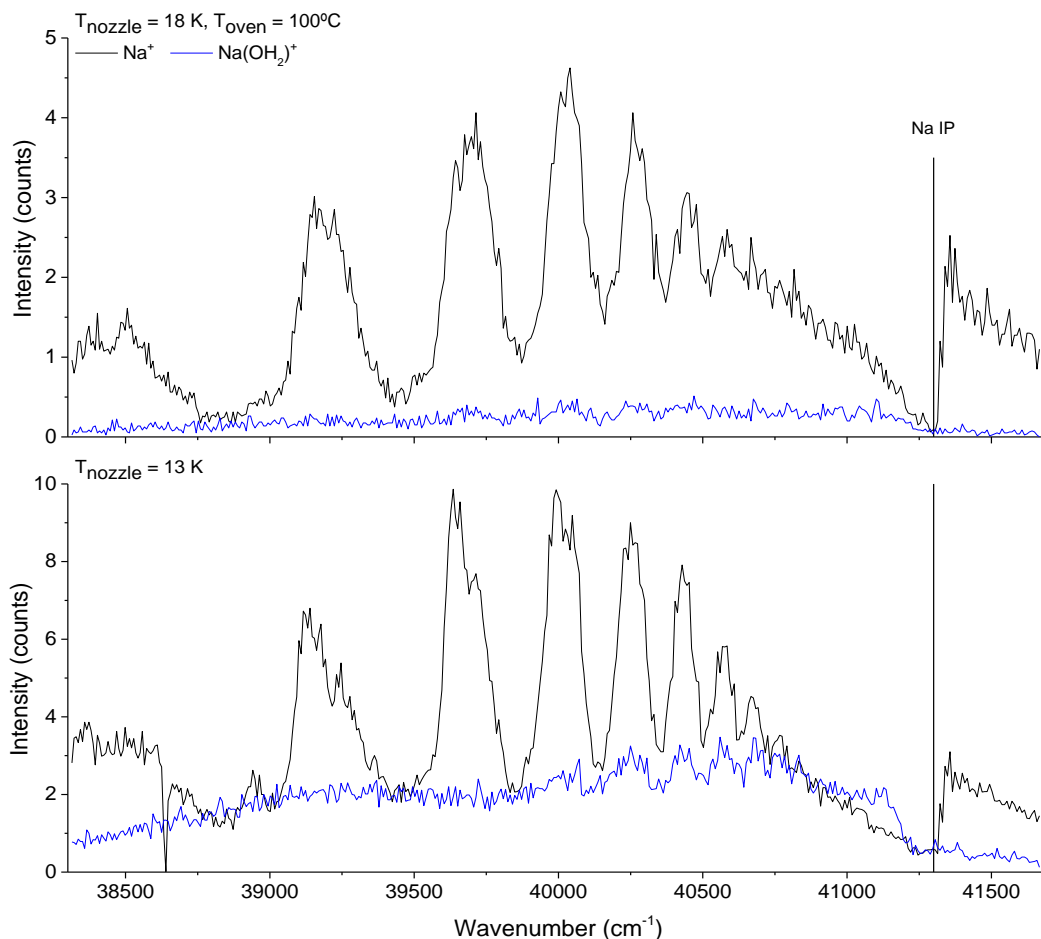


Figure 5-3. Excitation spectra of Na and water doped helium droplets detecting Na^+ (in black) and $\text{Na}(\text{OH}_2)^+$ (in blue) in the Rydberg states region of sodium up to the ionisation energy. The oven temperature is 100 °C and the nozzle temperature is 18 K (top) and 13 K (bottom).

5.4.1.1.1 Sodium dimer

To determine if sodium dimer contributes to the monomer's spectrum, their spectra are compared. The energies needed to ionise the singlet sodium dimer and triplet sodium dimer on helium droplets are calculated to be 39330 cm^{-1} and 33480 cm^{-1} respectively (see 5.3.2.1). Oven temperatures corresponding to 100, 110 and 120 °C were chosen to examine the effect of sodium doping. The experiments are performed with and without water doping. The nozzle temperature is 13 K.

All spectra are shown in Figure 5-4. The intensity of all ionic species increases with the oven temperature, as the droplets are more likely to be doped. The ionic monomer spectrum (a) presents a baseline that follows the shape of the ionic dimer signal (b). In the presence of water, the sodium dimer spectrum (e) shows a slightly

different pattern as this signal is largely dependent on the laser power. The monomer spectra both in the presence (c) and absence (a) of water suggest that fragmentation of the sodium dimer possibly contributes to the monomer signal. This in turn contributes to the signal below the ionisation energy of sodium when the laser frequency is not resonant to the Rydberg states. The signal of $\text{Na}(\text{OH}_2)^+$ (d) at high wavenumbers is more intense and thus contribution to the monomer can be discarded. Similarly, the profiles of Na_2^+ and $\text{Na}_2(\text{OH}_2)^+$ do not coincide.

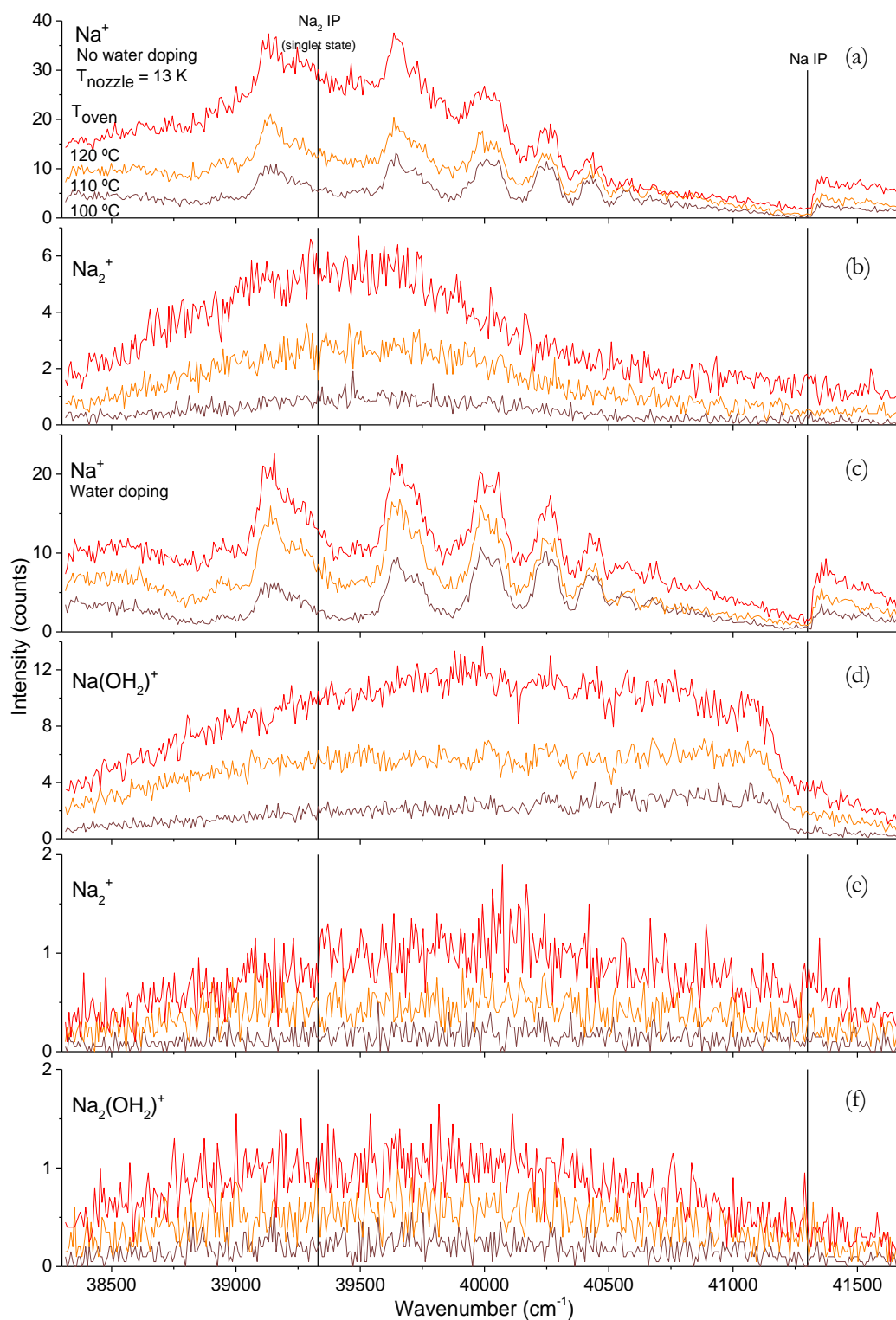


Figure 5-4. Mass-selected spectra of Na^+ , Na_2^+ (with and without water doping) and of $\text{Na}(\text{OH}_2)^+$. The nozzle temperature is 13 K and several oven temperatures are examined (100, 110 and 120 °C).

5.4.1.2 $\text{Na}(\text{OH}_2)_n^+$ spectra below and above ionisation energy

To examine formation of $\text{Na}(\text{OH}_2)_n^+$ complexes in helium droplets after sodium ionisation, the UV light is scanned from 41000 to 41800 cm^{-1} to compare the ion yield of different cluster sizes below and above the ionisation energy of sodium (at 41300 cm^{-1} [60-61]; $^1\text{S}_0 \leftarrow ^2\text{S}_{1/2}$ one-photon ionisation^[143]). $\text{Na}(\text{OH}_2)_n^+$ for $n = 1-7$ complexes are mass-detected, and several droplet sizes ($N = 2150-10860$) are examined for an oven temperature of 100 °C. The water doping conditions correspond to 5, 3, 2 and 2 water molecules per droplet on average for 13, 15, 17 and 19 K of nozzle temperature respectively.

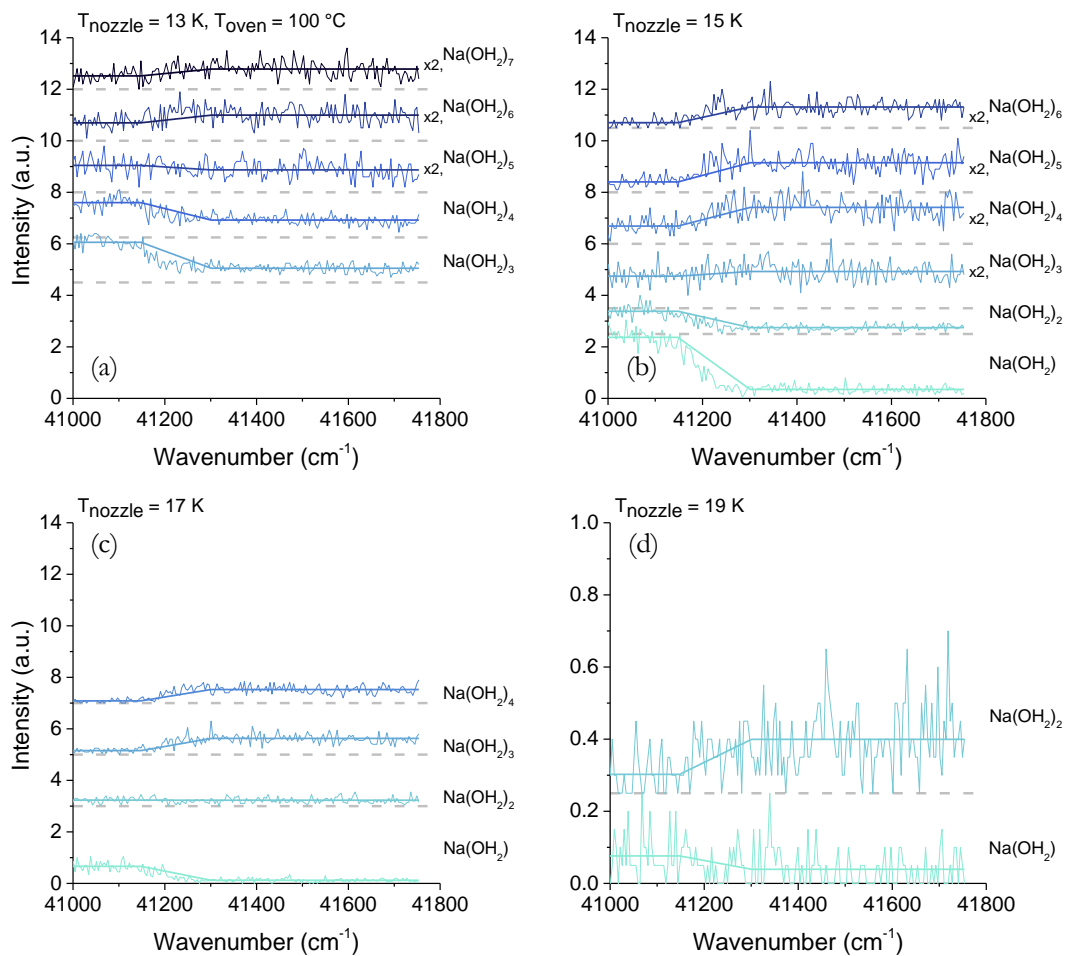


Figure 5-5. Excitation spectra of Na and water doped helium droplets detecting $\text{Na}(\text{OH}_2)_n^+$ ($n = 1-7$) at nozzle temperatures of 13 K (a), 15 K (b), 17 K (c), and 19 K (d). The oven temperature is set to 100 °C. The dashed lines correspond to the baseline of every measurement. The solid lines are the averaged values from 41000 to 41150 and from 41300 to 41800 cm^{-1} to facilitate perceiving the intensity below and above 41300 cm^{-1} .

Figure 5-5 comprises the obtained spectra distributed by helium droplet size for complexes with increasing number of water molecules. The ion yields below and above 41300 cm^{-1} present two case scenarios: the intensity can raise or drop. The results at 15 K, summarised in Table 5-2, will be taken as an example to explain the process. Figure 5-6 shows the different scenarios.

Table 5-2. Summary of the possible scenarios at 15 K. The effects are interpreted from the results obtained for $\text{Na}(\text{OH}_2)^+$ and $\text{Na}(\text{OH}_2)_6^+$ when the nozzle temperature is 15 K and the UV energy is below and above sodium's ionisation energy.

Below Na's IE [41000-41300] cm^{-1}			Above Na's IE [41300-41750] cm^{-1}	
	Ion yield	Effect	Ion yield	Effect
$\text{Na}(\text{OH}_2)^+$	+	<i>“Desorbed”</i>	≈ 0	<i>“Solvated”</i>
$\text{Na}(\text{OH}_2)_6^+$	≈ 0	<i>“Desorbed”</i>	+	<i>“Evaporated”</i>

Below the ionisation energy, the signal of $\text{Na}(\text{OH}_2)^+$ is nearly constant. In this case (1+1)-REMPI leads to formation and detection of the bare ionic complex (Figure 5-6, A.). The fact that the ionic sodium does not solvate into the droplet to result in an embedded ionic complex is probably caused by the ionisation process, as already mentioned in 5.4.1.1. When excited, the sodium starts to dissociate from the droplet (illustrated by the arrow) attracting a molecule of water with it and leaving the droplet as it is ionised. Even though we cannot confirm from these measurements whether the complexation occurs just after ionisation, this is probably not the case. For the sodium to attract the water, the distance between the two must be relatively short. If sodium starts to dissociate once excited, it is more likely that the complex is formed before ionisation than after it, since the laser pulse length is on the order of nanoseconds and dissociation occurs on the order of picoseconds^[144]. Above the sodium's ionisation energy the intensity drops close to zero. In this case, the sodium atom is directly ionised and becomes solvated by the helium droplet where it forms the $\text{Na}(\text{OH}_2)^+$ complex (Figure 5-6, B.). As a result, almost no free $\text{Na}(\text{OH}_2)^+$ is observed.

In contrast to $\text{Na}(\text{OH}_2)^+$, the signal of $\text{Na}(\text{OH}_2)_6^+$ below 41300 cm^{-1} is close to zero. Most likely the formation of such large complexes upon excitation of sodium is not efficient (Figure 5-6, C.). Analogously, the formation of NaHe_n^+ complexes was found to be limited to four helium atoms^[60]. For energies above sodium's ionisation energy, the $\text{Na}(\text{OH}_2)_6^+$ ion yield increases. The formation of a large $\text{Na}(\text{OH}_2)_6^+$ ionic

cluster will release a considerable amount of energy into the droplet. More specifically, after binding the six water units the generated energy equals 33175 cm^{-1} [145], which will cause evaporation of about 6600 helium atoms (see Table 5-3). Depending on the droplet size this can mean complete evaporation of the helium surrounding the complex (Figure 5-6, D.).

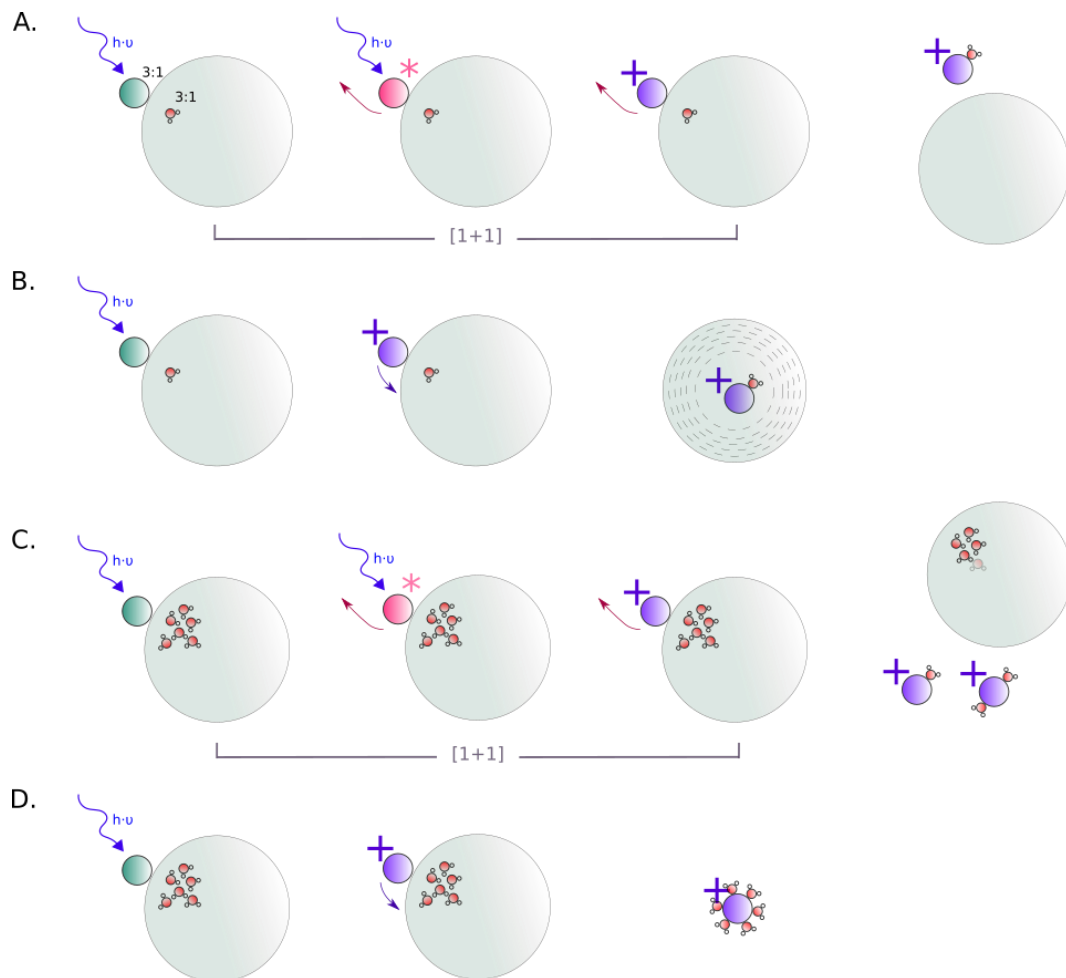


Figure 5-6. Ionic complexes ($\text{Na}(\text{OH}_2)^+$ and $\text{Na}(\text{OH}_2)_6^+$) formation scheme for helium droplets of $\sim 39\text{ \AA}$ radius: A. ‘Desorbed’: (1+1)-REMPI of sodium leads to complex dissociation outside the helium droplet. When excited, the sodium already starts to dissociate from the droplet (illustrated by the arrow) attracting a molecule of water with it and leaving the droplet as it is ionised. B. ‘Solvated’: After direct ionisation, ionic sodium solvates forming the ionic complex. C. ‘Desorbed’: $\text{Na}(\text{OH}_2)_6^+$ is not observed after (1+1)-REMPI of sodium. Most likely the formation of such large complexes upon excitation of sodium is not efficient. D. ‘Evaporated’: Direct ionisation of sodium. The bare ionic complex is detected; the energy released by the formation leads to complete helium evaporation.

For bigger droplets, Figure 5-5 (a), the complexes' ion yield decreases above the ionisation energy for $\text{Na}(\text{OH}_2)_n^+$ with $n = [1, 5]$ indicating that these complexes become solvated by the droplet. For the larger complexes, with $n = [6, 7]$, the yield above the ionisation energy increases. The energy released by the formation of these complexes is sufficient to completely evaporate the droplet. The dependence on the droplet size is evident, larger droplets can host larger complexes. The 'limit' number of water ligands of embedded complexes (n) goes from 5 (Figure 5-5 (a)) to 1 (Figure 5-5 (d)). This matches fairly well with the number of evaporated helium atoms after pick-up and complex formation, see Table 5-3.

Table 5-3. Generated energy [cm^{-1}] after water and sodium complexation for increasing number of water molecules and calculated number of evaporated helium atoms. The last column gives the total number of evaporated helium atoms for formation of $\text{Na}(\text{OH}_2)_n^+$ complexes from atomic Na^+ , from the sum of each of the individual complexation steps.

	Energy (cm^{-1})	Number of evaporated helium atoms	Total
$\text{Na}^+ + \text{H}_2\text{O} \rightarrow \text{Na}(\text{OH}_2)^+$	7908	1582	-
$\text{Na}(\text{OH}_2)^+ + \text{H}_2\text{O} \rightarrow \text{Na}(\text{OH}_2)_2^+$	6850	1370	2952
$\text{Na}(\text{OH}_2)_2^+ + \text{H}_2\text{O} \rightarrow \text{Na}(\text{OH}_2)_3^+$	5877	1175	4127
$\text{Na}(\text{OH}_2)_3^+ + \text{H}_2\text{O} \rightarrow \text{Na}(\text{OH}_2)_4^+$	4600	920	5047
$\text{Na}(\text{OH}_2)_4^+ + \text{H}_2\text{O} \rightarrow \text{Na}(\text{OH}_2)_5^+$	4180	836	5883
$\text{Na}(\text{OH}_2)_5^+ + \text{H}_2\text{O} \rightarrow \text{Na}(\text{OH}_2)_6^+$	3760	752	6635

5.4.1.3 Kinetic energy distribution

In order to highlight the different $\text{Na}(\text{OH}_2)_n^+$ processes, velocity map images are recorded from which the kinetic energies of the desorbed Na^+ and $\text{Na}(\text{OH}_2)_n^+$ with $n = [1-7]$ can be obtained. In this study, two energies are employed: below (40984 cm^{-1}), and above (41408 cm^{-1}) sodium's ionisation energy. The effect of the droplet size is also examined; the doping conditions correspond to five, three and two water molecules per droplet on average for droplets containing 10860, 4620, and 2150 helium atoms and oven temperatures of 100, 110 and 120°C respectively.

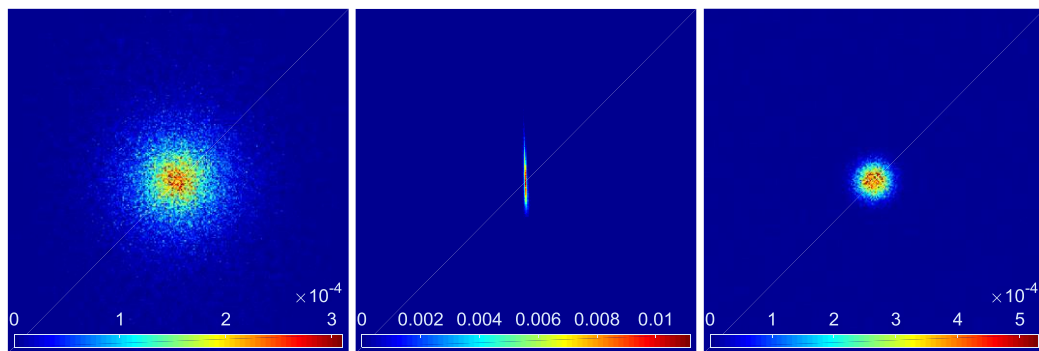


Figure 5-7. Velocity map images of Na^+ below IE, Na^+ above IE at 19 K of nozzle temperature, and $\text{Na}(\text{OH}_2)_7^+$ above IE at 13 K. Each image shows a 300×300 pixel frame around the centre. $Vr = 2000$ V.

Figure 5-7 left and middle correspond to ionic sodium monomer below and above the ionisation energy respectively. The appearance of a directional band in the latter indicates direct ionisation of sodium as it comes out of the oven, in a gas phase effusive beam, from which no speed information can be obtained by an inverse Abel transform due to lack of angular distribution. The remaining images present the typical diffuse ‘blob’ photoion VMI structure, from the expelled ions in all directions. The outer radius decreases with the number of water units of the complex (see Figure 5-7 left and right), sign of decreased maximum kinetic energy.

Obtained after an Abel inversion of the images, Figure 5-8 shows the speed distribution of the desorbed fragments. As already discernible in the raw images, the graphs confirm a systematic narrowing of the speed distributions with n , the number of water molecules in the complex. Comparison of the left (below the ionisation energy) and right (above the ionisation energy) figures’ distributions points out an energy dependence; the profiles being pushed to lower values above the ionisation energy. The contour corresponding to $\text{Na}(\text{OH}_2)^+$ at 41408 cm^{-1} exhibits otherwise with a broader profile, more similar to sodium’s speed distribution.

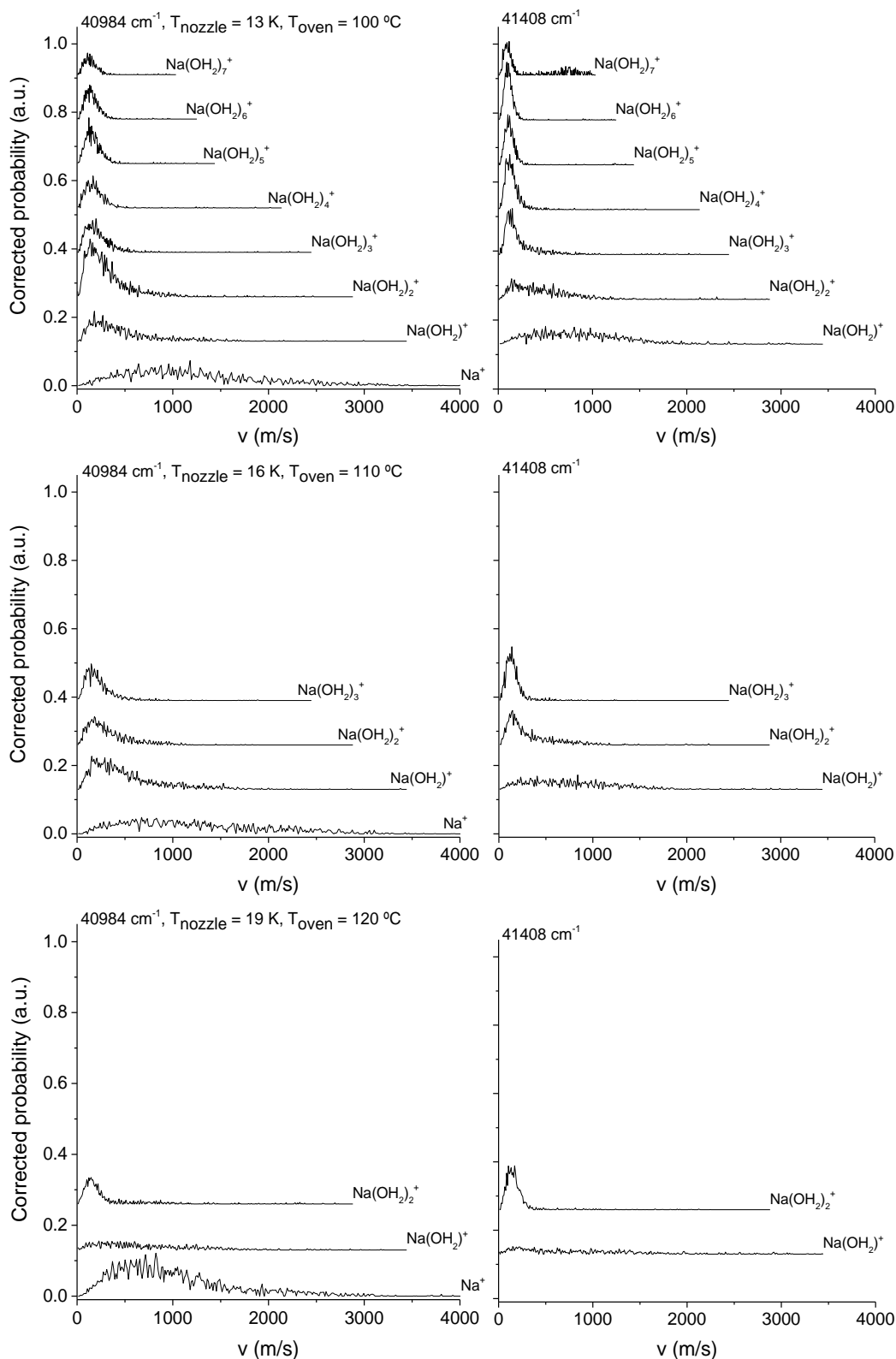


Figure 5-8. Speed distributions for Na^+ and $\text{Na}(\text{OH}_2)_n^+$ complex series ($n = [1, 7]$) at 13, 15 and 17 K nozzle temperature and 100, 110 and 120 °C oven temperature respectively.

The speed distributions are transformed into kinetic energy distributions for every particular mass and the energies derived as explained in 2.3.2. The values are plotted together in Figure 5-9 for comparison. No droplet size dependence is observed; the values do not follow a trend. The decrease in kinetic energy with water units is again confirmed. The largest values observed are of Na^+ and $\text{Na}(\text{OH}_2)^+$ at 41408 cm^{-1} around 1300 to 1900 cm^{-1} ; for $\text{Na}(\text{OH}_2)_{3-7}^+$, all values are below 300 cm^{-1} . Similarly to Na-He_p , heavier compounds give smaller kinetic energies^[146]. A possible explanation for this is that, assuming the complexes form in the droplets, a larger interaction with the solvation layer is expected in the case of larger molecules that might lead to some energy dissipation. In addition to that, the energy generated by forming the complexes is distributed into the more numerous vibrational modes of larger complexes. The kinetic energies obtained at the two ionisation energies, 40984 and 41408 cm^{-1} , are compared to examine the dependence on the ionisation methods. Whereas the mean kinetic energies of the complexes with more than three water molecules decrease ~ 50 to 80 cm^{-1} from 40984 to 41408 cm^{-1} , the kinetic energy of $\text{Na}(\text{OH}_2)^+$ increases up to 1000 cm^{-1} . Therefore no dependence on the ionisation method can be concluded.

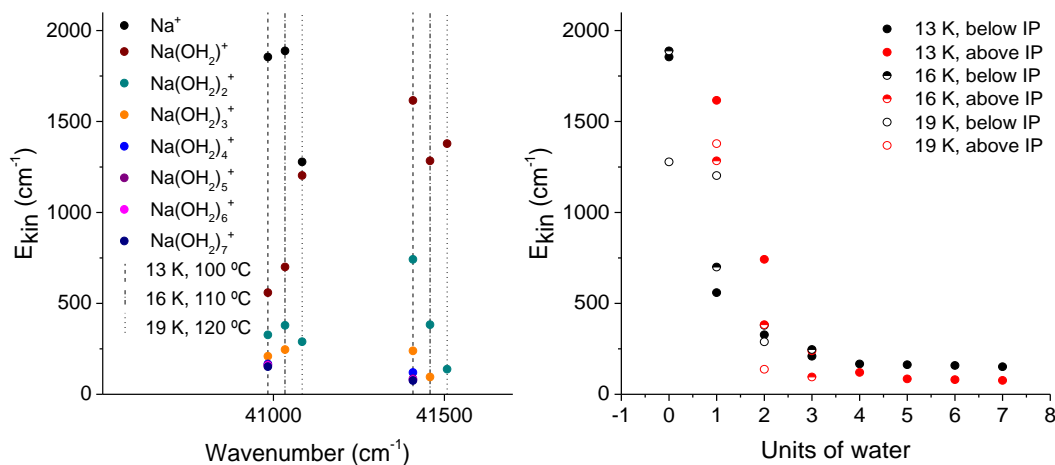


Figure 5-9. Average kinetic energies of different species (Na^+ and $\text{Na}(\text{OH}_2)_{1-7}^+$) below and above IE (40984 and 41408 cm^{-1} respectively) for 13 , 16 and 19 K and 100 , 110 and 120°C nozzle and oven temperatures respectively. Left: The values are plotted as a function of the laser energy. Data points at the same energy for different helium droplet sizes are horizontally displaced from each other for clarity. Right: The kinetic energies are plotted as a function of the number of complexed water ligands below (in black) and above (in red) sodium's ionisation energy.

5.4.2 Rovibrational spectroscopy of $\text{Na}(\text{OH}_2)^+$

Vibrational excitation of $\text{Na}(\text{OH}_2)^+$ after ionisation is performed to fully understand its formation mechanism in helium droplets. In addition, the rovibrational structure is analysed in order to investigate the rotation of ions in helium nanodroplets.

5.4.2.1 Spectrum

The chosen nozzle temperature to perform pump-probe experiments of $\text{Na}(\text{OH}_2)^+$ was 18 K. The oven was set to 100 °C. The water doping conditions corresponded to two water molecules per droplet on average. The UV light is fixed at 41408 cm^{-1} , i.e. above the ionisation energy of sodium. To record the excitation spectrum of $\text{Na}(\text{OH}_2)^+$ the IR is pulsed 50 ns after the UV pulse and scanned in the region of the symmetric and asymmetric OH_2 -stretches of $\text{Na}(\text{OH}_2)^+$. No literature values of the complex in helium are found, so clusters attached to argon ($\text{Na}(\text{OH}_2)^+\text{Ar}$) are taken as reference ($\nu_{\text{sym}}\text{OH}_2\text{-(Ar)} = 3634.5 \text{ cm}^{-1}$, $\nu_{\text{asym}}\text{OH}_2\text{-(Ar)} = 3707.0 \text{ cm}^{-1}$ [142]). In these studies, it was found that the rotational structure of the bands can be well described by a prolate symmetric top. In this context it should be mentioned that nuclear spin statistics gives rise to two distinct symmetry species for even and odd values of K , being the projection of the angular momentum onto the symmetry axis of the ionic system. As a result, a 3:1 intensity alternation is observed for transitions originating from odd and even values of K . Because the symmetry species do not interconvert, even at the lowest temperatures transitions starting from $K = 1$ transitions are stronger than those from $K = 0$. The excitation spectrum of $\text{Na}(\text{OH}_2)^+$ in helium droplets is shown in Figure 5-10. The spectrum presents rotationally resolved structure due to the cooling properties of the helium droplets.

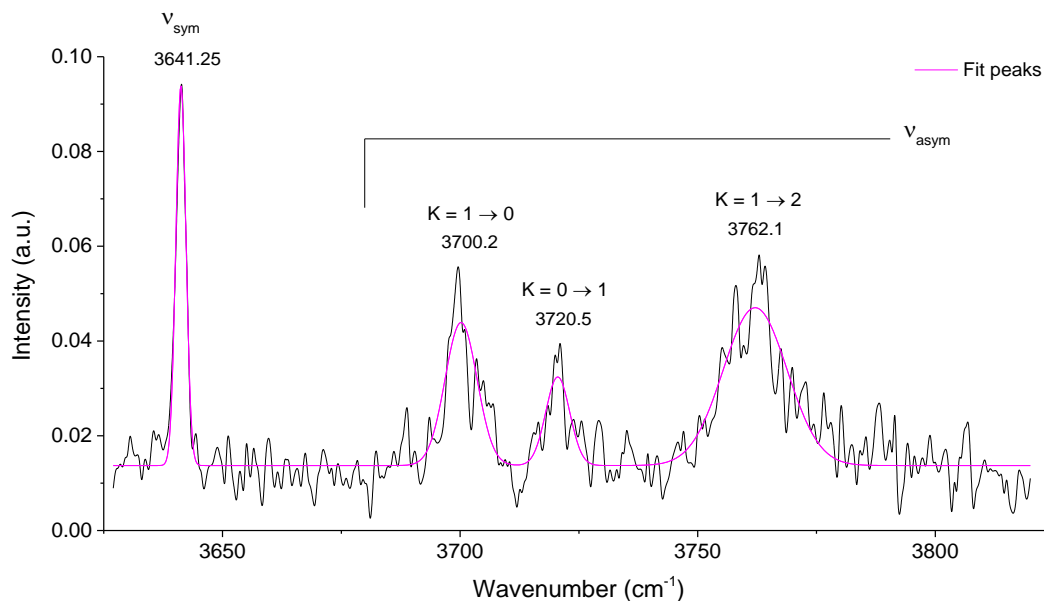


Figure 5-10. Rovibrational spectrum of $\text{Na}(\text{OH}_2)^+$ at the symmetric and asymmetric OH_2 -stretch region. The temperature of the nozzle is 18 K and the oven temperature is 100 °C. All peaks are Gaussian-fitted.

The spectrum is straightforward to assign as it is qualitatively similar to the $\text{M}^+(\text{H}_2\text{O})\text{Ar}$ cluster ions^[142, 147], see Figure 5-11. Even so, the spectra are different due to the different temperatures of the argon-containing cluster ions compared to the species in helium, 175 K versus 0.4 K. The peak values were obtained from a Gaussian function fitted to the data points. The band at 3641.25 cm^{-1} corresponds to the symmetric OH_2 -stretch. Its transition dipole moment is parallel to the symmetry axis and thus only $\Delta K = 0$ transitions are allowed. The narrow linewidth of this transition, 2.5 cm^{-1} , directly reflects the low internal temperature of the species in helium droplets. A comparison of transition frequency of this band with the gas phase spectrum of the argon complex reveals a blue-shift of 7 cm^{-1} , which is significantly larger than found for neutral systems but similar to what has been found for other ions. The bands observed above 3650 cm^{-1} correspond to the rotational structure of the asymmetric OH_2 -stretch. The transition dipole moment in this case is perpendicular to the symmetry axis explaining the observed rotational structure corresponding to $\Delta K = \pm 1$ transitions. Following the analysis in reference^[147], the peaks at 3700.2, 3720.5 and 3762.1 cm^{-1} are assigned to the $K = 1 \rightarrow 0$, $K = 0 \rightarrow 1$ and $K = 1 \rightarrow 2$ transitions respectively.

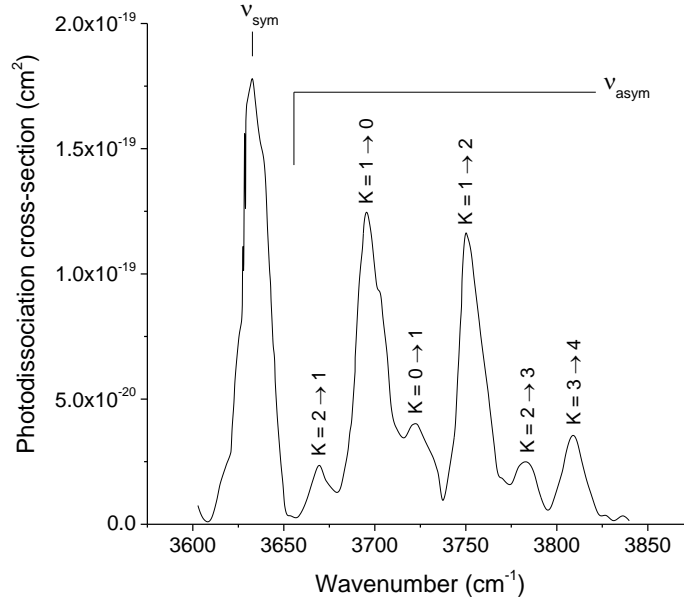


Figure 5-11. Experimental spectrum of $\text{Cs}^+(\text{OH}_2)\text{Ar}$ showing the vibrational bands and subbands. Adapted from [147].

In order to know if the ionic complex-helium interaction modifies the moment of inertia of this light rotor, the A rotational constant could be extracted from the K -subbands of the asymmetric stretch. The value can be compared to that of the $\text{Na}^+(\text{H}_2\text{O})\text{Ar}$ cluster. Additionally, since the heavy atoms lie on the symmetry axis of the complex, the A rotational constant is essentially the B rotational constant of water and can also be compared to it. It seems reasonable to think that if the ionic dopant-helium interaction were to affect the rotational constants a larger effect would be expected for B and C , as the sodium ion becomes constrained. The spacing between the $\Delta K = \pm 1$ transitions, of 20.3 and 41.6 cm^{-1} , differs strongly from the symmetric splitting of 23 cm^{-1} observed in the gas phase and already suggests a distortion of the energy levels.

To obtain more insight into the underlying mechanisms one might try to analyse the spectrum assuming a prolate slightly asymmetric top. In this case, the rotational energy including the centrifugal-distortion terms is given by^[135]:

$$F(J, K) = \tilde{B}J(J+1) + (A - \tilde{B})K^2 - D_J J^2(J+1)^2 - D_{JK}J(J+1)K^2 - D_K K^4 \quad (5.20)$$

where $\tilde{B} = \frac{1}{2}(B + C)$.

In order to estimate the A rotational constant, one could fit the energy of the observed transitions knowing that $\Delta K = \pm 1$. Given that the values of \tilde{B} , D , and

the band origin are also unknown, this is not possible with only three transitions. That being the case, we have taken several approaches in trying to determine A by simplifying the expression.

Vaden et al.^[147] estimate the band origin and the A rotational constant of $\text{Cs}^+(\text{H}_2\text{O})\text{Ar}$ by considering it a symmetric top, and neglecting the contributions of the $\tilde{B}J(J+1)$ and centrifugal-distortion terms and assuming identical rotational constants for the vibrational states involved. Therefore fitting the subbands to:

$$\nu = \nu_0 + \tilde{A}(K_2^2 - K_1^2) \quad (5.21)$$

where ν_0 is the band origin and K_1 and K_2 correspond to the ground and excited vibrational level and respectively and $\tilde{A} = A - \tilde{B}$ is the effective A rotational constant. Obviously, this approach is not valid for describing our system since the spacing of the peaks in the spectrum is not symmetric. When nonetheless trying to do so, one finds a value of $\tilde{A} = 15 \pm 3 \text{ cm}^{-1}$ where the large error reflects the failure of the model.

I will now explain four additional approaches considered. The results of these are summarised in Table 5-4 together with the experimental energies of the symmetric and asymmetric OH_2 -stretch vibrational bands and the rotational constants of free water^[148], $\text{Na}(\text{OH}_2)^+$ attached to argon^[142] and the values calculated in section 5.3.2.2.2 for comparison.

(1) First, we considered the next simplest option to obtain both the A and B rotational constants. Again we assume they don't significantly change from the ground to the excited vibrational level. We used the expression of the prolate symmetric top and disregarded the centrifugal-distortion terms. This yields:

$$\nu = \nu_0 + \tilde{B}J_2(J_2 + 1) - \tilde{B}J_1(J_1 + 1) + (A - \tilde{B})K_2^2 - (A - \tilde{B})K_1^2 \quad (5.22)$$

where the subscripts 1 and 2 correspond to the ground and excited vibrational level respectively. We next assume that only the lowest J levels are populated, i.e. $J = 0$ for $K = 0$ and $J = 1$ for $K = 1$.

We then considered all transitions allowed by the $\Delta J = 0, \pm 1$ selection rules and obtained 31.39 cm^{-1} and -10.61 cm^{-1} for A and \tilde{B} respectively for $K_1 = 1, J_1 = 1 \rightarrow K_2 = 0, J_2 = 0$, and 15.48 cm^{-1} and 5.305 cm^{-1} if $K_1 = 1, J_1 = 1 \rightarrow K_2 = 0, J_2 = 2$. Obviously, these values for both the A and \tilde{B} constants are not physical.

(2) Then, we allowed the A rotational constants to be different for the ground and excited vibrational level. In this case, the $\tilde{B}J(J+1)$ term as well as the centrifugal-distortion terms had to be neglected to fit the transitions, giving:

$$v = v_0 + \tilde{A}_2 K_2^2 - \tilde{A}_1 K_1^2 \quad (5.23)$$

The obtained effective \tilde{A} rotational constants were 4.87 cm^{-1} and 11.93 cm^{-1} for the ground and excited vibrational level, respectively. Such a large positive change in the A rotational constant is not physical.

In the next two approaches, the importance of the centrifugal distortion was investigated. IR spectroscopy of neutrals in helium droplets has revealed that centrifugal distortion constants can be on the order of 10^{-2} to 10^{-4} [149-150], orders of magnitude larger than found in the gas phase. Since fitting D_J , D_{JK} , and D_K simultaneously is not possible from the experimental transitions, individual values of D_i were obtained from simpler expressions.

(3) To determine the D_K centrifugal constant, the terms $D_J J^2(J+1)^2$ and $D_{JK} J(J+1)K^2$ were set equal to zero and the $\tilde{B}J(J+1)$ term disregarded, yielding:

$$v = v_0 + (\tilde{A} K_2^2 - D_K K_2^4) - (\tilde{A} K_1^2 - D_K K_1^4) \quad (5.24)$$

We obtained values of 11.93 cm^{-1} and 1.77 cm^{-1} for constants \tilde{A} and D_K respectively. Although the distortion constant appears large, it is only a factor of 40 larger than that of gas phase H_2O^+ [151].

The last option (4) considered tried to determine D_{JK} and thus $\tilde{B}J(J+1)$, $D_J J^2(J+1)^2$ and $D_K K^4$ were neglected yielding:

$$v = v_0 + (\tilde{A} K_2^2 - D_{JK} J(J+1)K_2^2) - (\tilde{A} K_1^2 - D_{JK} J(J+1)K_1^2) \quad (5.25)$$

This yielded an effective \tilde{A} rotational constant of 7.52 cm^{-1} and a D constant of -1.326 cm^{-1} . Clearly these values are not physical.

Table 5-4. Experimental vibrational energies [cm^{-1}] of the symmetric and asymmetric OH_2^- stretching bands and rotational constant [cm^{-1}] of free water, $\text{Na}(\text{OH}_2)^+$ attached to argon and calculated values using Gaussian (MP2-AUG-cc-pVTZ). Obtained band origin [cm^{-1}], A and B rotational constants [cm^{-1}] and centrifugal-distortion constant D [cm^{-1}] obtained in helium droplets from the subbands for the different approaches.

	A (cm^{-1})	$\nu_{\text{sym}}\text{OH}_2$ (cm^{-1})	$\nu_{\text{asym}}\text{OH}_2$ (cm^{-1})
Free water ^[148]	14.507 ± 0.009 (B)	3657	3756
$\text{Na}(\text{OH}_2)^+ \text{-Ar}^{[142]}$	14.3	3634.5	3707.0
$\text{Na}(\text{OH}_2)^+ \text{MP2}$	14.45	3627	3706

$\text{Na}(\text{OH}_2)^+ \text{-HeD}$		$\nu_{\text{asym}}\text{OH}_2$ (cm^{-1})	A (cm^{-1})	B (cm^{-1})	D (cm^{-1})
Eq. (5.21)	3712 ± 6		15 ± 3	-	-
(1)					
when $K = 1, J = 1 \rightarrow K = 0, J = 0$	3710.37		31.39	-10.61	-
when $K = 1, J = 1 \rightarrow K = 0, J = 1$	-		-	-	-
when $K = 1, J = 1 \rightarrow K = 0, J = 2$	3694.45		15.48	5.305	-
(2)	3715.67		Ground: 4.87 Excited: 11.93	-	-
(3)	3710.36		11.93	-	1.77
(4)	3710.37		7.52	-	-1.326

For all the considered approaches the results give similar band origin values that could match the experimental spectrum. However, the calculated rotational constants in most cases yielded unphysical values. Only the 3rd option, which considered the D_K centrifugal constant, yielded values that might be physical. The effective rotational constant, $\tilde{A} = 11.93 \text{ cm}^{-1}$, is clearly smaller than the gas phase value and could very well reflect an increase of the moment of inertia due to the coupling of the helium. As already mentioned, the centrifugal constant, $D_K = 1.77 \text{ cm}^{-1}$, is large but reflects only a 40-fold increase compared to the gas phase value of H_2O^+ , which is not exceptional for fast rotating neutral molecules in helium droplets^[152]. Although an unambiguous analysis of the spectrum is not possible, it appears from the above that the effect of the helium on fast rotating ions is very similar to neutrals, i.e. a small reduction of the rotational constant and a large increase in the centrifugal distortion constant.

5.4.2.1.1 Calculations

To help interpret the experimental results and to try to explain the rotational constants of the light ionic rotor in helium, some additional calculations are performed.

Our first calculations, in 5.3.2.2.2, did not take into account any interaction of the complex with the medium. The experimental spectrum however suggests otherwise. To do so, a single helium was added in between both species, in a $\text{Na}^+\text{-He-O}$ sequence, to examine if the medium could modify the complex geometry. But, when optimising the structure, the sodium ion tends to insert itself in between the helium and oxygen, attracted by the oxygen's lone electron pairs, as shown in Figure 5-12. This indicates that the starting structure is not an equilibrium structure. Consequently, the $\text{Na}(\text{OH}_2)^+$ complex in helium will have a similar geometry as in the gas phase.

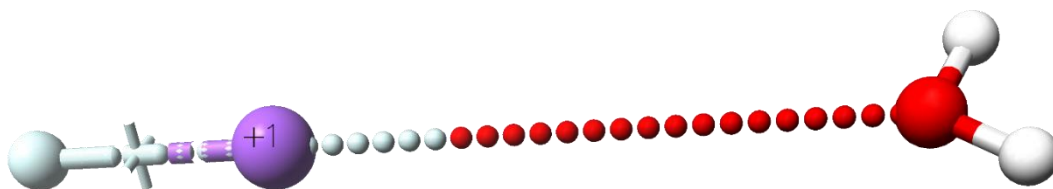


Figure 5-12. Optimised geometry of $\text{Na}^+\text{-He-OH}_2$ pointing out how the sodium ion is attracted by the lone pairs of oxygen and tends to sit in between water and helium. Plotted with SCIGRESS^[153].

If at all, the interaction of the helium with the solvated complex is expected to change the bond lengths and thereby change the rotational constants. Simulations are then performed for fixed shorter $\text{Na}^+\text{-O}$ bond lengths of the complex. The results, shown in Figure 5-13, give higher A rotational constant values. The energy required to yield a value of 15.5 cm^{-1} , as obtained using the last approach, is $470\text{ kJ} \cdot \text{mol}^{-1}$, discarding this possibility. Considering reasonably larger $\text{Na}^+\text{-O}$ bond lengths does not reproduce the calculated value of 12 cm^{-1} , from the second approach, either.

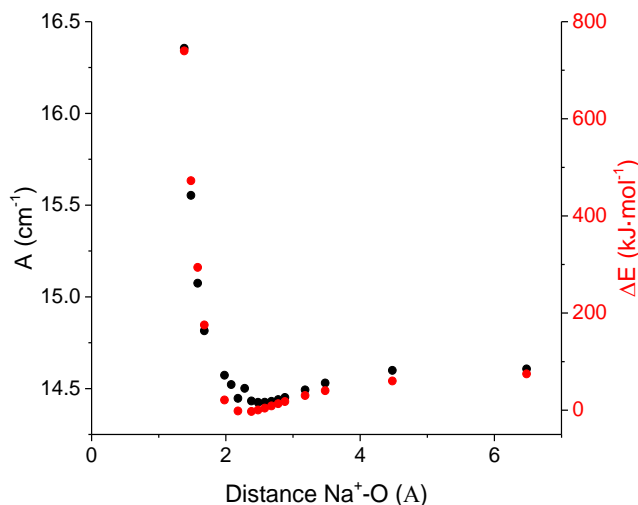


Figure 5-13. Rotational constant's dependence on $\text{Na}^+\text{-O}$ bond length and energy required. The values are obtained with Gaussian (MP2-AUG-cc-pVTZ) fixing the distance before performing the calculations.

5.4.2.1.2 Conclusion

It is clear from the IR spectrum that the helium strongly affects the energy levels of the ionic-alkali solvation complex. While the structure of the spectrum still largely resembles that of a symmetric top molecule, it cannot be described by a sensible set of rotational constants unambiguously. The ab initio calculations show that the geometry of the complex should resemble that of the gas phase and that a possible reduction of the $\text{Na}^+\text{-O}$ bond length due to surround helium will only lead to small variation in the A rotational constant. This indicates that in order to properly describe the IR spectrum, a full quantum calculation^[154] of the complete system, including the helium atoms, will be required.

5.4.2.2 Poisson distribution

The ion signal's pressure dependence is recorded for the band at 3641.25 cm^{-1} to confirm that the only species contributing to these peaks are monomer clusters. To form the complexes, a double pick-up process must take place. Assuming sufficient amount of sodium, the second doping chamber's pressure is monitored to calculate the distribution of $\text{Na}(\text{OH}_2)$ when adding water via the leak valve.

The pick-up probability of $\text{Na}(\text{OH}_2)$ in the doping chamber is calculated as explained in 5.3.1. Given the small size of the droplets (31 Å), the reduction in the cross-section after evaporative cooling cannot be neglected in the Poisson

distribution's calculations. Therefore, the dissipated energy after water and sodium pick-up is calculated (see Table 5-5).

Table 5-5. Number of evaporated helium atoms ΔN_{He} after sodium and water pick-up. Values of kinetic E_{kin} [cm^{-1}], internal E_{int} [cm^{-1}] and binding energy E_{bind} [cm^{-1}] for a given impurity temperature T_s [K] and mass m_s [u]. The velocity of the droplet beam v_D at 30 bar and 18 K is $387 \text{ m} \cdot \text{s}^{-1}$ [64]. Boltzmann constant is $0.695 \text{ cm}^{-1} \cdot \text{K}^{-1}$. The binding energies of sodium and water and taken from the literature^[133, 155].

	Sodium	Water
T_s (K)	371	293
m_s (u)	23	18
E_{kin} (cm^{-1})	530.1	417.62
		$w_1 = 3825.32$
w_i (cm^{-1})	-	$w_2 = 1653.91$
		$w_3 = 3935.59$
E_{int} (cm^{-1})	-	305.57
E_{bind} (cm^{-1})	13.1	258.1
$E_{pick-up}$ (cm^{-1})	543.2	981.29
ΔN_{He}	109	196

The Poisson distribution is calculated both considering the diminished cross-section due to evaporative cooling after pick-up and neglecting the losses (see Table 5-6 for input parameters), and compared to the experimental one, which is obtained monitoring the ion signal following IR excitation at 3641.25 cm^{-1} .

Table 5-6. Experimental values of the pressure P_s [mbar] and length L [m] of the doping cell, speed of the droplet beam v_D [$\text{m} \cdot \text{s}^{-1}$] at 30 bar and 18 K^[64], mass m_s [u] and temperature T_s [K] of the impurity and number of helium atoms N considering (or not) evaporative cooling.

P_s (mbar)	L (m)	v_D ($\text{m} \cdot \text{s}^{-1}$)	m_s (u)	k_B ($\text{J} \cdot \text{K}^{-1}$)	T_s (K)	$N_{\text{no evap cool}}$	$N_{\text{evap cool}}$
$[0.2, 570] \cdot 10^{-6}$	0.045	387	41	$1.38 \cdot 10^{-23}$	293	2750	2445

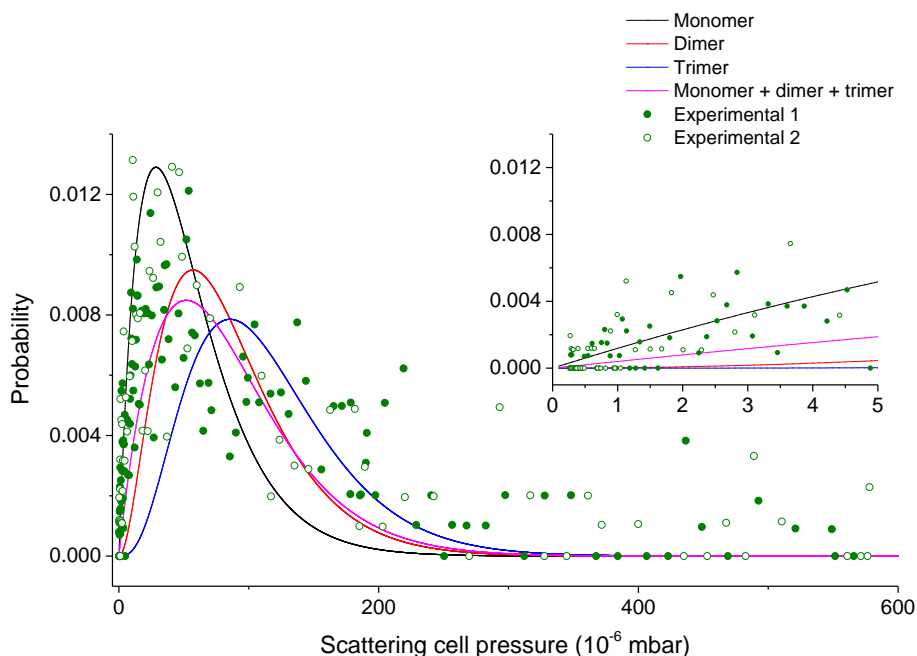


Figure 5-14. Calculated Poisson distributions for $\text{Na}(\text{OH}_2)^+$ after single, double and triple pick-up neglecting evaporative cooling loss of helium. Pressure dependence of the mass-selected $\text{Na}(\text{OH}_2)^+$ signal after excitation at 3641.25 cm^{-1} (scattered).

Figure 5-14 shows the comparison between the calculated and experimental values. Only the Poisson distributions neglecting the losses are plotted for comparison given that the difference caused by evaporative cooling was found to be subtle. The experimental data follows the curve of the monomer, with a maximum in the same region. The inset of the figure shows how the experimental values are distributed around the monomer distribution at low pressures confirming this assignment. Contribution of dimer and trimer clusters in the spectrum can be discarded; the pressure dependence of the signal can be assigned to $\text{Na}(\text{OH}_2)^+$ formed after a double pick-up.

5.4.2.3 TOF mass spectra

To obtain some insight about the $\text{Na}(\text{OH}_2)^+$ complex desolvation upon IR excitation, time-of-flight mass spectra before and after IR excitation of singly- (sodium) and doubly- (sodium and water) doped droplets are recorded.

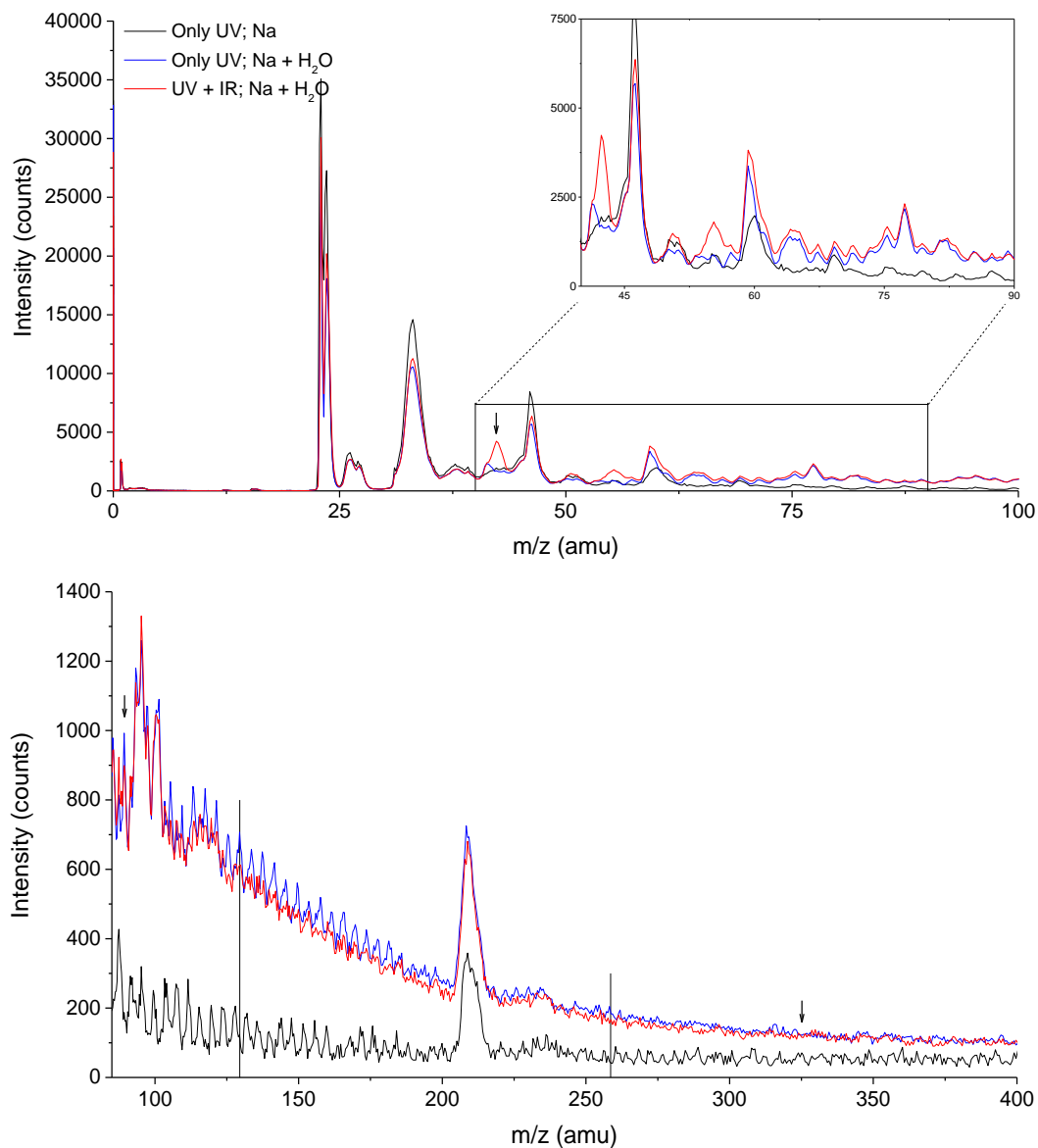


Figure 5-15. TOF mass spectra. Top: from 0 to 100 amu showing a rise at 41 uma after IR-excitation caused by desolvation of $\text{Na}(\text{OH}_2)^+$ from the droplet. The inset points out all the smaller clusters formed as a result of the excitation: $\text{Na}(\text{OH}_2)^+-\text{He}_p$ ($p = 1-9$). Bottom: the vertical arrows in the 85 to 400 uma region of the spectrum show a depletion, indication of dissociation from the hosting droplets. The solid lines show the 2 amu shift between the Na-He_r and $\text{Na}(\text{OH}_2)^+-\text{He}_p$ products of single and double pick-up confirming that the depleted series corresponds to ($p = 12-71$) clusters.

The flight distributions differ before and after excitation (only UV versus pump-probe) since the probe pulse causes ejection of the complex. As shown in Figure 5-15 top, the intensity corresponding to the complex at mass 41 amu rises after IR excitation. Signal depletion with IR is present at masses from 89 to 325 amu,

marked by vertical arrows on Figure 5-15 bottom. This 4 amu-spaced series corresponds to $\text{Na}(\text{OH}_2)^+-\text{He}_p$ clusters hosting the complex prior to excitation and subsequent desolvation. To confirm this assignment, distributions are recorded following single pick-up of sodium, which should yield Na^+-He_p products, and double pick-up of sodium and water, which should yield $\text{Na}(\text{OH}_2)^+-\text{He}_p$ products. The 2 amu horizontal shift between the TOF mass spectra proves that this is the case; $\text{Na}(\text{OH}_2)^+$ is solvated in droplets containing 12 to 71 helium atoms. The intensity gain from 45 to 77 amu, inset in Figure 5-15 top, indicates dissociation of $\text{Na}(\text{OH}_2)^+-\text{He}_{p'}$ clusters with $p' = 1-9$ in addition to the bare ionic complex after vibrational excitation.

5.4.2.4 Kinetic energy

Velocity map images were recorded to obtain the kinetic energy of $\text{Na}(\text{OH}_2)^+$ after excitation. A UV-only image was recorded for background subtraction. The kinetic energy of $\text{Na}(\text{OH}_2)^+$ upon desolvation is calculated from the speed distribution of the mass-selected species shown in Figure 5-16 right. The obtained kinetic energy is 78 cm^{-1} , noticeably smaller than the energy of $\text{Na}(\text{OH}_2)^+$ desorbed after ionisation, which is on the order of 1000 cm^{-1} (see section 5.4.1.3).

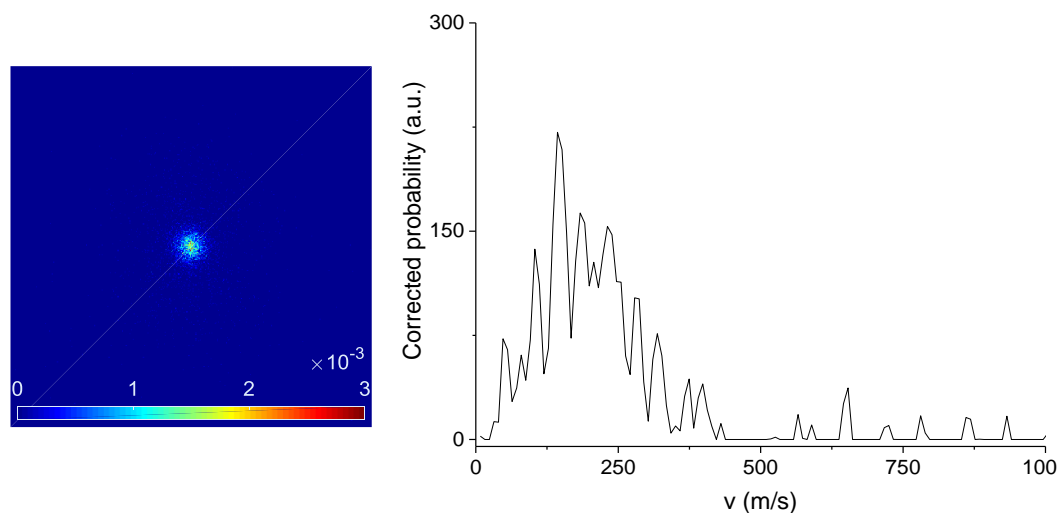


Figure 5-16. Left: Velocity map images of $\text{Na}(\text{OH}_2)^+$ after IR excitation. The image shows a 200×200 pixel frame around the centre. $V_r = 2000$. Right: Speed distribution of $\text{Na}(\text{OH}_2)^+$ escaping of the droplets after IR-excitation obtained from the velocity map image after subtraction of the background signal caused by the ionisation light.

5.4.2.5 Summary

IR spectroscopy of $\text{Na}(\text{OH}_2)^+$ was performed. The vibrational bands of the symmetric and asymmetric OH_2 -stretches were recorded. The assignment to $\text{Na}(\text{OH}_2)^+$ monomers was confirmed by the pressure dependence of the signal, matching the calculated Poisson distribution after single pick-up. From the TOF mass spectra, the desolvated species after excitation and the size of the hosting droplets were determined. Solvated in clusters containing 12 to 71 helium atoms, $\text{Na}(\text{OH}_2)^+$ desolvates from the droplet after vibrational excitation together with $\text{Na}(\text{OH}_2)^+-\text{He}_p$ clusters with $p' = 1-9$. The speed distribution obtained from VMI images allowed calculating the kinetic energy of the species escaping the droplets, equal to 78 cm^{-1} . It is clear from the IR spectrum that the helium strongly affects the energy levels of the ionic-alkali solvation complex. To estimate the degree of contribution, several approaches were taken to calculate the rotational constants by approximating it to a prolate symmetric top molecule. The results did not yield a sensible set of rotational constants, confirming that none of the employed approaches can describe it accurately and that full quantum calculations are required to describe the system.

5.5 SUMMARY

UV spectroscopy was used to investigate the formation of ionic sodium solvation complexes. To understand the role of photoionisation of the sodium atom to form the ionic complexes, the mass-selected ion yields of $\text{Na}(\text{OH}_2)_n^+$ complexes for $n = [1-7]$ were examined below and above the ionisation energy of the sodium. Below the ionisation energy, resonant-enhanced ionisation of sodium occurs via the atom's Rydberg states; above the ionisation energy the alkali is directly ionised. A first spectrum showed that the Rydberg transitions were also observed when detecting $\text{Na}(\text{OH}_2)^+$, indicating excitation of the metal prior to complex formation. From these measurements, we could not confirm whether the complexation happens right after excitation or ionisation. Regardless, the bare complex is detected after ionisation since it dissociates from the droplet. When directly ionising the alkali, the ionic atom solvates in the droplet and forms the complex. This is confirmed since the complex desolvates from the droplet after vibrational excitation. Formation of heavier $\text{Na}(\text{OH}_2)_n^+$ complexes after (1+1)-REMPI is not favoured though, since the sodium atom would need to drag several water molecules with it on its way out of the droplet. Direct ionisation is therefore more efficient to form these complexes. Moreover, bare $\text{Na}(\text{OH}_2)_n^+$ complexes were observed since their

formation releases a considerable amount of energy leading to droplet evaporation. This is then droplet size dependent, i.e. bare lighter complexes are more likely observed for smaller droplets, since their formation leads to complete evaporation, whereas bigger droplets are not completely evaporated and host the complex. The kinetic energies of the desorbed ionic species are lower for higher numbers of water molecules because more energy is dissipated to the droplet. However no clear dependence on the ionisation method was observed.

As mentioned, IR excitation of $\text{Na}(\text{OH}_2)^+$ leads to desolvation of the complex. From the TOF mass spectra, the desolvated species after excitation and the size of the hosting droplets were determined. This information, together with the fact that the sodium is solvated after ionisation, allowed us to disentangle the formation and desolvation of $\text{Na}(\text{OH}_2)^+$ step by step. The scheme in Figure 5-17 shows a representation of the mechanism. The sodium particle sitting at the droplet's surface (1) gets solvated (4) after ionisation (3) to meet the water. The hosting droplets contain 12 to 71 helium atoms as their size is reduced after ionisation. Vibrational excitation leads to dissociation (5) of the bare ionic complex with a kinetic energy of 78 cm^{-1} (a) and smaller clusters (of 1 to 9 helium atoms) (b). (Z1) and (Z2) point out the evaporative cooling loss of helium ensuing sodium and water pick-up.

In order to determine if the ionic dopant-helium interaction modifies the moment of inertia of this light ionic rotor, $\text{Na}(\text{OH}_2)^+$, the rovibrational structure of the asymmetric stretch was analysed. The asymmetric subband structure revealed a distortion on the energy levels compared to the gas-phase spectra indicating some contribution of helium to the moment of inertia. Even though the spectrum gives us confidence to confirm that helium contributes to the rotation of light ionic rotors, a quantitative degree of contribution is still missing.

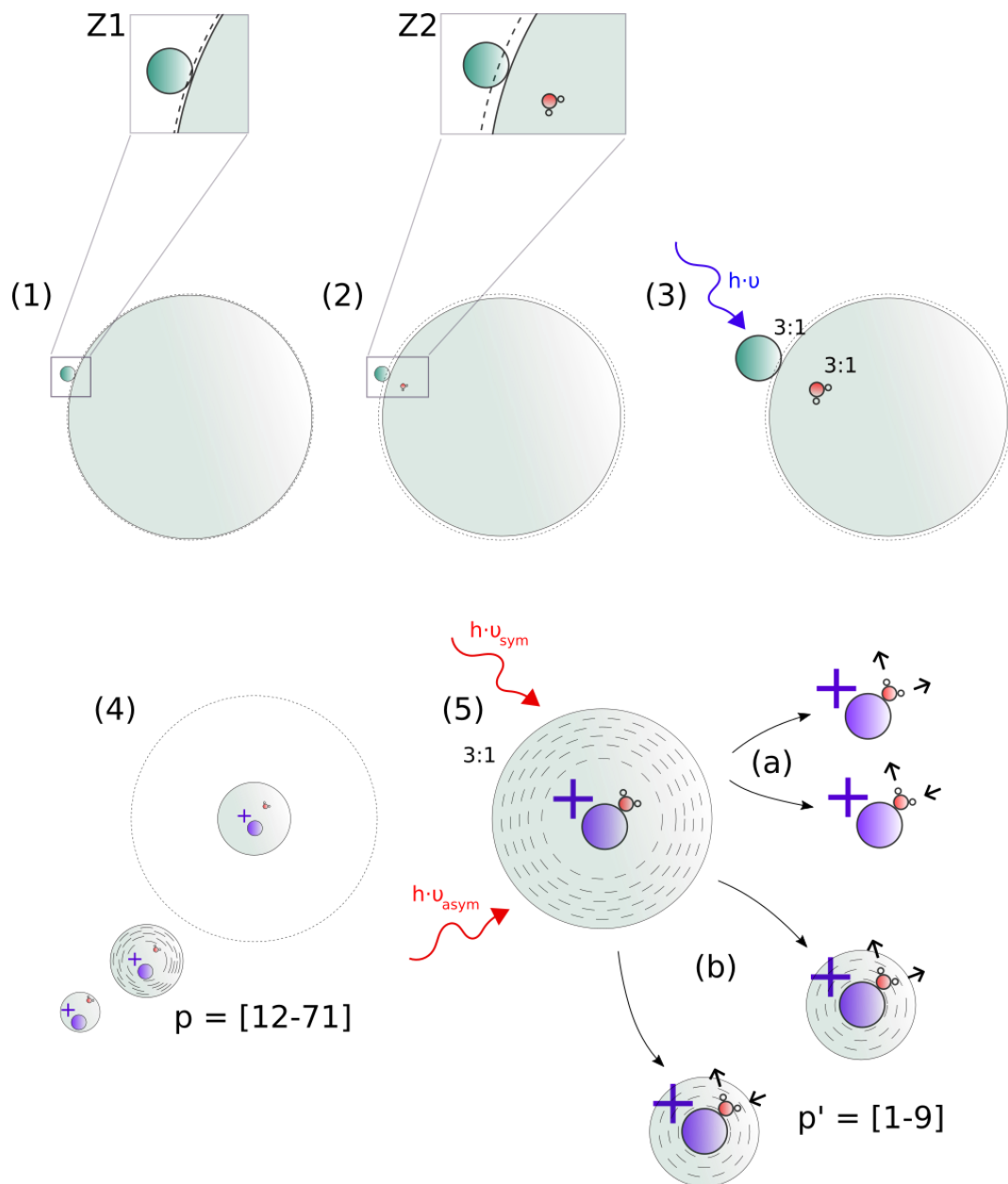


Figure 5-17. Ionic complex formation and desolvation scheme: (1) after the first pick-up, the sodium sits at the helium surface with a consequent number of evaporated helium atoms, (2) the water molecule gets solvated in the droplet remaining close to the edge due to a charge density interaction with the sodium atom; more helium atoms evaporate due to the pick-up process diminishing the droplet size, (3) the pump pulse is sent to ionise the sodium atom, (4) after ionisation, the size of the droplet decreases to tens of atoms [12-71] due to evaporation; the sodium gets solvated due to density interaction with the medium, (5) the probe pulse at the energy of the asymmetric and symmetric OH_2 -stretch vibration leads to (a) bare ionic complexes and (b) smaller size clusters of [1-9] helium atoms with the complex.

6 SUMMARY

The purpose of this thesis was to perform spectroscopy of ions in helium nanodroplets to widen our knowledge of these species themselves but also in this matrix, and to expand the range of experimental tools available to study them. The focus of this work was then to extend pendular state spectroscopy to molecular ions to determine structural information and to examine the formation of ionic metal solvation complexes upon photoionisation of the alkali and the interaction of the helium environment with this dopant.

As part of this thesis work, the existing reflectron TOF stage of the setup was reconfigured and made operational. Here, we have presented the first experimental results using this stage. Orientation of neutral aniline in the presence of high electric fields was first tested and used to validate the technique. Even though the degree of orientation probed by electronic spectroscopy disagreed with the computed values, the results probed via vibrational excitation were well-reproduced by the calculations and confirmed orientation of the neutral molecules. Vibrational spectroscopy of cationic aniline in the presence of increasing fields evidenced some degree of orientation. However, the calculated polarisation difference ratios showed a large discrepancy with the experimental values; the expected degree of orientation was significantly larger. Some experimental factors that we believed could influence the outcome were investigated in detail. The ionising laser energy, exciting laser power, lasers polarisations, helium droplets size and temporal delay of the orienting field with respect to the ionisation pulse were examined. The variation of the electric field dependence of the polarisation difference ratio with ionisation method seemed to indicate that the values indeed do not reflect the true degree of

orientation. The results pointed to some degree of orientation even for field-free conditions that suggested that the ionisation process leads to ions in a preferred orientation. However, lack of dependence on the ionising laser polarisation proved that this was not the case and that the initial orientation of the ions is not relevant for the final degree of orientation. Additional insight into the orientation process could not be obtained by switching the electric field. Contradictory results were obtained when the orienting field was rapidly switched on after aniline was ionised under (nearly) field-free conditions. The desolvation mechanism of ions from the droplet, which is still not completely understood nowadays, is known to be droplet size dependent. The polarisation difference ratios however did not show any droplet size dependence indicating that if the desolvation process were to affect the polarisation difference ratio, it would do so in the same way for all droplet sizes. The fact that orientation of neutral aniline was achieved even though the bands were saturated made us confident to discard the saturation of the band as a possible reason for the low degree of orientation of the ions. The laser fluence measurements did not show different polarisation difference ratios for levels of saturation similar to the ones at which the measurements on neutrals were performed. For all experimental conditions, the widths of the bands were broader than those calculated. Experiments for the scissoring overtone vibration, which has a narrower width, could not be performed due to insufficient signal. Therefore the process responsible of this broadening could not be discarded to affect the formation of pendular states. All these conditions examined, the measured degree of orientation seems unalterable. To complete these studies one should look at another molecule that presents narrow bandwidths and complete the experiments switching the electric field. In an attempt to take this a step further, one could consider performing another experiment to probe the measured orientation. Orientation of neutrals in helium droplets has been examined by Coulomb explosion. Therefore, one could Coulomb explode the ion in the cryogenic matrix to examine by VMI if the product orientation corresponds to the measured degree of orientation or indicates a higher degree, as would be expected. It is worth mentioning that in all cases, full orientation could not be achieved in the maximum electric field achievable in our setup and that higher fields or more polar molecules would be needed to ultimately consider pure orientation experiments. We hope that the limitations encountered in our experiments serve to help future investigators to pursue orientation of molecular ions.

Our results of solvation complexes have shown that formation upon alkali photoionisation can lead to both bare ionic complexes and embedded species depending on the ionisation method and droplet size conditions. After direct ionisation, the sodium atom becomes solvated and forms the $\text{Na}(\text{OH}_2)_n^+$ complex with the embedded water molecules. For this to happen, the energy generated by formation of the complex as it adds water ligands must not be enough to completely evaporate the helium environment, something which is likely for smaller droplets. After (1+1)-REMPI, bare ionic complexes are observed. When excited, the sodium tends to dissociate from the droplet and attracts the water molecules with it as it leaves the droplet. The formation of heavy complexes under these circumstances is less likely to happen. The excitation spectra of $\text{Na}(\text{OH}_2)^+$ showed some features corresponding to the atom's Rydberg transitions which indeed indicated that excitation of the metal occurs prior to complex formation. Spectra of sodium dimer suggested once more the formation of triplet-state dimers in helium droplets over the single-state dimer. The kinetic energies of the desorbed $\text{Na}(\text{OH}_2)_n^+$ give smaller values for larger complexes regardless of the ionisation method. A possible explanation for this is that, when the complexes form in the droplets, a larger interaction with the solvation layer is expected in the case of bigger molecules leading to more energy dissipation. Also, the generated energy is distributed among the more numerous vibrational modes of larger complexes. Vibrational excitation of $\text{Na}(\text{OH}_2)^+$ after ionisation permitted estimation of the size of the helium clusters hosting the ionic complex and led to desolvation of bare ionic complexes and smaller size clusters of helium atoms with the complex. From the rovibrational spectrum we could confirm that the helium environment contributes to the moment of inertia of light ionic rotors since the spacing of the asymmetric subbands, compared to the gas-phase spectra, revealed a distortion on the energy levels. However, due to the limited number of energy levels populated in the cold helium environment it is not possible to deduce to what extent the various energy levels are affected by the interaction with the helium.

7 REFERENCES

- [1] S. Grebenev, J. P. Toennies, A. F. Vilesov, *Science* **1998**, *279*, 2083-2086.
- [2] M. V. Patel, A. Viel, F. Paesani, P. Huang, K. B. Whaley, *The Journal of Chemical Physics* **2003**, *118*, 5011-5027.
- [3] H. Kamerlingh Onnes, *The liquefaction of helium. Communication no. 108 from the Physical Laboratory at Leiden*, Amsterdam, **1908**.
- [4] J. Wilks, *The properties of liquid and solid helium*, Clarendon Press, Oxford, **1967**.
- [5] J. P. Toennies, A. F. Vilesov, *Annual Review of Physical Chemistry* **1998**, *49*, 1-41.
- [6] A. Scheidemann, J. P. Toennies, J. A. Northby, *Physical Review Letters* **1990**, *64*, 1899-1902.
- [7] F. Ancilotto, P. B. Lerner, M. W. Cole, *Journal of Low Temperature Physics* **1995**, *101*, 1123-1146.
- [8] M. Hartmann, R. E. Miller, J. P. Toennies, A. Vilesov, *Physical Review Letters* **1995**, *75*, 1566-1569.
- [9] M. Hartmann, R. E. Miller, J. P. Toennies, A. F. Vilesov, *Science* **1996**, *272*, 1631-1634.
- [10] M. Joppien, R. Karnbach, T. Möller, *Physical Review Letters* **1993**, *71*, 2654-2657.
- [11] R. J. Donnelly, *Quantized vortices in helium II, Vol. 2*, Cambridge University Press, **1991**.
- [12] L. F. Gomez, E. Loginov, A. F. Vilesov, *Physical Review Letters* **2012**, *108*, 155302.
- [13] H. Buchenau, J. P. Toennies, J. A. Northby, *The Journal of Chemical Physics* **1991**, *95*, 8134-8148.
- [14] S. Smolarek, N. B. Brauer, W. J. Buma, M. Drabbels, *Journal of the American Chemical Society* **2010**, *132*, 14086-14091.
- [15] N. B. Brauer, S. Smolarek, X. Zhang, W. J. Buma, M. Drabbels, *The Journal of Physical Chemistry Letters* **2011**, *2*, 1563-1566.
- [16] X. Zhang, N. B. Brauer, G. Berden, A. M. Rijs, M. Drabbels, *The Journal of Chemical Physics* **2012**, *136*, 044305.
- [17] X. Zhang, M. Drabbels, *The Journal of Chemical Physics* **2012**, *137*, 051102.
- [18] P. Bartl, C. Leidlmair, S. Denifl, P. Scheier, O. Echt, *The Journal of Physical Chemistry A* **2014**, *118*, 8050-8059.
- [19] Q. Liu, J.-K. Wang, A. H. Zewail, *Nature* **1993**, *364*, 427-430.

- [20] K. Nauta, R. E. Miller, *Science* **1999**, *283*, 1895-1897.
- [21] K. Nauta, R. E. Miller, *Science* **2000**, *287*, 293-295.
- [22] J. Küpper, J. M. Merritt, *International Reviews in Physical Chemistry* **2007**, *26*, 249-287.
- [23] E. Loginov, L. F. Gomez, A. F. Vilesov, *The Journal of Physical Chemistry A* **2011**, *115*, 7199-7204.
- [24] E. Latimer, D. Spence, C. Feng, A. Boatwright, A. M. Ellis, S. Yang, *Nano Letters* **2014**, *14*, 2902-2906.
- [25] V. Mozhayskiy, M. N. Slipchenko, V. K. Adamchuk, A. F. Vilesov, *The Journal of Chemical Physics* **2007**, *127*, 094701.
- [26] S. A. Krasnokutski, G. Rouillé, C. Jäger, F. Huisken, S. Zhukovska, T. Henning, *The Astrophysical Journal* **2014**, *782*, 15.
- [27] F. Bierau, P. Kupser, G. Meijer, G. von Helden, *Physical Review Letters* **2010**, *105*, 133402.
- [28] K. Nauta, D. T. Moore, R. E. Miller, *Faraday Discussions* **1999**, *113*, 261-278.
- [29] J. J. Larsen, K. Hald, N. Bjerre, H. Stapelfeldt, T. Seideman, *Physical Review Letters* **2000**, *85*, 2470-2473.
- [30] C. Callegari, K. K. Lehmann, R. Schmied, G. Scoles, *The Journal of Chemical Physics* **2001**, *115*, 10090-10110.
- [31] F. Stienkemeier, K. K. Lehmann, *Journal of Physics B: Atomic, Molecular and Optical Physics* **2006**, *39*, R127.
- [32] A. Slenczka, J. P. Toennies, in *Low Temperatures and Cold Molecules*, **2006**, pp. 345-392.
- [33] T. Döppner, T. Diederich, A. Przystawik, N. X. Truong, T. Fennel, J. Tiggesbäumker, K. H. Meiwes-Broer, *Physical Chemistry Chemical Physics* **2007**, *9*, 4639-4652.
- [34] A. C. LaForge, M. Drabbels, N. B. Brauer, M. Coreno, M. Devetta, M. Di Fraia, P. Finetti, C. Grazioli, R. Katzy, V. Lyamayev, T. Mazza, M. Mudrich, P. O'Keeffe, Y. Ovcharenko, P. Piseri, O. Plekan, K. C. Prince, R. Richter, S. Stranges, C. Callegari, T. Möller, F. Stienkemeier, *Scientific Reports* **2014**, *4*, 3621.
- [35] M. Mudrich, F. Stienkemeier, *International Reviews in Physical Chemistry* **2014**, *33*, 301-339.
- [36] M. P. Ziemkiewicz, D. M. Neumark, O. Gessner, *International Reviews in Physical Chemistry* **2015**, *34*, 239-267.
- [37] F. Dalfovo, S. Stringari, *The Journal of Chemical Physics* **2001**, *115*, 10078-10089.
- [38] M. Barranco, R. Guardiola, S. Hernández, R. Mayol, J. Navarro, M. Pi, *Journal of Low Temperature Physics* **2006**, *142*, 1.

- [39] K. Szalewicz, *International Reviews in Physical Chemistry* **2008**, *27*, 273-316.
- [40] S. Yang, A. M. Ellis, *Chemical Society Reviews* **2013**, *42*, 472-484.
- [41] S. Goyal, D. L. Schutt, G. Scoles, *Physical Review Letters* **1992**, *69*, 933-936.
- [42] S. Goyal, D. L. Schutt, G. Scoles, *Physical Review Letters* **1994**, *73*, 2512-2512.
- [43] M. Hartmann, F. Mielke, J. P. Toennies, A. F. Vilesov, G. Benedek, *Physical Review Letters* **1996**, *76*, 4560-4563.
- [44] Y. Kwon, P. Huang, M. V. Patel, D. Blume, K. B. Whaley, *The Journal of Chemical Physics* **2000**, *113*, 6469-6501.
- [45] Y. Kwon, K. Birgitta Whaley, *Physical Review Letters* **1999**, *83*, 4108-4111.
- [46] C. Callegari, A. Conjusteau, I. Reinhard, K. K. Lehmann, G. Scoles, F. Dalfovo, *Physical Review Letters* **1999**, *83*, 5058-5061.
- [47] C. Callegari, A. Conjusteau, I. Reinhard, K. K. Lehmann, G. Scoles, F. Dalfovo, *Physical Review Letters* **2000**, *84*, 1848-1848.
- [48] D. Blume, M. Mladenović, M. Lewerenz, K. B. Whaley, *The Journal of Chemical Physics* **1999**, *110*, 5789-5805.
- [49] E. Lee, D. Farrelly, K. B. Whaley, *Physical Review Letters* **1999**, *83*, 3812-3815.
- [50] J. Tang, Y. Xu, A. R. W. McKellar, W. Jäger, *Science* **2002**, *297*, 2030-2033.
- [51] J. Tang, A. R. W. McKellar, *The Journal of Chemical Physics* **2003**, *119*, 5467-5477.
- [52] Y. Xu, W. Jäger, J. Tang, A. R. W. McKellar, *Physical Review Letters* **2003**, *91*, 163401.
- [53] J. Tang, A. R. W. McKellar, F. Mezzacapo, S. Moroni, *Physical Review Letters* **2004**, *92*, 145503.
- [54] N. B. Brauer, EPFL **2013**.
- [55] E. Mucha, M. Marianski, F.-F. Xu, D. A. Thomas, G. Meijer, G. von Helden, P. H. Seeberger, K. Pagel, *Nature Communications* **2018**, *9*, 4174.
- [56] F. Filsinger, D.-S. Ahn, G. Meijer, G. von Helden, *Physical Chemistry Chemical Physics* **2012**, *14*, 13370-13377.
- [57] X. Zhang, M. Drabbels, *The Journal of Physical Chemistry Letters* **2014**, *5*, 3100-3105.
- [58] A. I. González Flórez, D.-S. Ahn, S. Gewinner, W. Schöllkopf, G. von Helden, *Physical Chemistry Chemical Physics* **2015**, *17*, 21902-21911.
- [59] E. Loginov, D. Rossi, M. Drabbels, *Physical Review Letters* **2005**, *95*, 163401.

- [60] E. Loginov, EPFL **2008**.
- [61] E. Loginov, M. Drabbels, *Physical Review Letters* **2011**, *106*, 083401.
- [62] K. Nauta, R. E. Miller, *Physical Review Letters* **1999**, *82*, 4480-4483.
- [63] M. Y. Choi, F. Dong, R. E. Miller, *Philosophical Transactions of the Royal Society of London A: Mathematical, Physical and Engineering Sciences* **2005**, *363*, 393-413.
- [64] A. Braun, EPFL **2004**.
- [65] X. Zhang, EPFL **2013**.
- [66] H. Buchenau, E. L. Knuth, J. Northby, J. P. Toennies, C. Winkler, *The Journal of Chemical Physics* **1990**, *92*, 6875-6889.
- [67] M. Lewerenz, B. Schilling, J. P. Toennies, *Chemical Physics Letters* **1993**, *206*, 381-387.
- [68] E. L. Knuth, *The Journal of Chemical Physics* **1997**, *107*, 9125-9132.
- [69] S. Stringari, J. Treiner, *The Journal of Chemical Physics* **1987**, *87*, 5021-5027.
- [70] R. N. Bracewell, *The Fourier transform and its applications*, 3rd ed. ed., McGraw-Hill, Boston, **2000**.
- [71] A. Braun, M. Drabbels, *Review of Scientific Instruments* **2005**, *76*, 113103.
- [72] A. T. J. B. Eppink, D. H. Parker, *Review of Scientific Instruments* **1997**, *68*, 3477-3484.
- [73] M. J. J. Vrakking, *Review of Scientific Instruments* **2001**, *72*, 4084-4089.
- [74] U. Boesl, R. Weinkauff, E. W. Schlag, *International Journal of Mass Spectrometry and Ion Processes* **1992**, *112*, 121-166.
- [75] W. C. Wiley, I. H. McLaren, *Review of Scientific Instruments* **1955**, *26*, 1150-1157.
- [76] B. A. Mamyrin, V. I. Karataev, D. V. Shmikk, V. A. Zagulin, *Zh. Eksp. Teor. Fiz.* *64: No. 1*, 82-89. **1973**.
- [77] B. A. Mamyrin, *International Journal of Mass Spectrometry and Ion Processes* **1994**, *131*, 1-19.
- [78] N. Mirsaleh-Kohan, W. D. Robertson, R. N. Compton, *Mass Spectrometry Reviews* **2008**, *27*, 237-285.
- [79] A. Radionova, I. Filippov, P. J. Derrick, *Mass Spectrometry Reviews* **2016**, *35*, 738-757.
- [80] Behlke Power Electronics GmbH, **2019**.
- [81] R. J. Beuhler, R. B. Bernstein, K. H. Kramer, *Journal of the American Chemical Society* **1966**, *88*, 5331-5332.
- [82] K. H. Kramer, R. B. Bernstein, *The Journal of Chemical Physics* **1965**, *42*, 767-770.
- [83] P. R. Brooks, E. M. Jones, *The Journal of Chemical Physics* **1966**, *45*, 3449-3450.

- [84] R. C. Estler, R. N. Zare, *Journal of the American Chemical Society* **1978**, *100*, 1323-1324.
- [85] H. Stapelfeldt, *The European Physical Journal D - Atomic, Molecular, Optical and Plasma Physics* **2003**, *26*, 15-19.
- [86] F. Rosca-Pruna, M. J. J. Vrakking, *The Journal of Chemical Physics* **2002**, *116*, 6567-6578.
- [87] M. J. J. Vrakking, S. Stolte, *Chemical Physics Letters* **1997**, *271*, 209-215.
- [88] P. R. Brooks, *Science* **1976**, *193*, 11-16.
- [89] M. V. Johnston, *TrAC Trends in Analytical Chemistry* **1984**, *3*, 58-61.
- [90] B. Friedrich, D. R. Herschbach, *Z Phys D - Atoms, Molecules and Clusters* **1991**, *18*, 153-161.
- [91] H. J. Loesch, A. Remscheid, *The Journal of Chemical Physics* **1990**, *93*, 4779-4790.
- [92] B. Friedrich, D. R. Herschbach, *Nature* **1991**, *353*, 412-414.
- [93] K. Nauta, R. E. Miller, *The Journal of Chemical Physics* **1999**, *111*, 3426-3433.
- [94] M. Y. Choi, F. Dong, S. W. Han, R. E. Miller, *The Journal of Physical Chemistry A* **2008**, *112*, 7185-7190.
- [95] A. Min, S. J. Lee, Y. Myong, C.-S. Choi, R. E. Miller, *Bull. Korean Chem. Soc* **2009**, *30(12)*, 3039-3044.
- [96] F. Dong, R. E. Miller, *Science* **2002**, *298*, 1227-1230.
- [97] M. Y. Choi, R. E. Miller, *The Journal of Physical Chemistry A* **2007**, *111*, 2475-2479.
- [98] M. Y. Choi, R. E. Miller, *Journal of the American Chemical Society* **2006**, *128*, 7320-7328.
- [99] L. Pei, J. Zhang, C. Wu, W. Kong, *The Journal of Chemical Physics* **2006**, *125*, 024305.
- [100] L. Pei, J. Zhang, W. Kong, *The Journal of Chemical Physics* **2007**, *127*, 174308.
- [101] L. Pei, J. Zhang, W. Kong, D. Xu, H. Guo, *Chemical Physics Letters* **2008**, *462*, 173-177.
- [102] K. J. Franks, H. Li, W. Kong, *The Journal of Chemical Physics* **1999**, *110*, 11779-11788.
- [103] J. Michl, *Spectroscopy with polarized light: solute alignment by photoselection, in liquid crystals, polymers, and membranes*, VCH, Weinheim, **1986**.
- [104] S. A. Rice, A. R. Dinner, *Advances in Chemical Physics, Vol. vol. 316*, Wiley, **2011**.
- [105] R. N. Zare, *Angular momentum: understanding spatial aspects in chemistry and physics*, Wiley, New York, **1988**.

- [106] G. Henderson, B. Logsdon, *Journal of Chemical Education* **1995**, 72, 1021.
- [107] W. Kong, J. Bulthuis, *The Journal of Physical Chemistry A* **2000**, 104, 1055-1063.
- [108] P. W. Atkins, R. Friedman, *Molecular quantum mechanics*, 5th ed. ed., Oxford University Press, Oxford, **2011**.
- [109] K. Nauta, R. E. Miller, *The Journal of Chemical Physics* **2002**, 117, 4846-4852.
- [110] D. T. Moore, L. Oudejans, R. E. Miller, *The Journal of Chemical Physics* **1999**, 110, 197-208.
- [111] M. J. Frisch, G. W. Trucks, H. B. Schlegel, G. E. Scuseria, M. A. Robb, J. R. Cheeseman, G. Scalmani, V. Barone, B. Mennucci, G. A. Petersson, H. Nakatsuji, M. Caricato, X. Li, H. P. Hratchian, A. F. Izmaylov, J. Bloino, G. Zheng, J. L. Sonnenberg, M. Hada, M. Ehara, K. Toyota, R. Fukuda, J. Hasegawa, M. Ishida, T. Nakajima, Y. Honda, O. Kitao, H. Nakai, T. Vreven, J. A. Montgomery, J. E. Peralta, F. Ogliaro, M. Bearpark, J. J. Heyd, E. Brothers, K. N. Kudin, V. N. Staroverov, R. Kobayashi, J. Normand, K. Raghavachari, A. Rendell, J. C. Burant, S. S. Iyengar, J. Tomasi, M. Cossi, N. Rega, J. M. Millam, M. Klene, J. E. Knox, J. B. Cross, V. Bakken, C. Adamo, J. Jaramillo, R. Gomperts, R. E. Stratmann, O. Yazyev, A. J. Austin, R. Cammi, C. Pomelli, J. W. Ochterski, R. L. Martin, K. Morokuma, V. G. Zakrzewski, G. A. Voth, P. Salvador, J. J. Dannenberg, S. Dapprich, A. D. Daniels, Farkas, J. B. Foresman, J. V. Ortiz, J. Cioslowski, D. J. Fox, Gaussian, Inc., Wallingford CT, **2009**.
- [112] P. M. Wojciechowski, W. Zierkiewicz, D. Michalska, P. Hobza, *The Journal of Chemical Physics* **2003**, 118, 10900-10911.
- [113] T. Nakanaga, F. Ito, J. Miyawaki, K. Sugawara, H. Takeo, *Chemical Physics Letters* **1996**, 261, 414-420.
- [114] J. C. D. Brand, D. R. Williams, T. J. Cook, *Journal of Molecular Spectroscopy* **1966**, 20, 359-380.
- [115] M. Honda, A. Fujii, E. Fujimaki, T. Ebata, N. Mikami, *The Journal of Physical Chemistry A* **2003**, 107, 3678-3686.
- [116] H. Piest, G. v. Helden, G. Meijer, *The Journal of Chemical Physics* **1999**, 110, 2010-2015.
- [117] J. A. Arnaud, W. M. Hubbard, G. D. Mandeville, B. de la Clavière, E. A. Franke, J. M. Franke, *Appl. Opt.* **1971**, 10, 2775-2776.
- [118] P. Radcliffe, A. Przystawik, T. Diederich, T. Döppner, J. Tiggesbäumker, K.-H. Meiwes-Broer, *Physical Review Letters* **2004**, 92, 173403.
- [119] V. S. Letokhov, V. I. Mishin, A. A. Puretzky, *Progress in Quantum Electronics* **1977**, 5, 139-203.
- [120] S. Braslavsky, *Pure And Applied Chemistry* **2007**, 79, 293-465.

- [121] K. Kuyanov-Prozument, M. Y. Choi, A. F. Vilesov, *The Journal of Chemical Physics* **2010**, *132*, 014304.
- [122] R. Schwan, M. Kaufmann, D. Leicht, G. Schwaab, M. Havenith, *Physical Chemistry Chemical Physics* **2016**, *18*, 24063-24069.
- [123] L. Fumagalli, A. Esfandiar, R. Fabregas, S. Hu, P. Ares, A. Janardanan, Q. Yang, B. Radha, T. Taniguchi, K. Watanabe, G. Gomila, K. S. Novoselov, A. K. Geim, *Science* **2018**, *360*, 1339-1342.
- [124] C. J. Mundy, J. Hutter, M. Parrinello, *Journal of the American Chemical Society* **2000**, *122*, 4837-4838.
- [125] C. Bobbert, C. P. Schulz, *The European Physical Journal D - Atomic, Molecular, Optical and Plasma Physics* **2001**, *16*, 95-97.
- [126] C. Steinbach, U. Buck, *Physical Chemistry Chemical Physics* **2005**, *7*, 986-990.
- [127] F. Stienkemeier, J. Higgins, C. Callegari, S. I. Kanorsky, W. E. Ernst, G. Scoles, *Z Phys D - Atoms, Molecules and Clusters* **1996**, *38*, 253-263.
- [128] C. M. Lindsay, G. E. Douberly, R. E. Miller, *Journal of Molecular Structure* **2006**, *786*, 96-104.
- [129] K. E. Kuyanov, M. N. Slipchenko, A. F. Vilesov, *Chemical Physics Letters* **2006**, *427*, 5-9.
- [130] E. Lugovoj, J. P. Toennies, A. Vilesov, *The Journal of Chemical Physics* **2000**, *112*, 8217-8220.
- [131] G. E. Douberly, R. E. Miller, *The Journal of Physical Chemistry A* **2007**, *111*, 7292-7302.
- [132] S. Müller, S. Krapf, T. Koslowski, M. Mudrich, F. Stienkemeier, *Physical Review Letters* **2009**, *102*, 183401.
- [133] M. Lewerenz, B. Schilling, J. P. Toennies, *The Journal of Chemical Physics* **1995**, *102*, 8191-8207.
- [134] P. Atkins, J. de Paula, *Atkins' Physical Chemistry*, OUP Oxford, **2010**.
- [135] G. Herzberg, *Molecular Spectra and Molecular Structure: Infrared and Raman Spectra of Polyatomic Molecules, Vol. II*, Krieger Publishing Company, **1991**.
- [136] C.-C. Tsai, J. T. Bahns, W. C. Stwalley, *Chemical Physics Letters* **1995**, *236*, 553-557.
- [137] E. S. Chang, L. Jing, J. Zhang, T. Chin-Chun, J. Bahns, W. C. Stwalley, *The Journal of Chemical Physics* **1999**, *111*, 6247-6252.
- [138] J. Higgins, C. Callegari, J. Reho, F. Stienkemeier, W. E. Ernst, M. Gutowski, G. Scoles, *The Journal of Physical Chemistry A* **1998**, *102*, 4952-4965.
- [139] H. K. Chung, K. Kirby, J. F. Babb, *Physical Review A* **2001**, *63*, 032516.

- [140] A. Färbert, J. Koch, T. Platz, W. Demtröder, *Chemical Physics Letters* **1994**, *223*, 546-552.
- [141] Chemcraft, **2019**, p. graphical software for visualization of quantum chemistry computations.
- [142] T. D. Vaden, C. J. Weinheimer, J. M. Lisy, *The Journal of Chemical Physics* **2004**, *121*, 3102-3107.
- [143] A. Kramida, Y. Ralchenko, J. Reader, NIST, National Institute of Standards and Technology, **2018**.
- [144] A. Hernando, M. Barranco, M. Pi, E. Loginov, M. Langlet, M. Drabbels, *Physical Chemistry Chemical Physics* **2012**, *14*, 3996-4010.
- [145] NIST, National Institute of Standards and Technology, **2018**.
- [146] E. Loginov, M. Drabbels, *The Journal of Physical Chemistry A* **2014**, *118*, 2738-2748.
- [147] T. D. Vaden, B. Forinash, J. M. Lisy, *The Journal of Chemical Physics* **2002**, *117*, 4628-4631.
- [148] T. Shimanouchi, *Journal of Physical and Chemical Reference Data* **1977**, 1-160.
- [149] G. E. Douberly, K. Nauta, R. E. Miller, *Chemical Physics Letters* **2003**, *377*, 384-390.
- [150] D. T. Moore, R. E. Miller, *The Journal of Physical Chemistry A* **2004**, *108*, 1930-1937.
- [151] T. R. Huet, C. J. Pursell, W. C. Ho, B. M. Dinelli, T. Oka, *The Journal of Chemical Physics* **1992**, *97*, 5977-5987.
- [152] M. Y. Choi, G. E. Douberly, T. M. Falconer, W. K. Lewis, C. M. Lindsay, J. M. Merritt, P. L. Stiles, R. E. Miller, *International Reviews in Physical Chemistry* **2006**, *25*, 15-75.
- [153] SCIGRESS, Fujitsu, **2019**.
- [154] A. R. W. McKellar, *The Journal of Chemical Physics* **2007**, *127*, 044315.
- [155] F. Ancilotto, E. Cheng, M. W. Cole, F. Toigo, *Zeitschrift für Physik B Condensed Matter* **1995**, *98*, 323-329.

LIST OF ABBREVIATIONS

BBO	Beta barium borate
CCD	Charge-coupled device
DFT	Density functional theory
FWHM	Full width at half maximum
HND	Helium nanodroplet
HV	High-voltage
IE	Ionisation energy
IR	Infrared
KDP	Potassium dihydrogen phosphate
MCP	Micro-channel plate
MP2	Second-order Møller–Plesset perturbation theory
MSP	Microsphere plate
Nd:YAG	Neodymium-doped yttrium-aluminium-garnet ($\text{Nd:Y}_3\text{Al}_5\text{O}_{12}$)
OPA	Optical parametric amplifier
OPO	Optical parametric oscillator
PS	Phosphor screen
QMS	Quadrupole mass spectrometer
REMPI	Resonant-enhanced multiphoton ionisation
ROI	Region of interest
TD	Time dependent
TOF	Time of flight
UHV	Ultra-high vacuum
UV	Ultraviolet
VMI	Velocity map imaging



(Don't hesitate to cut this page off if you prefer to have it on hand)

LIST OF FIGURES

Figure 1-1. Spectra of OCS in ^3He as the average number of added ^4He atoms (N_4) is increased. The spectrum in ^3He (A) shows a broad band that results into sharp rotational features for $N \geq 60$ (E and F). ν_θ is at 2061.71 cm^{-1} . Taken from [1].....	4
Figure 1-2. Ground state wave function obtained from Monte Carlo calculations (a) of helium for a nonrotating (left) and rotating (right) SF_6 molecule projected in the molecular frame at 4.25 \AA from the molecule; (b) of $^4\text{He}_8\text{SF}_6$ projected at 8 a.u. radius when the gas phase rotational constant (B) (left) and a ten times larger B value (right) are used. In (b), the colour scale uses blue to represent high values and red for low ones. A more isotropic density is obtained for rotating SF_6 . Higher rotational constants result in an even more isotropic density. Reprinted from (a) [44], (b) [49].	6
Figure 2-1. Illustration of the main components of the experimental setup. The blue dots show the trajectory of the helium droplet beam. The red lines show the ion trajectories in the time-of-flight mass spectrometers.....	13
Figure 3-1. Left: Initial distribution of the ions produced by the laser in a field (HV) and in terms of temporal (t), spatial (x) and velocity (v) distributions factors contributing to an initial distribution. Right: Illustration explaining (first order) space focus. At time zero the ions are spread and start moving by the field. The distance from these positions to the ground electrode is x_A . At some point, called the space focus x_{SF} , the faster ions overtake the slower ones ($x_{SF} = 2x_A$). The simultaneity is lost after the space focus. Taken from [74].....	21
Figure 3-2. Schematic representation of the reflectron time-of-flight apparatus showing its different components. Ions with different kinetic energies would follow different trajectories (dashed lines) in the ion mirror; for greater kinetic energies they arrive faster to the ion mirror but penetrate deeper (in green) into the field traveling a longer flight path and resulting in similar total flight times.....	21
Figure 3-3. SOLIDWORKS side view of the built reflectron time-of-flight mass spectrometer viewed from the helium nozzle to the quadrupole mass spectrometer of the machine. The design allows linear and reflectron TOF configurations. The ion trajectories for each are shown in red and blue dashed lines respectively.....	23
Figure 3-4. SOLIDWORKS side view of the ion source.	24
Figure 3-5. Simulated trajectories of ions of 200 uma at $60 \text{ kV} \cdot \text{cm}^{-1}$ in the reflectron TOF with an initial velocity in the molecular beam direction in a dual-stage type ion source. The blue and red dashed lines represent the molecular beam and laser beam respectively. Top: viewed from the molecular beam to the quadrupole mass spectrometer of the machine. Bottom: viewed in the direction of the laser, perpendicular to the molecular beam.	26

- Figure 3-6. Simulated trajectories of aniline ions at $60 \text{ kV} \cdot \text{cm}^{-1}$ in the reflectron TOF with an initial velocity in the molecular beam direction in a single-stage type ion source. The blue and red dashed lines represent the molecular beam and laser beam respectively. Top: viewed from the molecular beam to the quadrupole mass spectrometer of the machine. Bottom: viewed in the direction of the laser, perpendicular to the molecular beam..... 27
- Figure 3-7. Circuits of the two operational modes of the HV-switch. Left: scheme employed for switching between positive voltages. Right: Employed for negative-positive fields. R_S : series resistors, C_B : capacitor, A: switching off-state path, B: switching on-state path. Taken from BEHLKE^[80]..... 29
- Figure 3-8. Measured voltage output (in green) on an oscilloscope from an initial voltage of zero switched to 30 kV generated by the installed HV-switch. A 1000:1 probe is employed to measure it. Each horizontal division corresponds to $1 \mu\text{s}$ and every vertical to 1 kV. The rise time is on the order of 100 ns and the pulse length is $5 \mu\text{s}$ 30
- Figure 4-1. Left: Coordinate system illustrating the laboratory frame (X, Y, Z) and the molecular frame (x, y, z). In the molecular frame, the permanent dipole, μ_p , is chosen to be the z axis and the transition dipole, μ_t , is set to be within the x-z plane. θ is the angle between the laboratory frame and the molecular frame, ϕ is the projection of this angle on the X-Y plane and, α is the angle between the permanent dipole moment and the transition dipole moment. Right: when the electric field is applied the permanent dipole moment orients in its direction ($\Theta = 0$). Reprinted and adapted with permission from ^[102]..... 34
- Figure 4-2. Effect of an electric field on the transition intensity as a function of the laser polarisation direction. The solid line represents the spectra at zero field. μ_p is the permanent dipole moment, μ_t is the transition dipole moment and α the angle between them. Reprinted with permission from ^[63]..... 35
- Figure 4-3. Left: Motion of a two-particle rigid rotor. Right: Stark pendulum, the dipole moment of the molecule (μ_p) is trapped by the applied electric field (ϵ) in a libration motion. Adapted from reference ^[106]..... 36
- Figure 4-4. Calculated splitting and shifting of the energy levels when the dipole of aniline cation interacts with an electric field ($J = 20$, $m = 1$). The rotational constants are divided by nine. Right: Enlarged y axis to observe the splitting in detail..... 37
- Figure 4-5. Calculated spectra of the H-F stretch in acetylene-HF (parallel to the permanent dipole moment) from 0 to $160 \text{ kV} \cdot \text{cm}^{-1}$ resulting for (left) parallel (right) perpendicular laser polarisation..... 38
- Figure 4-6. Excitation spectra ($S_1 \leftarrow S_0$ (1+1)-REMPI) of aniline in the gas phase (top) and in helium droplets (bottom) for a droplet size of 41 \AA . Taken from ^[59]..... 40
- Figure 4-7. (a) Structure of aniline in the ground state showing the molecular frame axes (in green) and the permanent dipole moment direction (in blue). (c) Structure of aniline in the S_1 state showing the molecular frame axes (in green) and the permanent

dipole moment direction (in blue). Right: direction of the displacement vectors (in orange) contributing to the antisymmetric (b) and symmetric (d) transition dipole moments.	41
Figure 4-8. Structure of aniline cation showing the molecular frame axes (in green) and permanent dipole moment direction (in blue).	42
Figure 4-9. IR spectrum of aniline cation in helium droplets showing the scissoring overtone ($2\delta_{\text{scis}}\text{NH}_2$) at 3270.6 cm^{-1} , the symmetric NH_2 -stretch vibration ($\nu_{\text{sym}}\text{NH}_2$) at 3395.1 cm^{-1} and the antisymmetric NH_2 -stretch vibration ($\nu_{\text{asym}}\text{NH}_2$) at 3488.8 cm^{-1} . Data taken from ^[54]	43
Figure 4-10. Conceptual scheme of the levels of the states populated: electronic (left) and vibrational (right) transitions of neutral molecules.	45
Figure 4-11. Scheme of ionisation methods and excitation: two-photon non-resonant ionisation (left), $(1 + 1)$ -resonance-enhanced multiphoton ionisation via the band origin 000 (middle) and the 1201 vibronic band (right) of the $S_1 \leftarrow S_0$ transition...	46
Figure 4-12. Dependence of the ion yield of aniline on the UV laser polarisation at different field strengths.	47
Figure 4-13. Effect of the applied electric field on the ion yield generated after electronic excitation of aniline (expressed as the difference ratios of the averaged intensity from each laser polarisation).	47
Figure 4-14. Effect of the applied electric field on the ion yield generated after electronic excitation of aniline (expressed as the ratio of the averaged intensity from each laser polarisation) and comparison with simulated values at standard helium nanodroplet conditions (expressed as the ratio of the transition peak areas from each laser polarisation).	48
Figure 4-15. Left: Antisymmetric NH_2 -stretch vibrational band of aniline in helium nanodroplets when the laser polarisation direction is parallel and perpendicular in a $15\text{ kV} \cdot \text{cm}^{-1}$ static electric field. Right: Effect of the applied electric field on the symmetric (in blue, $\nu_{\text{sym}}\text{NH}_2$ at 3422 cm^{-1}) and antisymmetric (in green, $\nu_{\text{asym}}\text{NH}_2$ at 3509 cm^{-1}) stretch transition intensity for neutral aniline (expressed as the difference ratios of the peak areas from each laser polarisation).	49
Figure 4-16. Effect of the applied electric field on the symmetric (solid line in blue, $\nu_{\text{sym}}\text{NH}_2$ at 3422 cm^{-1}) and antisymmetric (solid line in green, $\nu_{\text{asym}}\text{NH}_2$ at 3509 cm^{-1}) stretch transition intensity for neutral aniline and comparison with simulated values (dashed lines) at standard helium nanodroplet conditions both expressed as the difference ratios of the peak areas from each laser polarisation.	50
Figure 4-17. Left: Symmetric NH_2 -stretch vibrational band of non-resonantly generated aniline cations in helium nanodroplets when the laser polarisation direction is parallel and perpendicular in a $60\text{ kV} \cdot \text{cm}^{-1}$ static electric field. Right: Effect of the IR polarisation on the symmetric stretch transition intensity for non-resonantly ionised	

aniline for different field strengths (expressed as the difference ratio of the peak areas from each laser polarisation).....	52
Figure 4-18. Antisymmetric (left) and symmetric (right) NH_2 -stretch vibrational bands of aniline cations generated by resonant ionisation via the $S_1 \leftarrow S_0$ band origin at 34100 cm^{-1} in helium nanodroplets when the laser polarisation direction is parallel and perpendicular in a $60 \text{ kV} \cdot \text{cm}^{-1}$ static electric field.....	53
Figure 4-19. Effect of the IR polarisation on the symmetric ($\nu_{\text{sym}}\text{NH}_2$ at 3395 cm^{-1}) and antisymmetric ($\nu_{\text{asym}}\text{NH}_2$ at 3488 cm^{-1}) stretch transition intensity for cationic aniline (expressed as the difference ratios of the peak areas from each laser polarisation) as a function of the applied electric field. Left: resonant ionisation via the band origin 000 of the $S_1 \leftarrow S_0$ transition origin at 34100 cm^{-1} . Right: resonant ionisation via the 1201 vibronic band at 34900 cm^{-1} of the $S_1 \leftarrow S_0$ transition.	54
Figure 4-20. Effect of the IR polarisation on the symmetric ($\nu_{\text{sym}}\text{NH}_2$ at 3395 cm^{-1}) and antisymmetric ($\nu_{\text{asym}}\text{NH}_2$ at 3488 cm^{-1}) stretch transition intensity for cationic aniline ionised in three different ways (expressed as the difference ratios of the peak areas from each laser polarisation) as a function of the applied electric field. $E_i = 37594 \text{ cm}^{-1}$ non-resonant ionisation, $E_i = 34100 \text{ cm}^{-1}$ resonant ionisation via the $S_1 \leftarrow S_0$ band origin, $E_i = 34900 \text{ cm}^{-1}$ resonant ionisation via the 1201 vibronic band of the $S_1 \leftarrow S_0$ transition.....	55
Figure 4-21. Left: Effect of the applied electric field on the symmetric (in blue) and antisymmetric (in green) stretch vibrational transition intensity (expressed as the difference ratios of the peak areas from each laser polarisation) and comparison with simulated values at standard helium nanodroplet conditions for ions (dashed lines). Right: Simulated effect of the electric field on the symmetric stretch transition area of aniline ions resulting for different temperatures and rotational constants.....	57
Figure 4-22. Effect of the IR polarisation on the symmetric (open circle, $\nu_{\text{sym}}\text{NH}_2$ at 3395 cm^{-1}) and antisymmetric (solid circle, $\nu_{\text{asym}}\text{NH}_2$ at 3488 cm^{-1}) stretch transition intensity for cationic aniline for several UV polarisations (expressed as the difference ratios of the peak areas from each laser polarisation). α is the angle between the UV laser polarisation direction and the field direction. The values are taken in a $10 \text{ kV} \cdot \text{cm}^{-1}$ and $60 \text{ kV} \cdot \text{cm}^{-1}$ electric field. Data points at the same field strength are horizontally displaced from each other for clarity.....	58
Figure 4-23. Scheme showing the relative delays of pump, probe and high-voltage switch. Left: normal switch working conditions with an initial zero or negative voltage. Right: voltage switches 200 ns before the UV pulse to imitate static field conditions.....	59
Figure 4-24. Left: Effect of a $60 \text{ kV} \cdot \text{cm}^{-1}$ pulsed electric field on the symmetric stretch vibrational transition of ionic aniline after non-resonant ionisation. Right: Effect of a $60 \text{ kV} \cdot \text{cm}^{-1}$ pulsed electric field with $-2 \text{ kV} \cdot \text{cm}^{-1}$ initial field.....	60
Figure 4-25. Effect of a $60 \text{ kV} \cdot \text{cm}^{-1}$ pulsed electric field on the difference ratios of the peak areas from each IR laser polarisation on the symmetric ($\nu_{\text{sym}}\text{NH}_2$ at 3395 cm^{-1}) and	

- antisymmetric ($\nu_{\text{asym}}\text{NH}_2$ at 3488 cm^{-1}) stretch vibrations of aniline cations generated by resonant ionisation via the $S_1 \leftarrow S_0$ band origin at 34100 cm^{-1} . (a) The positive voltage is applied before the UV pulse, as if no switch. (b) The polarisation of the UV light is vertical (rest done for horizontal). The strength of the field is $60\text{ kV} \cdot \text{cm}^{-1}$ for all measurements; separated for readability. 61
- Figure 4-26. Effect of the droplet size on the antisymmetric ($\nu_{\text{asym}}\text{NH}_2$ at 3488 cm^{-1}) stretch transition intensity for ionic aniline (expressed as the difference ratios of the peak areas from perpendicular IR laser polarisations) in a $60\text{ kV} \cdot \text{cm}^{-1}$ field. 62
- Figure 4-27. Effect of the IR laser fluence on the symmetric stretch ($\nu_{\text{sym}}\text{NH}_2$ at 3395 cm^{-1}) for aniline cation (expressed as the difference ratios of the peak areas from each laser polarisation) in a $60\text{ kV} \cdot \text{cm}^{-1}$ field. 63
- Figure 4-28. Effect of the IR polarisation on the symmetric ($\nu_{\text{sym}}\text{NH}_2$ at 3395 cm^{-1}) stretch transition intensity for cationic aniline as a function of the applied electric field when the IR laser power is decreased by a factor of three after resonant ionisation via the $S_1 \leftarrow S_0$ band origin at 34100 cm^{-1} and comparison with full laser power for all ionisation schemes expressed as polarisation difference ratios. 63
- Figure 4-29. Widths of the antisymmetric (a, b) and symmetric (c, d, e) vibrational stretch of the amino group with increasing electric field obtained after non-resonant ($E_i = 37594\text{ cm}^{-1}$; c), resonant via the 1201 vibronic band of the $S_1 \leftarrow S_0$ transition ($E_i = 34900\text{ cm}^{-1}$; a, d) and resonant via the $S_1 \leftarrow S_0$ band origin ($E_i = 34100\text{ cm}^{-1}$; b, e) ionisation of aniline. *) Value obtained previously in the group^[14]. 66
- Figure 4-30. Simulated spectra of the symmetric stretch ($\nu_{\text{sym}}\text{NH}_2$ at 3395 cm^{-1}) of cationic aniline under field free (left) and for parallel (blue) and perpendicular (black) laser polarisations to the electric field at $60\text{ kV} \cdot \text{cm}^{-1}$ (right). The bottom figures, (c) and (d), are obtained when the transitions are convoluted with a Gaussian distribution having a FWHM of the laser bandwidth. 67
- Figure 4-31. Left: Effect of the applied electric field on the ion yield generated after electronic excitation of aniline (expressed as the ratio of the averaged intensity from each laser polarisation) and comparison with simulated values at standard helium nanodroplet conditions (expressed as the ratio of the transition peak areas from each laser polarisation). Right: Effect of the applied electric field on the symmetric (solid line in blue, $\nu_{\text{sym}}\text{NH}_2$ at 3422 cm^{-1}) and antisymmetric (solid line in green, $\nu_{\text{asym}}\text{NH}_2$ at 3509 cm^{-1}) stretch transition intensity for neutral aniline and comparison with simulated values (dashed lines) at standard helium nanodroplet conditions both expressed as the difference ratios of the peak areas from each laser polarisation. 70
- Figure 4-32. Effect of the IR polarisation on the symmetric ($\nu_{\text{sym}}\text{NH}_2$ at 3395 cm^{-1} , left) and antisymmetric ($\nu_{\text{asym}}\text{NH}_2$ at 3488 cm^{-1} , right) stretch transition intensity for cationic aniline ionised in three different ways (expressed as the difference ratios of the peak areas from each laser polarisation) as a function of the applied electric field and comparison with simulated values at standard helium nanodroplet conditions for ions

(dashed lines). $E_i = 37594 \text{ cm}^{-1}$ non-resonant ionisation, $E_i = 34100 \text{ cm}^{-1}$ resonant ionisation via the $S_1 \leftarrow S_0$ band origin, $E_i = 34900 \text{ cm}^{-1}$ resonant ionisation via the 1201 vibronic band of the $S_1 \leftarrow S_0$ transition.....	71
Figure 5-1. Scheme showing the formation of enriched triplet-state dimers on helium droplets compared to singlet. The higher binding energy of the singlet leads to small clusters evaporation or dissociation of the molecule. Reprinted with permission from [138]. Copyright (2019) American Chemical Society.....	80
Figure 5-2. Optimised geometry of $\text{Na}(\text{OH}_2)^+$ indicating the bond lengths calculated with Gaussian 09 (MP2-AUG-cc-pVTZ) and plotted with Chemcraft ^[141]	81
Figure 5-3. Excitation spectra of Na and water doped helium droplets detecting Na^+ (in black) and $\text{Na}(\text{OH}_2)^+$ (in blue) in the Rydberg states region of sodium up to the ionisation energy. The oven temperature is 100 °C and the nozzle temperature is 18 K (top) and 13 K (bottom).	83
Figure 5-4. Mass-selected spectra of Na^+ , Na_2^+ (with and without water doping) and of $\text{Na}(\text{OH}_2)^+$. The nozzle temperature is 13 K and several oven temperatures are examined (100, 110 and 120 °C).....	85
Figure 5-5. Excitation spectra of Na and water doped helium droplets detecting $\text{Na}(\text{OH}_2)_n^+$ ($n = 1-7$) at nozzle temperatures of 13 K (a), 15 K (b), 17 K (c), and 19 K (d). The oven temperature is set to 100 °C. The dashed lines correspond to the baseline of every measurement. The solid lines are the averaged values from 41000 to 41150 and from 41300 to 41800 cm^{-1} to facilitate perceiving the intensity below and above 41300 cm^{-1}	86
Figure 5-6. Ionic complexes ($\text{Na}(\text{OH}_2)^+$ and $\text{Na}(\text{OH}_2)_6^+$) formation scheme for helium droplets of $\sim 39 \text{ \AA}$ radius: A. ‘Desorbed’: (1+1)-REMPI of sodium leads to complex dissociation outside the helium droplet. When excited, the sodium already starts to dissociate from the droplet (illustrated by the arrow) attracting a molecule of water with it and leaving the droplet as it is ionised. B. ‘Solvated’: After direct ionisation, ionic sodium solvates forming the ionic complex. C. ‘Desorbed’: $\text{Na}(\text{OH}_2)_6^+$ is not observed after (1+1)-REMPI of sodium. Most likely the formation of such large complexes upon excitation of sodium is not efficient. D. ‘Evaporated’: Direct ionisation of sodium. The bare ionic complex is detected; the energy released by the formation leads to complete helium evaporation.....	88
Figure 5-7. Velocity map images of Na^+ below IE, Na^+ above IE at 19 K of nozzle temperature, and $\text{Na}(\text{OH}_2)_7^+$ above IE at 13 K. Each image shows a 300 x 300 pixel frame around the centre. $V_r = 2000 \text{ V}$	90
Figure 5-8. Speed distributions for Na^+ and $\text{Na}(\text{OH}_2)_n^+$ complex series ($n = [1, 7]$) at 13, 15 and 17 K nozzle temperature and 100, 110 and 120 °C oven temperature respectively.	91
Figure 5-9. Average kinetic energies of different species (Na^+ and $\text{Na}(\text{OH}_2)_{1-7}^+$) below and above IE (40984 and 41408 cm^{-1} respectively) for 13, 16 and 19 K and 100, 110 and	

120 °C nozzle and oven temperatures respectively. Left: The values are plotted as a function of the laser energy. Data points at the same energy for different helium droplet sizes are horizontally displaced from each other for clarity. Right: The kinetic energies are plotted as a function of the number of complexed water ligands below (in black) and above (in red) sodium's ionisation energy.	92
Figure 5-10. Rovibrational spectrum of $\text{Na}(\text{OH}_2)^+$ at the symmetric and asymmetric OH_2 -stretch region. The temperature of the nozzle is 18 K and the oven temperature is 100 °C. All peaks are Gaussian-fitted.	94
Figure 5-11. Experimental spectrum of $\text{Cs}^+(\text{OH}_2)\text{Ar}$ showing the vibrational bands and subbands. Adapted from ^[147]	95
Figure 5-12. Optimised geometry of $\text{Na}^+\text{-He-OH}_2$ pointing out how the sodium ion is attracted by the lone pairs of oxygen and tends to sit in between water and helium. Plotted with SCIGRESS ^[153]	99
Figure 5-13. Rotational constant's dependence on $\text{Na}^+\text{-O}$ bond length and energy required. The values are obtained with Gaussian (MP2-AUG-cc-pVTZ) fixing the distance before performing the calculations.	100
Figure 5-14. Calculated Poisson distributions for $\text{Na}(\text{OH}_2)^+$ after single, double and triple pick-up neglecting evaporative cooling loss of helium. Pressure dependence of the mass-selected $\text{Na}(\text{OH}_2)^+$ signal after excitation at 3641.25 cm^{-1} (scattered).	102
Figure 5-15. TOF mass spectra. Top: from 0 to 100 amu showing a rise at 41 uma after IR-excitation caused by desolvation of $\text{Na}(\text{OH}_2)^+$ from the droplet. The inset points out all the smaller clusters formed as a result of the excitation: $\text{Na}(\text{OH}_2)^+\text{-He}_p$ ($p = 1\text{-}9$). Bottom: the vertical arrows in the 85 to 400 uma region of the spectrum show a depletion, indication of dissociation from the hosting droplets. The solid lines show the 2 amu shift between the Na-He_r and $\text{Na}(\text{OH}_2)^+\text{-He}_p$ products of single and double pick-up confirming that the depleted series corresponds to ($p = 12\text{-}71$) clusters.	103
Figure 5-16. Left: Velocity map images of $\text{Na}(\text{OH}_2)^+$ after IR excitation. The image shows a 200×200 pixel frame around the centre. $V_r = 2000$. Right: Speed distribution of $\text{Na}(\text{OH}_2)^+$ escaping of the droplets after IR-excitation obtained from the velocity map image after subtraction of the background signal caused by the ionisation light. ...	104
Figure 5-17. Ionic complex formation and desolvation scheme: (1) after the first pick-up, the sodium sits at the helium surface with a consequent number of evaporated helium atoms, (2) the water molecule gets solvated in the droplet remaining close to the edge due to a charge density interaction with the sodium atom; more helium atoms evaporate due to the pick-up process diminishing the droplet size, (3) the pump pulse is sent to ionise the sodium atom, (4) after ionisation, the size of the droplet decreases to tens of atoms [12-71] due to evaporation; the sodium gets solvated due to density interaction with the medium, (5) the probe pulse at the energy of the asymmetric and symmetric OH_2 -stretch vibration leads to (a) bare ionic complexes and (b) smaller size clusters of [1-9] helium atoms with the complex.	107

LIST OF TABLES

Table 2-1. Mean number of helium atoms per droplet ($\langle N \rangle$) and droplet radius ($\langle r \rangle$, [Å]) at different nozzle temperatures (T , [K]).....	15
Table 3-1. Input parameters used to simulate the ion trajectories in SIMION®. The y, z, x axes are defined in the direction of the laser beam, the molecular beam, and perpendicular to them respectively.....	25
Table 3-2. Optimum calculated voltages for dual-stage ion source operation of the designed reflectron time-of-flight spectrometer for a 5 kV repeller voltage.	25
Table 3-3. Optimum calculated voltages (for a 60 kV · cm ⁻¹ electric field) to perform pendular state spectroscopy using the designed reflectron time-of-flight spectrometer.	27
Table 3-4. Optimum experimental voltages (for a 60 kV · cm ⁻¹ electric field) to perform pendular state spectroscopy using the designed reflectron time-of-flight spectrometer.	28
Table 4-1. Calculated values of rotational constants [cm ⁻¹] and permanent dipole moments [D] of aniline by DFT and TD-DFT using B3lyp functional and a 6-311++G(df,pd) basis set in Gaussian.....	39
Table 4-2. Vibrational wavenumbers (ν [cm ⁻¹]) and molecular absorption coefficients (a [km · mol ⁻¹]) for both the symmetric and antisymmetric stretch of aniline.	40
Table 4-3. Calculated values of rotational constants [cm ⁻¹] and permanent dipole moment [D] of ionic aniline by DFT using B3lyp functional and a 6-311++G(df,pd) basis set in Gaussian.	41
Table 4-4. Vibrational wavenumbers (ν [cm ⁻¹]) and molecular absorption coefficients (a [km · mol ⁻¹]) for both the symmetric and antisymmetric stretch of aniline cation. ...	42
Table 4-5. Values and standard errors of slopes and intercepts and Pearson correlation coefficients obtained of the linear fits of the polarisation difference ratios obtained for different vibrational transitions of molecules ionised in the three different ways.	55
Table 4-6. Integrated molar absorption coefficients (a) for aniline and its radical cation for both the symmetric and antisymmetric stretch [km · mol ⁻¹]. Calculated values of absorption cross-sections (σ [cm ²]). The error comprises the different values of $\Delta u_{1/2}$ (FWHM) at different field strengths ranging from 2.0 to 2.4 cm ⁻¹ [cm ²]. Energy densities needed to meet the saturation condition [mJ · cm ²].....	64
Table 5-1. Calculated energies [cm ⁻¹] of the symmetric (u_{sym}) and asymmetric (u_{asym}) OH ₂ -stretching modes and rotational constants A , B and C [cm ⁻¹] of the Na(OH ₂) ⁺ using Gaussian (MP2-AUG-cc-pVTZ).	81

Table 5-2. Summary of the possible scenarios at 15 K. The effects are interpreted from the results obtained for $\text{Na}(\text{OH}_2)^+$ and $\text{Na}(\text{OH}_2)_6^+$ when the nozzle temperature is 15 K and the UV energy is below and above sodium's ionisation energy.	87
Table 5-3. Generated energy [cm^{-1}] after water and sodium complexation for increasing number of water molecules and calculated number of evaporated helium atoms. The last column gives the total number of evaporated helium atoms for formation of $\text{Na}(\text{OH}_2)_n^+$ complexes from atomic Na^+ , from the sum of each of the individual complexation steps.	89
Table 5-4. Experimental vibrational energies [cm^{-1}] of the symmetric and asymmetric OH_2 -stretching bands and rotational constant [cm^{-1}] of free water, $\text{Na}(\text{OH}_2)^+$ attached to argon and calculated values using Gaussian (MP2-AUG-cc-pVTZ). Obtained band origin [cm^{-1}], A and B rotational constants [cm^{-1}] and centrifugal-distortion constant D [cm^{-1}] obtained in helium droplets from the subbands for the different approaches..	98
Table 5-5. Number of evaporated helium atoms ΔN_{He} after sodium and water pick-up. Values of kinetic E_{kin} [cm^{-1}], internal E_{int} [cm^{-1}] and binding energy E_{bind} [cm^{-1}] for a given impurity temperature T_s [K] and mass m_s [u]. The velocity of the droplet beam v_D at 30 bar and 18 K is $387 \text{ m} \cdot \text{s}^{-1}$ [64]. Boltzmann constant is $0.695 \text{ cm}^{-1} \cdot \text{K}^{-1}$. The binding energies of sodium and water and taken from the literature ^[133, 155]	101
Table 5-6. Experimental values of the pressure P_s [mbar] and length L [m] of the doping cell, speed of the droplet beam v_D [$\text{m} \cdot \text{s}^{-1}$] at 30 bar and 18 K ^[64] , mass m_s [u] and temperature T_s [K] of the impurity and number of helium atoms N considering (or not) evaporative cooling.	101

ACKNOWLEDGEMENTS

Well, the moment has finally come. When I first visited Lausanne to interview for this PhD position, I could quickly picture myself living in Switzerland. The fact that now, several years later, I am able to sit and write these words after succeeding and making the most of my time here and of this rollercoaster called “PhD” has a lot to do with the people that have contributed to it during this time. Therefore, I would like to thank them today.

I would like to start by thanking my thesis director Dr. Marcel Drabbels for his guidance during these years. Thank you for always being behind the door every time I knocked to discuss any scientific matters and for introducing me to the technical aspects I needed to know in the laboratory. I am completely aware of what a luxury it is to have such an engaged supervisor who also allows independence and I am grateful for that.

I am very thankful to Prof. Vassily Hatzimanikatis, Prof. Wei Kong, Prof. Alkwin Slenczka and Prof. Thomas Rizzo for being part of my committee, evaluating this thesis and their insightful feedback and questions at the defence. A special thanks to Prof. Wei Kong for sending us the “mystery” code to calculate the pendular states, which was essential for the orientation chapter, and to Prof. Thomas Rizzo for the summer group barbecues at his place.

If I had to thank only one person for this thesis, it would be my friend and office buddy Andrew Clark. You have been there for me since my very first days at EPFL; I still remember the few weeks we shared in the lab in which neither of us knew what we were doing and you, as the senior, were pretending to control the situation. Thank you for the extra hands when needed in the lab, proofreading a huge part of my thesis, brainstorming, sharing ideas and all the help you have given me to achieve this goal. But more importantly, thank you for your support and being there just listening when necessary. You have been a great company during all the trips to conferences, beamtimes and summer/winter schools, badminton partner in the office and patatas/ice-cream breaks buddy. Your presence has been invaluable to me. We were a group of two, but honestly, I didn’t need more.

When I came to Lausanne as part of the LCPM group I did not know that I would end up in the LND group. After being a part of each group for almost half of my PhD time, I would like to thank the past and current members of both groups. To the past members for welcoming me and making my first months here easier, introducing me to the Swiss culture (though none of them were Swiss!) and organising events together. To the usual *very punctual* (11h45) lunch breaks at Vinci for very serious discussions not only about science but cryptocurrency, invention ideas and whatever else comes to mind. A special thanks to the people next door to the lab for not putting up with my loud music. Another special thanks goes to Chiara, present since the day of my interview, for being the official event organiser, giving a hand in the lab and for the many chats. Thanks to Val for his help with the OPO/OPA, introducing me to Gaussian and his enthusiasm in general. To Dr. Andreas Osterwalder for the many metro rides, brownies, smart ideas, advice and reading part of this thesis. Even though we work on different topics and were “forced” to be together, the LND group meetings have been very useful to have most of the figures in this thesis ready beforehand.

I have been also being quite lucky to have members of my neighbouring groups (GDP and especially LSU) that were always willing to discuss science, give suggestions and lending optics when needed. In particular I thank Rebecca for her contagious excitement and help with calculations. I guess I should thank in particular someone else from this group but I have already acknowledged him in person; thanks for the optimism you bring to my life.

Even though my thesis was not supposed to involve much technical work, I did end up modifying some equipment and involuntarily registered for the intensive course on “how to keep everything functioning at the same time”. Therefore, I spent quite some time at the ISIC workshops. Indeed, the first actual word I learnt in French when I arrived was “vis”. Merci beaucoup à tous les membres des ateliers mécanique, électronique et IT. En particulier à André Fattet, Guillaume Francey et Christophe Clément pour toutes les pièces fabriquées et réparées. Un très grand merci à Supardi Sujito de m’avoir aidé avec les lasers notamment, mais pour tout en général et à Grégoire Pasche et Benjamin Charles Le Geyt pour le HV-switch mais surtout pour tenir le sonde pendant chaque essai !

Merci beaucoup à Marie-Christine Lehmann et à Annick Gaudin, les secrétaires du groupe, pour s'occuper de tous les détails administratifs et relatifs au logement et surtout pour les petites conversations de temps en temps.

The fact that I decided to pursue a PhD was because of the great experience I had during my bachelor and master thesis with Prof. José Manuel López Poyato at the Universidad Autónoma de Madrid. I would like to thank him and Prof. Joaquín Juan Camacho for introducing me into research. This, together with the chats with Dr. Juan Pablo Cid, was critical to me appreciating science, and more specifically laser spectroscopy.

It is intriguing how life puts people together, and I have to thank fortune, and maybe also Prof. Rainer Beck, for bringing Ana to do her PhD at EPFL a month after I started mine. Muchas gracias por estar ahí, por los paseos alrededor del edificio cuando fueron necesarios y las muchas tardes de meriendas y conversaciones. Te deseo todo lo mejor en esta nueva etapa que ya sí que comenzamos.

I would like to thank the friends I met during these years here, especially Weitian and Loc for all the nice activities we did during our time together in Switzerland and for always showing me different perspectives. Of course, to my friends scattered everywhere that have been there via video calls during these years, visiting me here or just making sure I was making the most of my free time elsewhere. Here I should present the award to Cris and Laura for the “best long-distance friends”, being so for even longer than we were ever together and for being present in my life without even living in the same country.

Finally, a great part of this thesis belongs to my family, even if none of them are scientists, for their endless support. Muchas gracias por darme acceso a una buena educación, animarme a no ser conformista y apoyarme en mis decisiones. Pero sobre todo gracias por los valores que me habéis enseñado e inculcado: la perseverancia, el trabajo duro para conseguir lo que uno quiere, la amabilidad y el respeto a la gente. Gracias por estar siempre ahí, hacer que la distancia no parezca tan grande y vuestro infinito apoyo.

And you, the reader, for having a look at this thesis.

Lausanne, 25th June 2019.

CURRICULUM VITAE

Verónica Oliver Álvarez de Lara

Date of Birth: November 1st, 1991.

Nationality: Spanish.



EDUCATION

2015 – 2019 Ph.D. in Physical chemistry. École polytechnique fédérale de Lausanne (EPFL), Switzerland.

‘Orientation, rotation and solvation of ions in helium nanodroplets’, supervisor: Dr. Marcel Drabbels.

2013 - 2014 MSc Eng in Advanced and Applied Chemistry. Danmarks Tekniske Universitet (DTU), Denmark.

Erasmus placement during the Master thesis at Spanish National Research Council (CSIC) and Universidad Autónoma de Madrid (UAM).

‘Spectroscopic and dynamic analysis of plasmas generated by LIBS of Aluminium alloys’ under the supervision of Prof. José Manuel López Poyato.

2009 - 2013 Bachelor in Chemistry. Universidad Autónoma de Madrid (UAM), Spain.

One-year Erasmus programme at Danmarks Tekniske Universitet (DTU).

POSTER PRESENTATIONS

2018 ‘Pendular state spectroscopy of aniline ions in helium droplets’ at the Gordon Research Seminar (GRS) and at the Gordon Research Conference (GRC) on Molecular and Ionic Clusters, Lucca (Italy).

- 2017 'Pendular state spectroscopy of ions in helium nanodroplets' at Conference on Quantum Fluid Clusters (QFC), Obergurgl (Austria).
- 2016 'Pendular state spectroscopy in Helium nanodroplets' at Perspectives on Photonics Summer School, Gstaad (Switzerland).
- 2014 'Spectral characterization and temporal evolution of the induced plasma emission in the ablation of aluminium alloy' at the XXIV National Meeting on Spectroscopy (RNE) –VIII Iberian Conference on Spectroscopy (CIE), Logroño (Spain).

SCIENTIFIC PUBLICATIONS

B. Langbehn, K. Sander, Y. Ovcharenko, C. Peltz, A. Clark, M. Coreno, R. Cucini, M. Drabbels, P. Finetti, M. Di Fraia, L. Giannessi, C. Grazioli, D. Iablonskyi, A. C. LaForge, T. Nishiyama, V. Oliver Álvarez de Lara, P. Piseri, O. Plekan, K. Ueda, J. Zimmermann, K. C. Prince, F. Stienkemeier, C. Callegari, T. Fennel, D. Rupp, T. Möller, *Physical Review Letters* **2018**, 121, 255301.

A. C. LaForge, R. Michiels, M. Bohlen, C. Callegari, A. Clark, A. von Conta, M. Coreno, M. Di Fraia, M. Drabbels, M. Huppert, P. Finetti, J. Ma, M. Mudrich, V. Oliver, O. Plekan, K. C. Prince, M. Shcherbinin, S. Stranges, V. Svoboda, H. J. Wörner, F. Stienkemeier, *Physical Review Letters* **2019**, 122, 133001.

TEACHING EXPERIENCE

650 hours of experience at EPFL.

Laboratory teacher assistant of:

- Experimental Physical Chemistry (in English)
- Travaux Pratiques de Chimie de première année (in French)

LANGUAGES

Native Spanish.

English (B2 certificate 2008, 7 years of studies abroad).

French (fluent oral and intermediate written).

